INTERNATIONAL TABLES FOR CRYSTALLOGRAPHY

Volume D

PHYSICAL PROPERTIES OF CRYSTALS

Edited by

A. AUTHIER

Contributing authors

A. Authier: Institut de Minéralogie et de la Physique des Milieux Condensés, Bâtiment 7, 140 rue de Lourmel, 75051 Paris, France. E-mail: AAuthier@wanadoo.fr. [1.1, 1.3]

P. Boček: Institute of Information Theory and Automation, Academy of Sciences of the Czech Republic, Pod vodárenskou věží 4, 182 08 Prague 8, Czech Republic. E-mail: bocek@utia.cas.cz. [3.1.6, *GI⋆KoBo*-1]

A. S. Borovik–Romanov†: P. L. Kapitza Institute for Physical Problems, Russian Academy of Sciences, Kosygin Street 2, 119334 Moscow, Russia. [1.5]

B. Boulanger: Laboratoire de Spectrométrie Physique, Université Joseph Fourier, 140 avenue de la Physique, BP 87, 38 402 Saint-Martin-d'Hères, France. E-mail: benoit.boulanger@ujf-grenoble.fr. [1.7]

E. Courtens: Laboratoire des Verres, Université Montpellier 2, Case 069, Place Eugène Bataillon, 34095 Montpellier CEDEX, France. E-mail: eric.courtens@ldv.univ-montp2.fr. [2.4]

K. G. Cox†: Department of Earth Sciences, University of Oxford, Parks Road, Oxford OX1 3PR, England. [1.6]

G. Eckold: Institut für Physikalische Chemie, Universität Göttingen, Tammannstrasse 6, D-37077 Göttingen, Germany. E-mail: geckold@gwdg.de. [2.1]

M. Ephraïm: Advisory Engineering Agency PROMIS, PO Box 854, 1180 AW Amstelveen, The Netherlands. E-mail: M.Ephraim@promisbv.com. [1.2.7, *Ten*χ*ar*]

A. M. Glazer: Department of Physics, University of Oxford, Parks Road, Oxford OX1 3PU, England. E-mail: glazer@physics.ox.ac.uk. [1.6]

I. Gregora: Institute of Physics, Academy of Sciences of the Czech Republic, Na Slovance 2, CZ-18221 Prague 8, Czech Republic. E-mail: gregora@fzu.cz. [2.3]

H. Grimmer: Labor für Neutronenstreuung, ETH Zurich, and Paul Scherrer Institute, CH-5234 Villigen PSI, Switzerland. E-mail: hans.grimmer@psi.ch. [1.5]

Th. Hahn: Institut für Kristallographie, Rheinisch–Westfälische Technische Hochschule, D-52056 Aachen, Germany. E-mail: hahn@xtal.rwth-aachen.de. [3.2, 3.3]

A. Janner: Institute for Theoretical Physics, University of Nijmegen, 6525 ED Nijmegen, The Netherlands. E-mail: alo@sci.kun.nl. [1.2.7, *Ten*χ*ar*]

V. Janovec: Department of Physics, Technical University of Liberec, Hálkova 6, 461 17 Liberec 1, Czech Republic. Email: janovec@fzu.cz. [3.1.3, 3.2, 3.4]

T. Janssen: Institute for Theoretical Physics, University of Nijmegen, 6524 ED Nijmegen, The Netherlands. E-mail: ted@sci.kun.nl. [1.2, 1.10, *Ten*χ*ar*]

H. Klapper: Mineralogisch-Petrologisches Institut, Universität Bonn, D-53113 Bonn, Germany. E-mail: klapper@uni-bonn.de. [3.2, 3.3]

V. Kopský: Institute of Physics, Academy of Sciences of the Czech Republic, Na Slovance 2, 182 21 Prague 8, and Department of Physics, Technical University of Liberec, Hálkova 6, 461 17 Liberec 1, Czech Republic. E-mail: kopsky@fzu.cz. [3.1.3, 3.1.6, *GI⋆KoBo*-1]

W. F. Kuhs: GZG Abt. Kristallographie, Goldschmidtstrasse 1, 37077 Göttingen, Germany. E-mail: wkuhs1@gwdg.de. [1.9]

H. Küppers: Institut für Geowissenshaften, Universität Kiel, Olshausenstrasse 40, D-24098 Kiel, Germany. E-mail: kueppers@min.uni-kiel.de. [1.4]

G. D. Mahan: Department of Physics, 104 Davey Laboratory, Pennsylvania State University, University Park, Pennsylvania, USA. E-mail: gmahan@psu.edu. [1.8]

J. Přívratská: Department of Mathematics and Didactics of Mathematics, Technical University of Liberec, Hálkova 6, 461 17 Liberec 1, Czech Republic. E-mail: jana.privratska@vslib.cz. [3.4]

K. Schwarz: Institut für Materialchemie, Technische Universität Wien, Getreidemarkt 9/165-TC, A-1060 Vienna, Austria. Email: kschwarz@theochem.tuwien.ac.at. [2.2]

J. F. Scott: Earth Sciences Department, University of Cambridge, Downing Street, Cambridge CB2 3EQ England. E-mail: JSCO99@esc.cam.ac.uk. [3.1.5]

A. Thiers: AT Computing, Toernooiveld 104, 6525 EC Nijmegen, The Netherlands. Email: ad.thiers@ATConsultancy.nl. [1.2.7, *Ten*χ*ar*]

J.-C. Tolédano: Ecole Polytechnique, Route de Saclay, 91128 Palaiseau CEDEX France. E-mail: toledano@hp1sesi.polytechnique.fr. [3.1.1, 3.1.2, 3.1.4]

R. Vacher: Laboratoire des Verres, Université Montpellier 2, Case 069, Place Eugène Bataillon, 34095 Montpellier CEDEX, France. E-mail: rene.vacher@ldv.univ-montp2.fr. [2.4]

A. Zarembowitch: Laboratoire de Physique des Milieux Condensés, Université P. et M. Curie, 75252 Paris CEDEX 05, France. E-mail: Andre.Zarembowitch@pmc.jussieu.fr. [1.3]

J. Zyss: Laboratoire de Photonique Quantique et Moléculaire, Ecole Normale Supérieure de Cachan, 61 Avenue du Président Wilson, 94235 Cachan, France. E-mail: zyss.joseph@lpqm.ens-cachan.fr. [1.7]

† Deceased.

Contents

Preface

By André Authier

The initial idea of having a volume of *International Tables for Crystallography* dedicated to the physical properties of crystals is due to Professor B. T. M. Willis. He submitted the proposal to the Executive Committee of the International Union of Crystallography during their meeting in Vienna in 1988. The principle was then adopted, with Professor Willis as Editor. After his resignation in 1990, I was asked by the Executive Committee to become the new Editor. Following a broad consultation with many colleagues, a nucleus of potential authors met in Paris in June 1991 to define the contents of the volume and to designate its contributors. This was followed by a meeting in 1995, hosted by Theo Hahn in Aachen, of the authors contributing to Part 3 and by another meeting in 1998, hosted by Vaclav Janovec and Vojtech Kopský in Prague, of the authors of the supplementary software.

The aim of Volume D is to provide an up-to-date account of the physical properties of crystals, with many useful tables, to a wide readership in the fields of mineralogy, crystallography, solid-state physics and materials science. An original feature of the volume is the bringing together of various topics that are usually to be found in quite different handbooks but that have in common their tensorial nature and the role of crystallographic symmetry. Part 3 thus confronts the properties of twinning, which traditionally pertains to crystallography and mineralogy, and the properties of ferroelectric or ferroelastic domains, which are usually studied in physics.

The volume comprises three parts and a CD-ROM of supplementary software.

The first part is devoted to the tensorial properties of physical quantities. After a presentation of the matrix of physical properties and an introduction to the mathematical notion of a tensor, the symmetry properties of tensors and the representations of crystallographic groups are discussed, with a special treatment for the case of quasiperiodic structures. The first part also includes several examples of physical property tensors developed in separate chapters: elastic properties, thermal expansion, magnetic properties, optical properties (both linear and nonlinear), transport properties and atomic displacement parameters.

The second part is concerned with the symmetry aspects of excitations in reciprocal space. It includes bases of solid-state physics and describes in the first two chapters the properties of phonons and electrons in crystals. The following two chapters deal with Raman and Brillouin scattering.

The third part concerns structural phase transitions and twinning. The first chapter includes an introduction to the Landau theory, a description of the behaviour of physical property tensors at ferroic phase transitions and an approach to the microscopical aspect of structural transitions and soft modes, with practical examples. The second chapter explains the relationship between twinning and domain structures and introduces the group-theoretical tools needed for the analysis of domain structures and twins. In the third chapter, the basic concepts and definitions of twinning are presented, as well as the morphological, genetic and lattice classifications of twins and the properties of twin boundaries, with many examples. The fourth chapter is devoted to the symmetry and crystallographic analysis of domain structures. The relations that govern their formation are derived and tables with useful ready-to-use data on domain structures of ferroic phases are provided.

An innovation of Volume D is an accompanying CD-ROM containing two programs. The first, *Ten*χ*ar* (*Calculations with Tensors and Characters*) supports Part 1 for the determination of irreducible group representations and tensor components. The second, *GI*$\star$*KoBo*-1, supports Part 3 on structural phase transitions and enables the reader to find the changes in the tensor properties of physical quantities during ferroic phase transitions.

For various reasons, Volume D has taken quite a long time to produce, from the adoption of its principle in 1990 to its actual printing in 2003, and it is a particular pleasure for me to see the outcome of so many efforts. I would like to take this opportunity to thank all those who have contributed to the final result. Firstly, thanks are due to Terry Willis, whose idea the volume was and who made the initial push to have it accepted. I am very grateful to him for his encouragement and for having translated into English a set of notes that I had written for my students and which served as the nucleus of Chapter 1.1. I am greatly indebted to the Technical Editors who have worked tirelessly over the years: Sue Barnes in the early years and then Nicola Ashcroft, Amanda Berry and the staff of the Editorial Office in Chester, who did the hard work of editing all the chapters and translating them into Standard Generalized Markup Language (SGML); I thank them for their infinite patience and good humour. I am also very grateful to the Research and Development Officer, Brian McMahon, for his successful integration of the supplementary software and for his constant cooperation with its authors. Last but not least, I would like to thank all the authors who contributed to the volume and made it what it is.

SAMPLE PAGES

1.1. Introduction to the properties of tensors

By A. Authier

1.1.1. The matrix of physical properties

1.1.1.1. *Notion of extensive and intensive quantities*

Physical laws express in general the response of a medium to a certain influence. Most physical properties may therefore be defined by a relation coupling two or more measurable quantities. For instance, the specific heat characterizes the relation between a variation of temperature and a variation of entropy at a given temperature in a given medium, the dielectric susceptibility the relation between electric field and electric polarization, the elastic constants the relation between an applied stress and the resulting strain *etc*. These relations are between quantities of the same nature: thermal, electrical and mechanical, respectively. But there are also cross effects, for instance:

(*a*) *thermal expansion* and *piezocalorific effect*: mechanical reaction to a thermal impetus or the reverse;

(*b*) *pyroelectricity* and *electrocalorific effect*: electrical response to a thermal impetus or the reverse;

(*c*) *piezoelectricity* and *electrostriction*: electric response to a mechanical impetus;

(*d*) *piezomagnetism* and *magnetostriction*: magnetic response to a mechanical impetus;

(*e*) *photoelasticity*: birefringence produced by stress;

(*f*) *acousto-optic effect*: birefringence produced by an acoustic wave;

(*g*) *electro-optic effect*: birefringence produced by an electric field;

(*h*) *magneto-optic effect*: appearance of a rotatory polarization under the influence of a magnetic field.

The physical quantities that are involved in these relations can be divided into two categories:

(i) *extensive quantities*, which are proportional to the volume of matter or to the mass, that is to the number of molecules in the medium, for instance entropy, energy, quantity of electricity *etc.* One uses frequently specific extensive parameters, which are given per unit mass or per unit volume, such as the specific mass, the electric polarization (dipole moment per unit volume) *etc.*

(ii) *intensive parameters*, quantities whose product with an extensive quantity is homogeneous to an energy. For instance, volume is an extensive quantity; the energy stored by a gas undergoing a change of volume $\mathrm{d}V$ under pressure p is $p\ \mathrm{d}V$. Pressure is therefore the intensive parameter associated with volume. Table 1.1.1.1 gives examples of extensive quantities and of the related intensive parameters.

1.1.1.2. *Notion of tensor in physics*

Each of the quantities mentioned in the preceding section is represented by a mathematical expression. Some are direction independent and are represented by *scalars*: specific mass, specific heat, volume, pressure, entropy, temperature, quantity of electricity, electric potential. Others are direction dependent and are represented by *vectors*: force, electric field, electric displacement, the gradient of a scalar quantity. Still others cannot be represented by scalars or vectors and are represented by more complicated mathematical expressions. Magnetic quantities are represented by *axial* vectors (or pseudovectors), which are a particular kind of tensor (see Section 1.1.4.5.3). A few examples will show the necessity of using tensors in physics and Section 1.1.3 will present elementary mathematical properties of tensors.

(i) *Thermal expansion*. In an isotropic medium, thermal expansion is represented by a single number, a scalar, but this is not the case in an anisotropic medium: a sphere cut in an anisotropic medium becomes an ellipsoid when the temperature is varied and thermal expansion can no longer be represented by a single number. It is actually represented by a tensor of rank 2.

(ii) *Dielectric constant*. In an isotropic medium of a perfect dielectric we can write, in SI units,

$$\mathbf{P} = \varepsilon_0 \chi_e \mathbf{E}$$
$$\mathbf{D} = \varepsilon_0 \mathbf{E} + \mathbf{P} = \varepsilon_0 (1 + \chi_e)\mathbf{E} = \varepsilon \mathbf{E},$$

where $\mathbf{P}$ is the electric polarization (= dipole moment per unit volume), ε_0 the permittivity of vacuum, χ_e the dielectric susceptibility, $\mathbf{D}$ the electric displacement and ε the dielectric constant, also called dielectric permittivity. These expressions indicate that the electric field, on the one hand, and polarization and displacement, on the other hand, are linearly related. In the general case of an anisotropic medium, this is no longer true and one must write expressions indicating that the components of the displacement are linearly related to the components of the field:

$$\begin{cases} D^1 = \varepsilon_1^1 E^1 + \varepsilon_1^2 E^2 + \varepsilon_1^3 E \\ D^2 = \varepsilon_1^2 E^1 + \varepsilon_2^2 E^2 + \varepsilon_2^3 E \\ D^3 = \varepsilon_1^3 E^1 + \varepsilon_2^3 E^2 + \varepsilon_3^3 E. \end{cases} \qquad (1.1.1.1)$$

The dielectric constant is now characterized by a set of nine components ε_i^j; they are the components of a tensor of rank 2. It will be seen in Section 1.1.4.5.2.1 that this tensor is symmetric ($\varepsilon_i^j = \varepsilon_j^i$) and that the number of independent components is equal to six.

(iii) *Stressed rod (Hooke's law)*. If one pulls a rod of length ℓ and cross section $\mathcal{A}$ with a force F, its length is increased by a quantity $\Delta\ell$ given by $\Delta\ell/\ell = (1/E)F/\mathcal{A}$, where E is Young's modulus, or elastic stiffness (see Section 1.3.3.1). But, at the same time, the radius, r, decreases by Δr given by $\Delta r/r = -(\nu/E)F/\mathcal{A}$, where ν is Poisson's ratio (Section 1.3.3.4.3). It can be seen that a scalar is not sufficient to describe the elastic deformation of a material, even if it is isotropic. The number of independent components depends on the symmetry of the medium and it will be seen that they are the components of a tensor of rank 4. It was precisely to describe the properties of elasticity by a mathematical expression that the notion of a tensor was introduced in physics by W. Voigt in the 19th century (Voigt, 1910) and by L. Brillouin in the first half of the 20th century (Brillouin, 1949).

Table 1.1.1.1. *Extensive quantities and associated intensive parameters*

The last four lines of the table refer to properties that are time dependent.

Extensive quantities	Intensive parameters
Volume	Pressure
Strain	Stress
Displacement	Force
Entropy	Temperature
Quantity of electricity	Electric potential
Electric polarization	Electric field
Electric displacement	Electric field
Magnetization	Magnetic field
Magnetic induction	Magnetic field
Reaction rate	Chemical potential
Heat flow	Temperature gradient
Diffusion of matter	Concentration gradient
Electric current	Potential gradient

Furthermore, the left-hand term of (1.1.4.11) remains unchanged if we interchange the indices i and j. The terms on the right-hand side therefore also remain unchanged, whatever the value of T_{ll} or T_{kl}. It follows that

$$s_{ijll} = s_{jill}$$
$$s_{ijkl} = s_{ijlk} = s_{jikl} = s_{jilk}.$$

Similar relations hold for c_{ijkl}, Q_{ijkl}, p_{ijkl} and π_{ijkl}: the submatrices **2** and **3**, **4** and **7**, **5**, **6**, **8** and **9**, respectively, are equal.

Equation (1.4.1.11) can be rewritten, introducing the coefficients of the Voigt strain matrix:

$$S_\alpha = S_{ii} = \sum_l s_{iill} T_{ll} + \sum_{k\neq l} (s_{iikl} + s_{iilk}) T_{kl} \quad (\alpha = 1, 2, 3)$$
$$S_\alpha = S_{ij} + S_{ji} = \sum_l (s_{ijll} + s_{jill}) T_{ll} + \sum_{k\neq l} (s_{ijkl} + s_{ijlk} + s_{jikl} + s_{jilk}) T_{kl} \quad (\alpha = 4, 5, 6).$$

We shall now introduce a two-index notation for the elastic compliances, according to the following conventions:

$$\left.\begin{array}{llll} i=j; & k=l; & s_{\alpha\beta} = s_{iill} \\ i=j; & k\neq l; & s_{\alpha\beta} = s_{iikl} + s_{iilk} \\ i\neq j; & k=l; & s_{\alpha\beta} = s_{ijkk} + s_{jikk} \\ i\neq j; & k\neq l; & s_{\alpha\beta} = s_{ijkl} + s_{jikl} + s_{ijlk} + s_{jilk}. \end{array}\right\} \quad (1.1.4.12)$$

We have thus associated with the fourth-rank tensor a square 6×6 matrix with 36 coefficients:

α \ β	1	2	3	4	5	6
1	11	12	13	14	15	16
2	21	22	23	24	25	26
3	31	32	33	34	35	36
4	41	42	43	44	45	46
5	51	52	53	54	55	56
6	61	62	63	64	65	66

One can translate relation (1.1.4.12) using the 9×9 matrix representing s_{ijkl} by adding term by term the coefficients of submatrices **2** and **3**, **4** and **7** and **5**, **6**, **8** and **9**, respectively:

$$\left(\begin{array}{c|c} \mathbf{1} & \\ \hline \mathbf{2+3} & \end{array}\right) = \left(\begin{array}{c|c} \mathbf{1} & \mathbf{2} \\ \hline \mathbf{4+7} & \mathbf{5+6} \\ & \mathbf{+8+9} \end{array}\right) \times \left(\begin{array}{c|c} \mathbf{1} & \\ \hline \mathbf{2+3} & \end{array}\right)$$

Using the two-index notation, equation (1.1.4.9) becomes

$$S_\alpha = s_{\alpha\beta} T_\beta. \quad (1.1.4.13)$$

A similar development can be applied to the other fourth-rank tensors π_{ijkl}, which will be replaced by 6×6 matrices with 36 coefficients, according to the following rules.

(i) *Elastic stiffnesses*, c_{ijkl} and *elasto-optic coefficients*, p_{ijkl}:

$$\left(\begin{array}{c|c} \mathbf{1} & \\ \hline \mathbf{2} & \end{array}\right) = \left(\begin{array}{c|c} \mathbf{1} & \mathbf{2} \\ \hline \mathbf{4} & \mathbf{5} \end{array}\right) \times \left(\begin{array}{c|c} \mathbf{1} & \\ \hline \mathbf{2} & \end{array}\right)$$

where

$$c_{\alpha\beta} = c_{ijkl}$$
$$p_{\alpha\beta} = p_{ijkl}.$$

(ii) *Piezo-optic coefficients*, π_{ijkl}:

$$\left(\begin{array}{c|c} \mathbf{1} & \\ \hline \mathbf{2} & \end{array}\right) = \left(\begin{array}{c|c} \mathbf{1} & \mathbf{2+3} \\ \hline \mathbf{4} & \mathbf{5+6} \end{array}\right) \times \left(\begin{array}{c|c} \mathbf{1} & \\ \hline \mathbf{2} & \end{array}\right)$$

where

$$\left.\begin{array}{llll} i=j; & k=l; & \pi_{\alpha\beta} = \pi_{iill} \\ i=j; & k\neq l; & \pi_{\alpha\beta} = \pi_{iikl} + \pi_{iilk} \\ i\neq j; & k=l; & \pi_{\alpha\beta} = \pi_{ijkk} = \pi_{jikk} \\ i\neq j; & k\neq l; & \pi_{\alpha\beta} = \pi_{ijkl} + \pi_{jikl} = \pi_{ijlk} + \pi_{jilk}. \end{array}\right\}$$

(iii) *Electrostriction coefficients*, Q_{ijkl}: same relation as for the elastic compliances.

1.1.4.10.6. *Independent components of the matrix associated with a fourth-rank tensor according to the following point groups*

1.1.4.10.6.1. *Triclinic system, groups* $\bar{1}$, 1

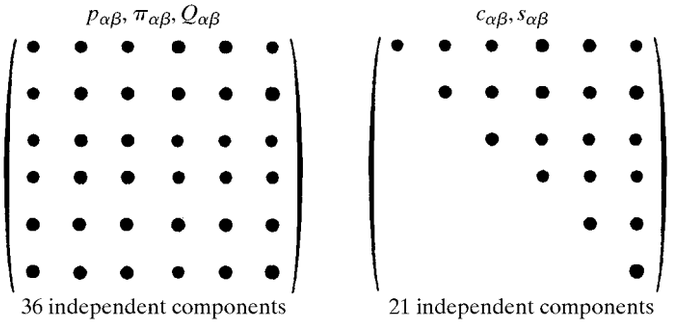

36 independent components — 21 independent components

1.1.4.10.6.2. *Monoclinic system*

Groups $2/m$, 2, m, twofold axis parallel to Ox_2:

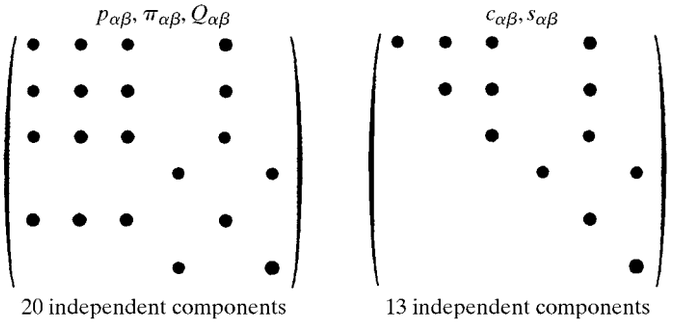

20 independent components — 13 independent components

1.1.4.10.6.3. *Orthorhombic system*

Groups *mmm*, 2*mm*, 222:

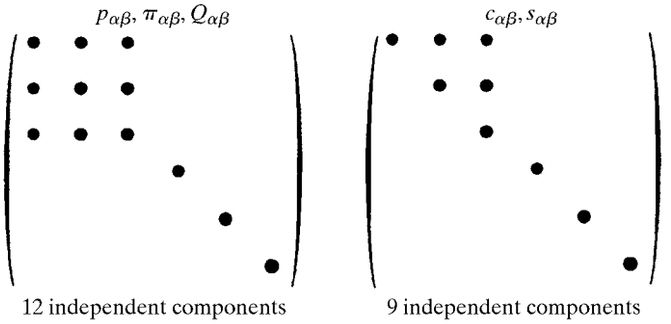

12 independent components — 9 independent components

1.2. Representations of crystallographic groups

By T. Janssen

1.2.1. Introduction

Symmetry arguments play an important role in science. Often one can use them in a heuristic way, but the correct formulation is in terms of group theory. This remark is in fact superfluous for crystallographers, who are used to point groups and space groups as they occur in the description of structures. However, besides these structural problems there are many others where group theory may play a role. A central role in this context is played by representation theory, which treats the action of a group on physical quantities, and usually this is done in terms of linear transformations, although nonlinear representations may also occur.

To start with an example, consider a spin system, an arrangement of spins on sites with a certain symmetry, for example space-group symmetry. The elements of the space group map the sites onto other sites, but at the same time the spins are rotated or transformed otherwise in a well defined fashion. The spins can be seen as elements of a vector space (spin space) and the transformation in this space is an image of the space-group element. In a similar way, all symmetric tensors of rank 2 form a vector space, because one can add them and multiply them by a real factor. A linear change of coordinates changes the vectors, and the transformations in the space of tensors are the image of the coordinate transformations. Probably the most important use of such representations is in quantum mechanics, where transformations in coordinate space are mapped onto linear transformations in the quantum mechanical space of state vectors.

To see the relation between groups of transformations and the use of their representations in physics, consider a tensor which transforms under a certain point group. Let us take a symmetric rank 2 tensor T_{ij} in three dimensions. We take as example the point group 222. From Section 1.1.3.2 one knows how such a tensor transforms: it transforms into a tensor T'_{ij} according to

$$T'_{ij} = \sum_{k=1}^{3}\sum_{m=1}^{3} R_{ik}R_{jm}T_{km} \qquad (1.2.1.1)$$

for all orthogonal transformations R in the group 222. This action of the point group 222 is obviously a linear one:

$$\left(c_1 T^{(1)}_{ij} + c_2 T^{(2)}_{ij}\right)' = c_1 T^{(1)\prime}_{ij} + c_2 T^{(2)\prime}_{ij}.$$

The transformations on the tensors really form an image of the group, because if one writes $D(R)T$ for T', one has for two elements $R^{(1)}$ and $R^{(2)}$ the relation

$$\big(D(R^{(1)}R^{(2)})\big)T = D(R^{(1)})\big(D(R^{(2)})T\big)$$

or

$$D(R^{(1)}R^{(2)}) = D(R^{(1)})D(R^{(2)}). \qquad (1.2.1.2)$$

This property is said to define a (linear) representation. Because of the representation property, it is sufficient to know how the tensor transforms under the generators of a group. In our example, one could be interested in symmetric tensors that are invariant under the group 222. Then it is sufficient to consider the rotations over 180° along the x and y axes. If the point group is a symmetry group of the system, a tensor describing the relation between two physical quantities should remain the same. For invariant tensors one has

$$\begin{pmatrix} a_{11} & a_{12} & a_{13} \\ a_{12} & a_{22} & a_{23} \\ a_{13} & a_{23} & a_{33} \end{pmatrix} = \begin{pmatrix} 1 & 0 & 0 \\ 0 & -1 & 0 \\ 0 & 0 & -1 \end{pmatrix}\begin{pmatrix} a_{11} & a_{12} & a_{13} \\ a_{12} & a_{22} & a_{23} \\ a_{13} & a_{23} & a_{33} \end{pmatrix}\begin{pmatrix} 1 & 0 & 0 \\ 0 & -1 & 0 \\ 0 & 0 & -1 \end{pmatrix},$$

$$\begin{pmatrix} a_{11} & a_{12} & a_{13} \\ a_{12} & a_{22} & a_{23} \\ a_{13} & a_{23} & a_{33} \end{pmatrix} = \begin{pmatrix} -1 & 0 & 0 \\ 0 & 1 & 0 \\ 0 & 0 & -1 \end{pmatrix}\begin{pmatrix} a_{11} & a_{12} & a_{13} \\ a_{12} & a_{22} & a_{23} \\ a_{13} & a_{23} & a_{33} \end{pmatrix}\begin{pmatrix} -1 & 0 & 0 \\ 0 & 1 & 0 \\ 0 & 0 & -1 \end{pmatrix}$$

and the solution of these equations is

$$\begin{pmatrix} a_{11} & a_{12} & a_{13} \\ a_{12} & a_{22} & a_{23} \\ a_{13} & a_{23} & a_{33} \end{pmatrix} = \begin{pmatrix} a_{11} & 0 & 0 \\ 0 & a_{22} & 0 \\ 0 & 0 & a_{33} \end{pmatrix}.$$

The matrices of rank 2 form a nine-dimensional vector space. The rotation over 180° around the x axis can also be written as

$$R\begin{pmatrix} a_{11} \\ a_{12} \\ a_{13} \\ a_{21} \\ a_{22} \\ a_{23} \\ a_{31} \\ a_{32} \\ a_{33} \end{pmatrix} = \begin{pmatrix} 1 & 0 & 0 & 0 & 0 & 0 & 0 & 0 & 0 \\ 0 & -1 & 0 & 0 & 0 & 0 & 0 & 0 & 0 \\ 0 & 0 & -1 & 0 & 0 & 0 & 0 & 0 & 0 \\ 0 & 0 & 0 & -1 & 0 & 0 & 0 & 0 & 0 \\ 0 & 0 & 0 & 0 & 1 & 0 & 0 & 0 & 0 \\ 0 & 0 & 0 & 0 & 0 & 1 & 0 & 0 & 0 \\ 0 & 0 & 0 & 0 & 0 & 0 & -1 & 0 & 0 \\ 0 & 0 & 0 & 0 & 0 & 0 & 0 & 1 & 0 \\ 0 & 0 & 0 & 0 & 0 & 0 & 0 & 0 & 1 \end{pmatrix}\begin{pmatrix} a_{11} \\ a_{12} \\ a_{13} \\ a_{21} \\ a_{22} \\ a_{23} \\ a_{31} \\ a_{32} \\ a_{33} \end{pmatrix}.$$

This nine-dimensional matrix together with the one corresponding to a rotation along the y axis generate a representation of the group 222 in the nine-dimensional space of three-dimensional rank 2 tensors. The invariant tensors form the subspace $(a_{11}, 0, 0, 0, a_{22}, 0, 0, 0, a_{33})$. In this simple case, group theory is barely needed. However, in more complex situations, the calculations may become quite cumbersome without group theory. Moreover, group theory may give a wealth of other information, such as selection rules and orthogonality relations, that can be obtained only with much effort without group theory, or in particular representation theory. Tables of tensor properties, and irreducible representations of point and space groups, have been in use for a long time. For point groups see, for example, Butler (1981) and Altmann & Herzig (1994); for space groups, see Miller & Love (1967), Kovalev (1987) and Stokes & Hatch (1988).

In the following, we shall discuss the representation theory of crystallographic groups. We shall adopt a slightly abstract language, which has the advantage of conciseness and generality, but we shall consider examples of the most important notions. Another point that could give rise to some problems is the fact that we shall consider in part the theory for crystallographic groups in arbitrary dimension. Of course, physics occurs in three-

Table 1.2.6.5. *Irreducible representations and character tables for the 32 crystallographic point groups in three dimensions*

(*a*) C_1

C_1	ε
n	1
Order	1
Γ_1	1

1 $\Gamma_1 : A = \chi_1$ x, y, z $x^2, y^2, z^2, yz, xz, xy$
C_1

(*b*) C_2

C_2	ε	α
n	1	1
Order	1	2
Γ_1	1	1
Γ_2	1	-1

2 $\alpha = C_{2z}$ $\Gamma_1 : A = \chi_1$ z x^2, y^2, z^2, xy
C_2 $\Gamma_2 : B = \chi_3$ x, y yz, xz

m $\alpha = \sigma_z$ $\Gamma_1 : A' = \chi_1$ x, y x^2, y^2, z^2, xy
C_s $\Gamma_2 : A'' = \chi_3$ z yz, xz

$\bar{1}$ $\alpha = I$ $\Gamma_1 : A_g = \chi_1^+$ $x^2, y^2, z^2, yz, xz, xy$
C_i $\Gamma_2 : A_u = \chi_1^-$ x, y, z

(*c*) C_3 $[\omega = \exp(2\pi i/3)]$.

C_3	ε	α	α^2
n	1	1	1
Order	1	3	3
Γ_1	1	1	1
Γ_2	1	ω	ω^2
Γ_3	1	ω^2	ω

Matrices of the real two-dimensional representation:

	ε	α	α^2
$\Gamma_2 \oplus \Gamma_3$	$\begin{pmatrix} 1 & 0 \\ 0 & 1 \end{pmatrix}$	$\begin{pmatrix} 0 & -1 \\ 1 & -1 \end{pmatrix}$	$\begin{pmatrix} -1 & 1 \\ -1 & 0 \end{pmatrix}$

3 $\alpha = C_{3z}$ $\Gamma_1 : A = \chi_1$ z $x^2 + y^2, z^2$
C_3 $\Gamma_2 \oplus \Gamma_3 : E = \chi_{1c} + \chi_{1c}^*$ x, y $x^2 - y^2, xz, yz, xy$

(*d*) C_4

C_4	ε	α	α^2	α^3
n	1	1	1	1
Order	1	4	2	4
Γ_1	1	1	1	1
Γ_2	1	i	-1	$-i$
Γ_3	1	-1	1	-1
Γ_4	1	$-i$	-1	i

Matrices of the real two-dimensional representation:

	ε	α	α^2	α^3
$\Gamma_2 \oplus \Gamma_4$	$\begin{pmatrix} 1 & 0 \\ 0 & 1 \end{pmatrix}$	$\begin{pmatrix} 0 & -1 \\ 1 & 0 \end{pmatrix}$	$\begin{pmatrix} -1 & 0 \\ 0 & -1 \end{pmatrix}$	$\begin{pmatrix} 0 & 1 \\ -1 & 0 \end{pmatrix}$

4 $\alpha = C_{4z}$ $\Gamma_1 : A = \chi_1$ z $x^2 + y^2, z^2$
C_4 $\Gamma_3 : B = \chi_3$ $x^2 - y^2, xy$
$\Gamma_2 \oplus \Gamma_4 : E = \chi_{1c} + \chi_{1c}^*$ x, y yz, xz

$\bar{4}$ $\alpha = S_4$ $\Gamma_1 : A = \chi_1$ $x^2 + y^2, z^2$
S_4 $\Gamma_3 : B = \chi_3$ z $x^2 - y^2, xy$
$\Gamma_2 \oplus \Gamma_4 : E = \chi_{1c} + \chi_{1c}^*$ x, y yz, xz

(*e*) C_6 $[\omega = \exp(\pi i/3)]$.

C_6	ε	α	α^2	α^3	α^4	α^5
n	1	1	1	1	1	1
Order	1	6	3	2	3	6
Γ_1	1	1	1	1	1	1
Γ_2	1	ω	ω^2	-1	$-\omega$	$-\omega^2$
Γ_3	1	ω^2	$-\omega$	1	ω^2	$-\omega$
Γ_4	1	-1	1	-1	1	-1
Γ_5	1	$-\omega$	ω^2	1	$-\omega$	ω^2
Γ_6	1	$-\omega^2$	$-\omega$	-1	ω^2	ω

Matrices of the real representations:

	$\Gamma_2 \oplus \Gamma_6$	$\Gamma_3 \oplus \Gamma_5$
ε	$\begin{pmatrix} 1 & 0 \\ 0 & 1 \end{pmatrix}$	$\begin{pmatrix} 1 & 0 \\ 0 & 1 \end{pmatrix}$
α	$\begin{pmatrix} 1 & -1 \\ 1 & 0 \end{pmatrix}$	$\begin{pmatrix} 0 & -1 \\ 1 & -1 \end{pmatrix}$
α^2	$\begin{pmatrix} 0 & -1 \\ 1 & -1 \end{pmatrix}$	$\begin{pmatrix} -1 & 1 \\ -1 & 0 \end{pmatrix}$
α^3	$\begin{pmatrix} -1 & 0 \\ 0 & -1 \end{pmatrix}$	$\begin{pmatrix} 1 & 0 \\ 0 & 1 \end{pmatrix}$
α^4	$\begin{pmatrix} -1 & 1 \\ -1 & 0 \end{pmatrix}$	$\begin{pmatrix} 0 & -1 \\ 1 & -1 \end{pmatrix}$
α^5	$\begin{pmatrix} 0 & 1 \\ -1 & 1 \end{pmatrix}$	$\begin{pmatrix} -1 & 1 \\ -1 & 0 \end{pmatrix}$

6 $\alpha = C_{6z}$ $\Gamma_1 : A = \chi_1$ z $x^2 + y^2, z^2$
C_6 $\Gamma_4 : B = \chi_3$
$\Gamma_2 \oplus \Gamma_6$: $E_1 = \chi_{1c} + \chi_{1c}^*$ x, y xz, yz
$\Gamma_3 \oplus \Gamma_5$: $E_2 = \chi_{2c} + \chi_{2c}^*$ $x^2 - y^2, xy$

$\bar{3}$ $\alpha = S_{3z}$ $\Gamma_1 : A_g = \chi_1^+$ $x^2 + y^2, z^2$
S_6 $\Gamma_4 : A_u = \chi_1^-$ z
$\Gamma_2 \oplus \Gamma_6$: $E_u = \chi_{1c}^- + \chi_{1c}^{-*}$ x, y
$\Gamma_3 \oplus \Gamma_5$: $E_g = \chi_{1c}^+ + \chi_{1c}^{+*}$ $x^2 - y^2, xy, xz, yz$

$\bar{6}$ $\alpha = S_{6z}$ $\Gamma_1 : A' = \chi_1$ $x^2 + y^2, z^2$
C_{3h} $\Gamma_4 : A'' = \chi_3$ z
$\Gamma_2 \oplus \Gamma_6$: $E' = \chi_{2c} + \chi_{2c}^*$ xz, yz
$\Gamma_3 \oplus \Gamma_5$: $E'' = \chi_{1c} + \chi_{1c}^*$ x, y $x^2 - y^2, xy$

(*f*) D_2

D_2	ε	α	β	$\alpha\beta$
n	1	1	1	1
Order	1	2	2	2
Γ_1	1	1	1	1
Γ_2	1	1	-1	-1
Γ_3	1	-1	1	-1
Γ_4	1	-1	-1	1

222 $\alpha = C_{2x}$ $\Gamma_1 : A_1 = \chi_1$ x^2, y^2, z^2
D_2 $\beta = C_{2y}$ $\Gamma_2 : B_3 = \chi_3$ x yz
$\alpha\beta = C_{2z}$ $\Gamma_3 : B_2 = \chi_4$ y xz
$\Gamma_4 : B_1 = \chi_2$ z xz

$mm2$ $\alpha = C_{2z}$ $\Gamma_1 : A_1 = \chi_1$ z x^2, y^2, z^2
C_{2v} $\beta = \sigma_x$ $\Gamma_2 : A_2 = \chi_2$ xy
$\alpha\beta = \sigma_y$ $\Gamma_3 : B_2 = \chi_3$ y yz
$\Gamma_4 : B_1 = \chi_4$ x xz

$2/m$ $\alpha = C_{2z}$ $\Gamma_1 : A_g = \chi_1^+$ x^2, y^2, z^2, xy
C_{2h} $\beta = \sigma_z$ $\Gamma_2 : A_u = \chi_1^-$ z z
$\alpha\beta = I$ $\Gamma_3 : B_u = \chi_3^-$ x, y
$\Gamma_4 : B_g = \chi_3^+$

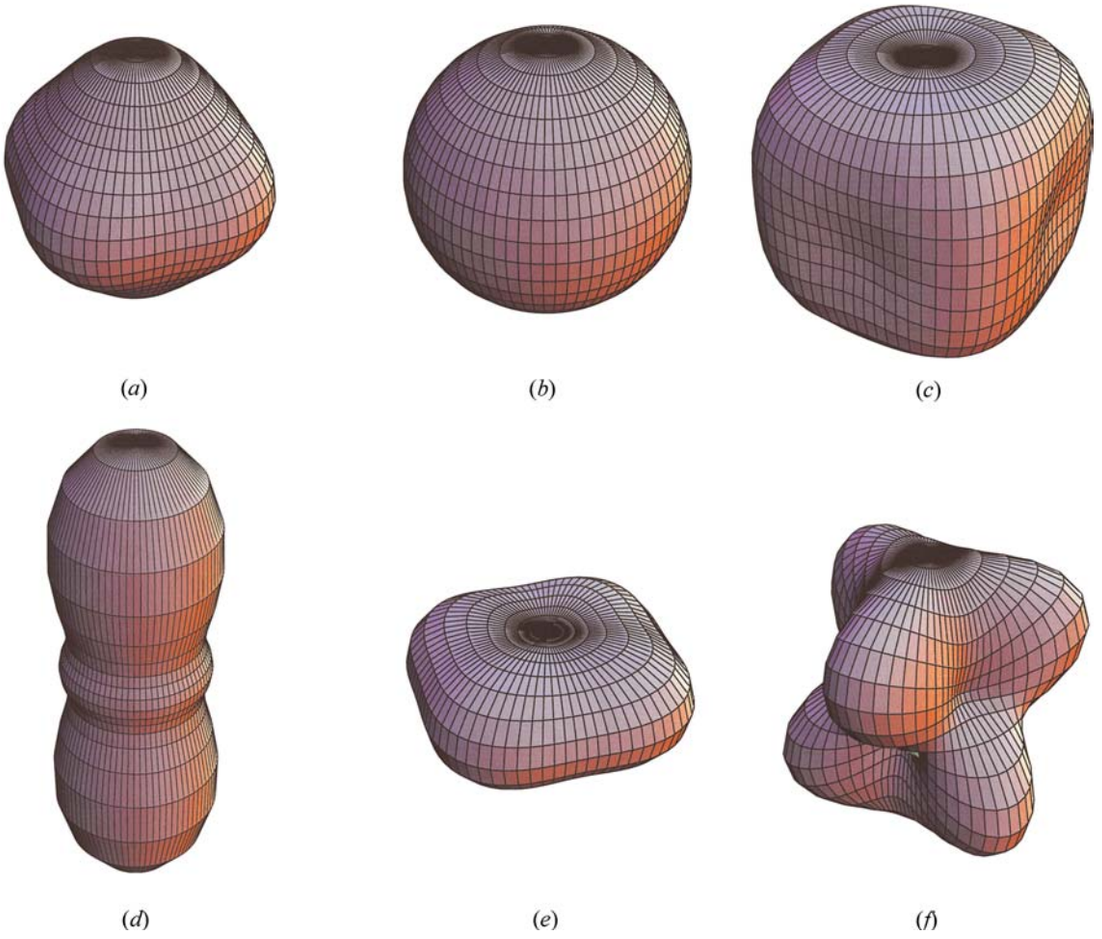

Fig. 1.3.3.4. Representation surface of the inverse of Young's modulus. (*a*) NaCl, cubic, anisotropy factor > 1; (*b*) W, cubic, anisotropy factor $= 1$; (*c*) Al, cubic, anisotropy factor < 1; (*d*) Zn, hexagonal; (*e*) Sn, tetragonal; (*f*) calcite, trigonal.

If one introduces the Lamé constants,

$$\mu = (1/2)(c_{11} - c_{12}) = c_{44}$$
$$\lambda = c_{12},$$

the equations may be written in the form often used in mechanics:

$$\begin{aligned} T_1 &= 2\mu S_1 + \lambda(S_1 + S_2 + S_3) \\ T_2 &= 2\mu S_2 + \lambda(S_1 + S_2 + S_3) \\ T_3 &= 2\mu S_3 + \lambda(S_1 + S_2 + S_3). \end{aligned} \tag{1.3.3.16}$$

Two coefficients suffice to define the elastic properties of an isotropic material, s_{11} and s_{12}, c_{11} and c_{12}, μ and λ, μ and ν, *etc.* Table 1.3.3.3 gives the relations between the more common elastic coefficients.

1.3.3.6. *Equilibrium conditions of elasticity for isotropic media*

We saw in Section 1.3.2.3 that the condition of equilibrium is

$$\partial T_{ij}/\partial x_i + \rho F_j = 0.$$

If we use the relations of elasticity, equation (1.3.3.2), this condition can be rewritten as a condition on the components of the strain tensor:

$$c_{ijkl}\frac{\partial S_{kl}}{\partial x_j} + \rho F_i = 0.$$

Recalling that

$$S_{kl} = \tfrac{1}{2}\left[\frac{\partial u_k}{\partial x_l} + \frac{\partial u_l}{\partial x_k}\right],$$

the condition becomes a condition on the displacement vector, $\mathbf{u}(\mathbf{r})$:

$$c_{ijkl}\frac{\partial^2}{\partial x_l \partial x_j} + \rho F_i = 0.$$

In an isotropic orthonormal medium, this equation, projected on the axis $0x_1$, can be written with the aid of relations (1.3.3.5) and (1.3.3.9):

$$\begin{aligned} c_{11}\frac{\partial^2 u_1}{(\partial x_1)^2} + c_{12}\left[\frac{\partial^2 u_2}{\partial x_1 \partial x_2} + \frac{\partial^2 u_3}{\partial x_1 \partial x_3}\right] \\ + \tfrac{1}{2}(c_{11} - c_{12})\left[\frac{\partial^2 u_1}{(\partial x_2)^2} + \frac{\partial^2 u_3}{\partial x_1 \partial x_3} + \frac{\partial^2 u_1}{(\partial x_3)^2}\right] + \rho F_i \\ = 0. \end{aligned}$$

This equation can finally be rearranged in one of the three following forms with the aid of Table 1.3.3.3.

$$\begin{aligned} \tfrac{1}{2}(c_{11} - c_{12})\Delta\mathbf{u} + \tfrac{1}{2}(c_{11} + c_{12})\nabla(\nabla\mathbf{u}) + \rho\mathbf{F} = 0 \\ \mu\Delta\mathbf{u} + (\mu + \lambda)\nabla(\nabla\mathbf{u}) + \rho\mathbf{F} = 0 \\ \mu\left[\Delta\mathbf{u} + \frac{1}{1 - 2\nu}\nabla(\nabla\mathbf{u})\right] + \rho\mathbf{F} = 0. \end{aligned} \tag{1.3.3.17}$$

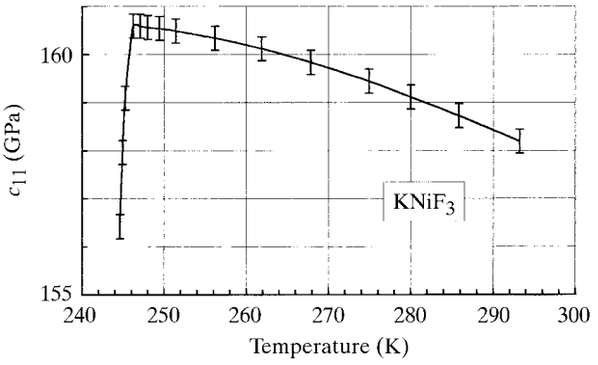

Fig. 1.3.5.4. Temperature dependence of the elastic constant c_{11} in $KNiF_3$, which undergoes a para–antiferromagnetic phase transition. Reprinted with permission from *Appl. Phys. Lett.* (Nouet *et al.*, 1972). Copyright (1972) American Institute of Physics.

The softening of c_{44} when the temperature decreases starts more than 100 K before the critical temperature, Θ_c. In contrast, Fig. 1.3.5.4 shows the temperature dependence of c_{11} in $KNiF_3$, a crystal that undergoes a para–antiferromagnetic phase transition at 246 K; the coupling between the elastic and the magnetic energy is weak, consequently c_{11} decreases abruptly only a few degrees before the critical temperature. We can generalize this observation and state that the softening of an elastic constant occurs over a large domain of temperature when this constant is the order parameter or is strongly coupled to the order parameter of the transformation; for instance, in the cooperative Jahn–Teller phase transition in $DyVO_4$, $(c_{11} - c_{12})/2$ is the soft acoustic phonon mode leading to the phase transition and this parameter anticipates the phase transition 300 K before it occurs (Fig. 1.3.5.5).

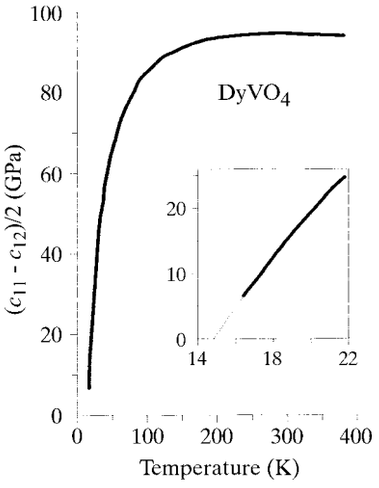

Fig. 1.3.5.5. Temperature dependence of $(c_{11} - c_{12})/2$ in $DyVO_4$, which undergoes a cooperative Jahn–Teller phase transition (after Melcher & Scott, 1972).

1.3.5.3. *Pressure dependence of the elastic constants*

As mentioned above, anharmonic potentials are needed to explain the stress dependence of the elastic constants of a crystal. Thus, if the strain-energy density is developed in a polynomial in terms of the strain, only the first and the second elastic constants are used in linear elasticity (harmonic potentials), whereas higher-order elastic constants are also needed for nonlinear elasticity (anharmonic potentials).

Concerning the pressure dependence of the elastic constants (nonlinear elastic effect), considerable attention has been paid to their experimental determination since they are a unique source of significant information in many fields:

(i) In *geophysics*, a large part of the knowledge we have on the interior of the earth comes from the measurement of the transit time of elastic bursts propagating in the mantle and in the core (in the upper mantle, the average pressure is estimated to be about a few hundred GPa, a value which is comparable to that of the elastic stiffnesses of many materials).

(ii) In *solid-state physics*, the pressure dependence of the elastic constants gives significant indications concerning the stability of crystals. For example, Fig. 1.3.5.2 shows the pressure dependence of the elastic constants of $KZnF_3$, a cubic crystal belonging to the perovskite family. As mentioned previously, this crystal is known to be stable over a wide range of temperature and the elastic stiffnesses c_{ij} depend linearly on pressure. It may be noted that, consequently, the third-order elastic constants (TOECs) are constant. On the contrary, we observe in Fig. 1.3.5.6 that the pressure dependence of the elastic constants of $TlCdF_3$, a cubic crystal belonging to the same family but which is known to become unstable when the temperature is decreased to 191 K (Fischer, 1982), is nonlinear even at low pressures. In this case, the development of the strain-energy density in terms of strains cannot be stopped after the terms containing the third-order elastic constants; the contributions of the fourth- and fifth-order elastic constants are not negligible.

(iii) For practical use in the case of technical materials such as concrete or worked metals, the pressure dependence of the elastic moduli is also required for examining the effect of applied stresses or of an applied hydrostatic pressure, and for studying residual stresses resulting from loading (heating) and unloading (cooling) the materials.

Table 1.3.5.2. *Order of magnitude of the temperature dependence of the elastic stiffnesses for different types of crystals*

Type of crystal	$(\partial \ln c_{11}/\partial\Theta)_p$ (K^{-1})	$(\partial \ln c_{44}/\partial\Theta)_p$ (K^{-1})
Ionic	-10^{-3}	-3×10^{-4}
Covalent	-10^{-4}	-8×10^{-5}
Metallic	-2×10^{-4}	-3×10^{-4}

1.3.6. Nonlinear elasticity

1.3.6.1. *Introduction*

In a solid body, the relation between the stress tensor T and the strain tensor S is usually described by Hooke's law, which postulates linear relations between the components of T and S (Section 1.3.3.1). Such relations can be summarized by (see equation 1.3.3.2)

$$T_{ij} = c_{ijkl} S_{kl},$$

where the c_{ijkl}'s are the elastic stiffnesses.

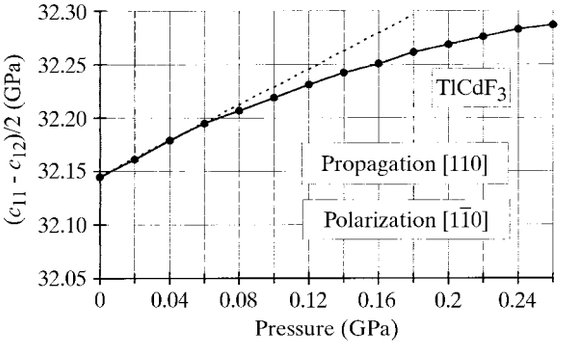

Fig. 1.3.5.6. Pressure dependence of the elastic constants $(c_{11} - c_{12})/2$ in $TlCdF_3$. Reproduced with permission from *Ultrasonics Symposium Proc. IEEE* (Fischer *et al.*, 1980). Copyright (1980) IEEE.

It should be mentioned that the true situation is more complicated. The grain boundaries of anisotropic polycrystalline solids are subject to considerable stresses because the neighbouring grains have different amounts of expansion or contraction. These stresses may cause local plastic deformation and cracks may open up between or within the grains. These phenomena can lead to a hysteresis behaviour when the sample is heated up or cooled down. Of course, in polycrystals of a cubic crystal species, these problems do not occur.

If the polycrystalline sample exhibits a texture, the orientation distribution function (ODF) has to be considered in the averaging process. The resulting overall symmetry of a textured polycrystal is usually $\frac{\infty}{m}m$ (see Section 1.1.4.7.4.2), showing the same tensor form as hexagonal crystals (Table 1.4.1.1), or *mmm*.

Table 1.4.1.1. *Shape of the quadric and symmetry restrictions*

System	Quadric: Shape	Quadric: Direction of principal axes	No. of independent components	Nonzero components
Triclinic	General ellipsoid or hyperboloid	No restrictions	6	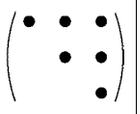
Monoclinic		One axis parallel to twofold axis (**b**)	4	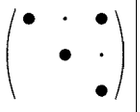
Orthorhombic		Parallel to crystallographic axes	3	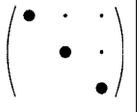
Trigonal, tetragonal, hexagonal	Revolution ellipsoid or hyperboloid	*c* axis is revolution axis	2	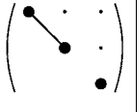
Cubic, isotropic media	Sphere	Arbitrary, not defined	1	

1.4.2. Grüneisen relation

Thermal expansion of a solid is a consequence of the anharmonicity of interatomic forces (see also Section 2.1.2.8). If the potentials were harmonic, the atoms would oscillate (even with large amplitudes) symmetrically about their equilibrium positions and their mean central position would remain unchanged. In order to describe thermal expansion, the anharmonicity is most conveniently accounted for by means of the so-called 'quasiharmonic approximation', assuming the lattice vibration frequencies ω to be independent of temperature but dependent on volume $[(\partial\omega/\partial V) \neq 0]$. Anharmonicity is taken into account by letting the crystal expand, but it is assumed that the atoms vibrate about their new equilibrium positions harmonically, *i.e.* lattice dynamics are still treated in the harmonic approximation. The assumption $(\partial\omega/\partial V) = 0$, which is made for the harmonic oscillator, is a generalization of the postulate that the frequency of a harmonic oscillator does not depend on the amplitude of vibration.

This approach leads, as demonstrated below, to the Grüneisen relation, which combines thermal expansion with other material constants and, additionally, gives an approximate description of the temperature dependence of thermal expansion (*cf.* Krishnan *et al.*, 1979; Barron, 1998).

For isotropic media, the volume expansion β $[= 3\alpha = \alpha_{11} + \alpha_{22} + \alpha_{33}]$, *cf.* (1.4.1.2), can be expressed by the thermodynamic relation

$$\beta = \frac{1}{V}\left(\frac{\partial V}{\partial T}\right)_p = -\frac{1}{V}\left(\frac{\partial V}{\partial p}\right)_T \left(\frac{\partial p}{\partial T}\right)_V = \kappa\left(\frac{\partial p}{\partial T}\right)_V, \qquad (1.4.2.1)$$

κ being the isothermal compressibility. To obtain the quantity $(\partial p/\partial T)_V$, the pressure p is deduced from the free energy F, whose differential is $\mathrm{d}F = -S\ \mathrm{d}T - p\ \mathrm{d}V$, *i.e.* from

$$p = -(\partial F/\partial V)_T. \qquad (1.4.2.2)$$

In a crystal consisting of N unit cells with p atoms in each unit cell, there are $3p$ normal modes with frequencies ω_s (denoted by an index s running from 1 to $3p$) and with N allowed wavevectors $\mathbf{q}_t$ (denoted by an index t running from 1 to N). Each normal mode $\omega_s(\mathbf{q}_t)$ contributes to the free energy by the amount

$$f_{s,t} = \frac{\hbar}{2}\omega_s(\mathbf{q}_t) + kT \ln\left[1 - \exp\left(-\frac{\hbar\omega_s(\mathbf{q}_t)}{kT}\right)\right]. \qquad (1.4.2.3)$$

The total free energy amounts, therefore, to

$$F = \sum_{s=1}^{3p}\sum_{t=1}^{N} f_{s,t}$$

$$= \sum_{s=1}^{3p}\sum_{t=1}^{N}\left\{\frac{\hbar}{2}\omega_s(\mathbf{q}_t) + kT \ln\left[1 - \exp\left(-\frac{\hbar\omega_s(\mathbf{q}_t)}{kT}\right)\right]\right\}. \qquad (1.4.2.4)$$

From (1.4.2.2)

$$p = -\left(\frac{\partial F}{\partial V}\right)_T$$

$$= -\sum_{s=1}^{3p}\sum_{t=1}^{N}\left\{\frac{\hbar}{2}\frac{\partial\omega_s}{\partial V} + \frac{\exp(-\hbar\omega_s/kT)\hbar(\partial\omega_s/\partial V)}{1 - \exp(-\hbar\omega_s/kT)}\right\}. \qquad (1.4.2.5)$$

The last term can be written as

$$\frac{\hbar(\partial\omega_s/\partial V)}{\exp(\hbar\omega_s/kT) - 1} = \hbar n(\omega_s(\mathbf{q}_t), T)\frac{\partial\omega_s}{\partial V}, \qquad (1.4.2.6)$$

where $n(\omega_s, T)$ is the Bose–Einstein distribution

The behaviour of the transition-metal ions is very different. In contrast to the rare-earth ions, the electrons of the partly filled shell in transition metals interact strongly with the electric field of the crystal. As a result, their energy levels are split and the orbital moments can be 'quenched'. This means that relation (1.5.1.5) transforms to

$$p_{ij} = (g_{\rm eff})_{ij}[S(S+1)]^{1/2}. \qquad (1.5.1.6)$$

Here the value of the effective spin S represents the degeneration of the lowest electronic energy level produced by the splitting in the crystalline field; $(g_{\rm eff})_{ij}$ differs from the usual Landé g-factor. The values of its components lie between 0 and 10–20. The tensor $(g_{\rm eff})_{ij}$ becomes diagonal in the principal axes. According to relation (1.5.1.6), the magnetic susceptibility also becomes a tensor. The anisotropy of $(g_{\rm eff})_{ij}$ can be studied using electron paramagnetic resonance (EPR) techniques.

The Curie–Weiss law describes the behaviour of those paramagnets in which the magnetization results from the competition of two forces. One is connected with the reduction of the magnetic energy by orientation of the magnetic moments of ions in the applied magnetic field; the other arises from thermal fluctuations, which resist the tendency of the field to orient these moments. At low temperatures and in strong magnetic fields, the linear dependence of the magnetization *versus* magnetic field breaks down and the magnetization can be saturated in a sufficiently strong magnetic field. Most of the paramagnetic substances that obey the Curie–Weiss law ultimately transform to an ordered magnetic as the temperature is decreased.

The conduction electrons in metals possess paramagnetism in addition to diamagnetism. The paramagnetic susceptibility of the conduction electrons is small (of the same order of magnitude as the diamagnetic susceptibility) and does not depend on temperature. This is due to the fact that the conduction electrons are governed by the laws of Fermi–Dirac statistics.

1.5.1.2. *Ordered magnetics*

1.5.1.2.1. *Ferromagnets (including ferrimagnets)*

As stated above, all ordered magnetics that possess a spontaneous magnetization $\mathbf{M}_s$ different from zero (a magnetization even in zero magnetic field) are called ferromagnets. The simplest type of ferromagnet is shown in Fig. 1.5.1.2(*a*). This type possesses only one kind of magnetic ion or atom. All their magnetic moments are aligned parallel to each other in the same direction. This magnetic structure is characterized by one vector **M**. It turns out that there are very few ferromagnets of this type in which only atoms or ions are responsible for the ferromagnetic magnetization ($CrBr_3$, EuO *etc.*). The overwhelming majority of ferromagnets of this simplest type are metals, in which the magnetization is the sum of the magnetic moments of the localized ions and of the conduction electrons, which are partly polarized.

More complicated is the type of ferromagnet which is called a ferrimagnet. This name is derived from the name of the oxides of the elements of the iron group. As an example, Fig. 1.5.1.2(*b*) schematically represents the magnetic structure of magnetite (Fe_3O_4). It contains two types of magnetic ions and the number of Fe^{3+} ions ($\boldsymbol{\mu}_1$ and $\boldsymbol{\mu}_2$) is twice the number of Fe^{2+} ions ($\boldsymbol{\mu}_3$). The values of the magnetic moments of these two types of ions differ. The magnetic moments of all Fe^{2+} ions are aligned in one direction. The Fe^{3+} ions are divided into two parts: the magnetic moments of one half of these ions are aligned parallel to the magnetic moments of Fe^{2+} and the magnetic moments of the other half are aligned antiparallel. The array of all magnetic moments of identical ions oriented in one direction is called a magnetic sublattice. The magnetization vector of a given sublattice will be denoted by $\mathbf{M}_i$. Hence the magnetic structure of Fe_3O_4 consists of three magnetic sublattices. The magnetizations of two of them are aligned in one direction, the magnetization of the third one is oriented in the opposite direction. The net ferromagnetic magnetization is $M_s = M_1 - M_2 + M_3 = M_3$.

The special feature of ferrimagnets, as well as of many antiferromagnets, is that they consist of sublattices aligned antiparallel to each other. Such a structure is governed by the nature of the main interaction responsible for the formation of the ordered magnetic structures, the exchange interaction. The energy of the exchange interaction does not depend on the direction of the interacting magnetic moments (or spins **S**) rela-

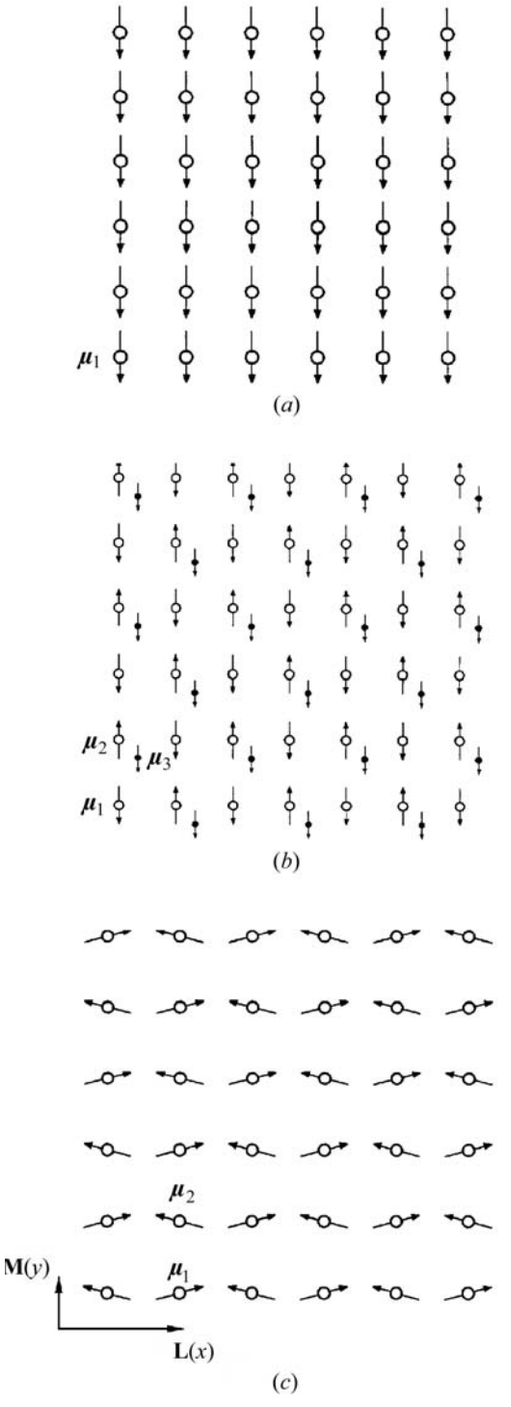

Fig. 1.5.1.2. Ordered arrangements of magnetic moments $\boldsymbol{\mu}_i$ in: (*a*) an ordinary ferromagnet $\mathbf{M}_s = N\boldsymbol{\mu}_1$; (*b*) a ferrimagnet $\mathbf{M}_s = (N/3)(\boldsymbol{\mu}_1 + \boldsymbol{\mu}_2 + \boldsymbol{\mu}_3)$; (*c*) a weak ferromagnet $\mathbf{M} = \mathbf{M}_D = (N/2)(\boldsymbol{\mu}_1 + \boldsymbol{\mu}_2)$, $\mathbf{L} = (N/2)(\boldsymbol{\mu}_1 - \boldsymbol{\mu}_2)$, ($L_x \gg M_y$; $M_x = M_z = L_y = L_z = 0$). ($N$ is the number of magnetic ions per cm^3.)

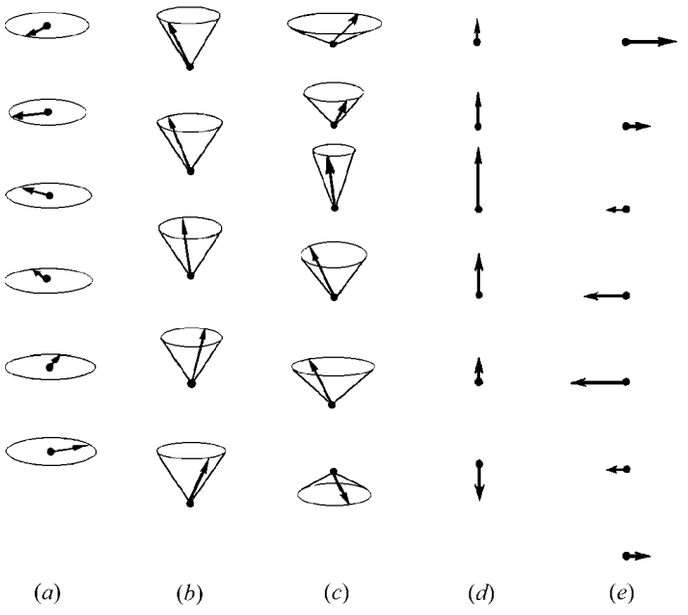

Fig. 1.5.1.4. Helical and sinusoidal magnetic structures. (*a*) An antiferromagnetic helix; (*b*) a cone spiral; (*c*) a cycloidal spiral; (*d*) a longitudinal spin-density wave; (*e*) a transverse spin-density wave.

the vectors of the magnetization of the layers are arranged on the surface of a cone. The ferromagnetic magnetization is aligned along the z axis. This structure is called a ferromagnetic helix. It usually belongs to the incommensurate magnetic structures.

More complicated antiferromagnetic structures also exist: sinusoidal structures, which also consist of layers in which all the magnetic moments are parallel to each other. Fig. 1.5.1.4(*c*) displays the cycloidal spiral and Figs. 1.5.1.4(*d*) and (*e*) display longitudinal and transverse spin density waves, respectively.

1.5.2. Magnetic symmetry

As discussed in Section 1.5.1, in studies of the symmetry of magnetics one should take into account not only the crystallographic elements of symmetry (rotations, reflections and translations) but also the time-inversion element, which causes the reversal of the magnetic moment density vector $\mathbf{m}(\mathbf{r})$. Following Landau & Lifshitz (1957), we shall denote this element by R. If combined with any crystallographic symmetry element G we get a product RG, which some authors call the space-time symmetry operator. We shall not use this terminology in the following.

To describe the symmetry properties of magnetics, one should use magnetic point and space groups instead of crystallographic ones. (See also Section 1.2.5.)

By investigating the 'four-dimensional groups of three-dimensional space', Heesch (1930) found not only the 122 groups that now are known as magnetic point groups but also the seven triclinic and 91 monoclinic magnetic space groups. He also recognized that these groups can be used to describe the symmetry of spin arrangements. The present interest in magnetic symmetry was much stimulated by Shubnikov (1951), who considered the symmetry groups of figures with black and white faces, which he called antisymmetry groups. The change of colour of the faces in antisymmetry (black–white symmetry, see also Section 3.3.5) corresponds to the element R. These antisymmetry classes were derived as magnetic symmetry point groups by Tavger & Zaitsev (1956). Beside antisymmetry, the concept of colour (or generalized) symmetry also was developed, in which the number of colours is not 2 but 3, 4 or 6 (see Belov *et al.*, 1964; Koptsik & Kuzhukeev, 1972). A different generalization to more than two colours was proposed by van der Waerden & Burckhardt (1961). The various approaches have been compared by Schwarzenberger (1984).

Table 1.5.2.1. *Comparison of different symbols for magnetic point groups*

Schoenflies	Hermann–Mauguin	Shubnikov	
$\boldsymbol{D}_{4R}$	$4221'$	$4{:}21'$	$4{:}2\underline{1}$
$\boldsymbol{D}_4$	422	4:2	4:2
$\boldsymbol{D}_4(\boldsymbol{C}_4)$	$42'2'$	$4{:}2'$	$4{:}\underline{2}$
$\boldsymbol{D}_4(\boldsymbol{D}_2)$	$4'22'$	$4'{:}2$	$\underline{4}{:}2$

As the theories of antisymmetry and of magnetic symmetry evolved often independently, different authors denote the operation of time inversion (black–white exchange) by different symbols. Of the four frequently used symbols ($R = E' = \underline{1} = 1'$) we shall use in this article only two: R and $1'$.

1.5.2.1. *Magnetic point groups*

Magnetic point groups may contain rotations, reflections, the element R and their combinations. A set of such elements that satisfies the group properties is called a magnetic point group. It is obvious that there are 32 trivial magnetic point groups; these are the ordinary crystallographic point groups supplemented by the element R. Each of these point groups contains all the elements of the ordinary point group $\mathcal{P}$ and also all the elements of this group $\mathcal{P}$ multiplied by R. This type of magnetic point group $\mathcal{M}_{P1}$ can be represented by

$$\mathcal{M}_{P1} = \mathcal{P} + R\mathcal{P}. \qquad (1.5.2.1)$$

These groups are sometimes called 'grey' magnetic point groups. As pointed out above, all dia- and paramagnets belong to this type of point group. To this type belong also antiferromagnets with a magnetic space group that contains translations multiplied by R (space groups of type III^b).

The second type of magnetic point group, which is also trivial in some sense, contains all the 32 crystallographic point groups without the element R in any form. For this type $\mathcal{M}_{P2} = \mathcal{P}$. Thirteen of these point groups allow ferromagnetic spontaneous magnetization (ferromagnetism, ferrimagnetism, weak ferromagnetism). They are listed in Table 1.5.2.4. The remaining 19 point groups describe antiferromagnets. The groups $\mathcal{M}_{P2}$ are often called 'white' magnetic point groups.

The third type of magnetic point group $\mathcal{M}_{P3}$, 'black and white' groups (which are the only nontrivial ones), contains those point groups in which R enters only in combination with rotations or reflections. There are 58 point groups of this type. Eighteen of them describe different types of ferromagnetism (see Table 1.5.2.4) and the others represent antiferromagnets.

Replacing R by the identity element E in the magnetic point groups of the third type does not change the number of elements in the point group. Thus each group of the third type $\mathcal{M}_{P3}$ is isomorphic to a group $\mathcal{P}$ of the second type.

The method of derivation of the nontrivial magnetic groups given below was proposed by Indenbom (1959). Let $\mathcal{H}$ denote the set of those elements of the group $\mathcal{P}$ which enter into the asso-

Table 1.5.2.2. *Comparison of different symbols for the elements of magnetic point groups*

Magnetic point group	Elements	
	Schoenflies	Hermann–Mauguin
$\boldsymbol{D}_{4R} = 4221'$	$E, C_2, 2C_4, 2U_2, 2U_2^a,$ $R, RC_2, 2RC_4, 2RU_2, 2RU_2^a$	$1, 2_x, 2_y, 2_z, 2_{xy}, 2_{-xy}, \pm 4_z,$ $1', 2'_x, 2'_y, 2'_z, 2'_{xy}, 2'_{-xy}, \pm 4'_z$
$\boldsymbol{D}_4 = 422$	$E, C_2, 2C_4, 2U_2, 2U_2^a$	$1, 2_x, 2_y, 2_z, 2_{xy}, 2_{-xy}, \pm 4_z$
$\boldsymbol{D}_4(\boldsymbol{C}_4) = 42'2'$	$E, C_2, 2C_4, 2RU_2, 2RU_2^a$	$1, 2_z, \pm 4_z, 2'_x, 2'_y, 2'_{xy}, 2'_{-xy}$
$\boldsymbol{D}_4(\boldsymbol{D}_2) = 4'22'$	$E, C_2^z, C_2^y, C_2^x, 2RU_2^a, 2RC_4$	$1, 2_x, 2_y, 2_z, 2'_{xy}, 2'_{-xy}, \pm 4'_z$

1.6. Classical linear crystal optics

By A. M. Glazer and K. G. Cox†

1.6.1. Introduction

The field of classical crystal optics is an old one, and in the last century, in particular, it was the main subject of interest in the study of crystallography. Since the advent of X-ray diffraction, however, crystal optics tended to fall out of widespread use, except perhaps in mineralogy, where it has persisted as an important technique for the classification and identification of mineral specimens. In more recent times, however, with the growth in optical communications technologies, there has been a revival of interest in the optical properties of crystals, both linear and nonlinear. There are many good books dealing with classical crystal optics, which the reader is urged to consult (Hartshorne & Stuart, 1970; Wahlstrom, 1959; Bloss, 1961). In addition, large collections of optical data on crystals exist (Groth, 1906–1919; Winchell, 1931, 1939, 1951, 1954, 1965; Kerr, 1959). In this chapter, both linear and nonlinear optical effects will be introduced briefly in a generalized way. Then the classical derivation of the refractive index surface for a crystal will be derived. This leads on to a discussion on the practical means by which conventional crystal optics can be used in the study of crystalline materials, particularly in connection with mineralogical study, although the techniques described apply equally well to other types of crystals. Finally, some detailed explanations of certain linear optical tensors will be given.

1.6.2. Generalized optical, electro-optic and magneto-optic effects

When light of a particular cyclic frequency ω is incident on a crystal of the appropriate symmetry, in general an electrical polarization **P** may be generated within the crystal. This can be expressed in terms of a power series with respect to the electric vector of the light wave (Nussbaum & Phillips, 1976; Butcher & Cotter, 1990; Kaminow, 1974):

$$P = \sum \varepsilon_o \chi^{(i)} E^i = \varepsilon_o \left(\chi^{(1)} E + \chi^{(2)} E^2 + \chi^{(3)} E^3 + \ldots\right), \quad (1.6.2.1)$$

where the $\chi^{(i)}$ are susceptibilities of order i. Those working in the field of electro-optics tend to use this notation as a matter of course. The susceptibility $\chi^{(1)}$ is a linear term, whereas the higher-order susceptibilities describe nonlinear behaviour.

However, it is convenient to generalize this concept to take into account other fields (*e.g.* electrical, magnetic and stress fields) that can be imposed on the crystal, not necessarily due to the incident light. The resulting polarization can be considered to arise from many different so-called electro-optic, magneto-optic and photoelastic (elasto-optic) effects, expressed as a series expansion of P_i in terms of susceptibilities $\chi_{ijk\ell\ldots}$ and the applied fields **E**, **B** and T. This can be written in the following way:

$$\begin{aligned} P_i = P_i^0 &+ \varepsilon_o \chi_{ij} E_j^\omega + \varepsilon_o \chi_{ij\ell} \nabla_\ell E_j^\omega + \varepsilon_o \chi_{ijk} E_j^{\omega_1} E_k^{\omega_2} \\ &+ \varepsilon_o \chi_{ijk\ell} E_j^{\omega_1} E_k^{\omega_2} E_\ell^{\omega_3} + \varepsilon_o \chi_{ijk} E_j^{\omega_1} B_k^{\omega_2} \\ &+ \varepsilon_o \chi_{ijk\ell} E_j^{\omega_1} B_k^{\omega_2} B_\ell^{\omega_3} + \varepsilon_o \chi_{ijk\ell} E_j^{\omega_1} T_{k\ell}^{\omega_2} + \ldots . \end{aligned} \quad (1.6.2.2)$$

Here, the superscripts refer to the frequencies of the relevant field terms and the susceptibilities are expressed as tensor components. Each term in this expansion gives rise to a specific effect that may or may not be observed, depending on the crystal symmetry and the size of the susceptibility coefficients. Note a possible confusion: in the notation $\chi^{(i)}$, i is equal to one less than its rank. It is important to understand that these terms describe various properties, both linear and nonlinear. Those terms that describe the effect purely of optical frequencies propagating through the crystal give rise to *linear* and *nonlinear* optics. In the former case, the input and output frequencies are the same, whereas in the latter case, the output frequency results from sums or differences of the input frequencies. Furthermore, it is apparent that nonlinear optics depends on the intensity of the input field, and so is an effect that is induced by the strong optical field.

If the input electrical fields are static (the term 'static' is used here to mean zero or low frequency compared with that of light), the resulting effects are either linear or nonlinear electrical effects, in which case they are of no interest here. There is, however, an important class of effects in which both static and optical fields are involved: linear and nonlinear electro-optic effects. Here, the use of the terms linear and nonlinear is open to confusion, depending on whether it is the electrical part or the optical part to which reference is made (see for example below in the discussion of the linear electro-optic effect). Similar considerations apply to applied magnetic fields to give linear and nonlinear magneto-optic effects and to applied stresses, the *photoelastic* effects. Table 1.6.2.1 lists the most important effects according to the terms in this series. The susceptibilities are written in the form $\chi(\omega_1; \omega_2, \omega_3, \ldots)$ to indicate the frequency ω_1 of the output electric field, followed after the semicolon by the input frequencies $\omega_1, \omega_2, \ldots$.

Table 1.6.2.1. *Summary of linear and nonlinear optical properties*

Type of polarization term	Susceptibility	Effect
P_i^0	$\chi(0; 0)$	Spontaneous polarization
$\varepsilon_o \chi_{ij} E_j^\omega$	$\chi(\omega; \omega)$	Dielectric polarization, refractive index, linear birefringence
$\varepsilon_o \chi_{ij\ell} \nabla_\ell E_j^\omega$	$\chi(\omega; \omega)$	Optical rotation (gyration)
$\varepsilon_o \chi_{ijk} E_j^{\omega_1} E_k^{\omega_2}$	$\chi(0; 0, 0)$	Quadratic electric effect
	$\chi(\omega; \omega, 0)$	Linear electro-optic effect or Pockels effect
	$\chi(\omega_1 \pm \omega_2; \omega_1, \omega_2)$	Sum/difference frequency generation, two-wave mixing
	$\chi(\omega; \omega/2, \omega/2)$	Second harmonic generation (SHG)
	$\chi(0; \omega/2, \omega/2)$	Optical rectification
	$\chi(\omega_3; \omega_1, \omega_2)$	Parametric amplification
$\varepsilon_o \chi_{ijk\ell} E_j^{\omega_1} E_k^{\omega_2} E_\ell^{\omega_3}$	$\chi(\omega; 0, 0)$	Quadratic electro-optic effect or Kerr effect
	$\chi(\omega; \omega/2, \omega/2, 0)$	Electric-field induced second harmonic generation (EFISH)
	$\chi(-\omega_1; \omega_2, \omega_3, -\omega_4)$	Four-wave mixing
$\varepsilon_o \chi_{ijk} E_j^{\omega_1} B_k^{\omega_2}$	$\chi(\omega; \omega, 0)$	Faraday rotation
$\varepsilon_o \chi_{ijk\ell} E_j^{\omega_1} B_k^{\omega_2} B_\ell^{\omega_3}$	$\chi(\omega; \omega, 0, 0)$	Quadratic magneto-optic effect or Cotton–Mouton effect
$\varepsilon_o \chi_{ijk\ell} E_j^{\omega_1} T_{k\ell}^{\omega_2}$	$\chi(\omega; \omega, 0)$	Linear elasto-optic effect or photoelastic effect
	$\chi(\omega_1 \pm \omega_2; \omega_1, \omega_2)$	Linear acousto-optic effect

† The sudden death of Keith Cox is deeply regretted. He died in a sailing accident on 27 August 1998 in Scotland at the age of 65.

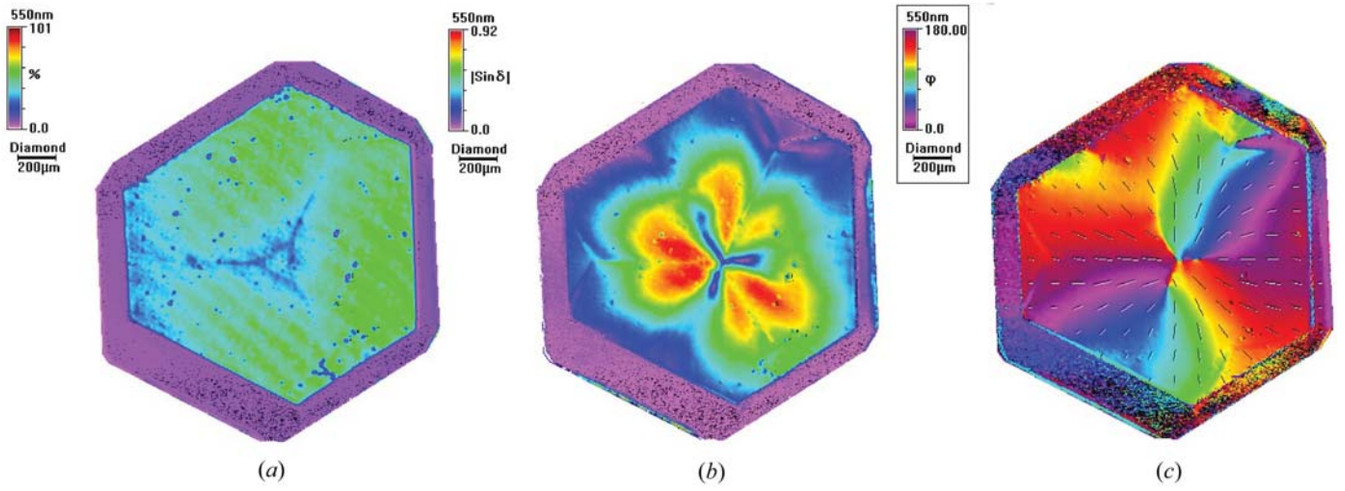

Fig. 1.6.4.7. Three birefringence images of industrial diamond viewed along [111] taken with the rotating analyser system. (*a*) I_0; (*b*) $|\sin\delta|$; (*c*) orientation φ of slow axis with respect to horizontal.

images observed in plane-polarized light rely on scattering from point sources within the specimen, and do not depend strictly on whether the configuration is conoscopic or orthoscopic. Nevertheless, relief and the Becke line are much more clearly observable in orthoscopic use.

The principle of conoscopic use is quite different. Here, the image is formed in the *back focal plane* of the objective. Any group of parallel rays passing through the specimen is brought to a focus in this plane, at a specific point depending on the direction of transmission. Hence every point in the image corresponds to a different transmission direction (see Fig. 1.6.4.8). Moreover, the visible effects are entirely caused by interference, and there is no image of the details of the specimen itself. That image is of course also present, towards the top of the tube at or near the cross wires, but the two are not simultaneously visible. The conoscopic image may be viewed simply by removing the eyepiece and looking down the tube, where it appears as a small but bright circle. More commonly however, the Bertrand lens is inserted in the tube, which has the effect of transferring the conoscopic image from the back focal plane of the objective to the front focal plane of the eyepiece, where it coincides with the cross wires and may be examined as usual.

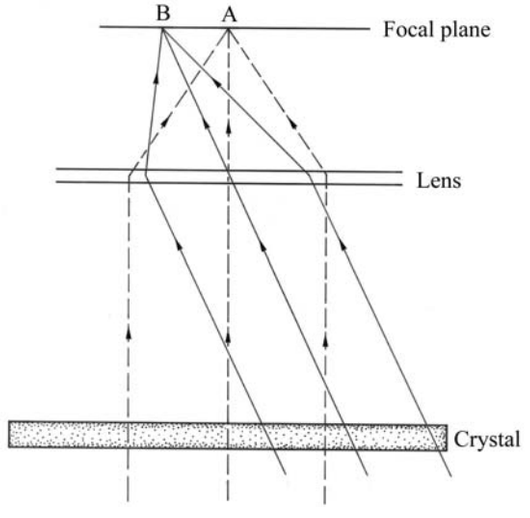

Fig. 1.6.4.8. Formation of the interference figure. The microscope axis lies vertically in the plane of the paper. A bundle of rays travelling through the crystal parallel to the microscope axis (dashed lines) is brought to a focus at A in the back focal plane of the objective. This is the centre of the interference figure. A bundle of oblique rays (solid lines) is brought to a focus at B, towards the edge of the figure.

It is useful to think of the conoscopic image as analogous to the gnomonic projection as used in crystallography. The geometrical principles are the same, as each direction through the crystal is projected directly through the centre of the lens into the back focal plane.

1.6.4.12. *Uniaxial figures*

To understand the formation of an interference figure, consider a simple example, a specimen of calcite cut at right angles to the *c* crystallographic axis. Calcite is uniaxial negative, with the optic axis parallel to **c**. The rays that have passed most obliquely through the specimen are focused around the edge of the figure, while the centre is occupied by rays that have travelled parallel to the optic axis (see Fig. 1.6.4.8). The birefringence within the image clearly must increase from nil in the centre to some higher value at the edges, because the rays here have had longer path lengths through the crystal. Furthermore, the image must have radial symmetry, so that the first most obvious feature of the figure is a series of coloured rings, corresponding in outward sequence to the successive orders. The number of rings visible will of course depend on the thickness of the sample, and when birefringence is low enough no rings will be obvious because all colours lie well within the first order (Figs. 1.6.4.9*a* and *b*). Fig. 1.6.4.10(*a*) illustrates, by reference to the indicatrix, the way in which the vibration directions of the *o* and *e* rays are disposed. Fig. 1.6.4.10(*b*) shows the disposition of vibration directions in the figure. Note that *o* rays always vibrate tangentially and *e* rays radially. The *o*-ray vibration directions lie in the plane of the figure, but *e*-ray vibration directions become progressively more inclined to the plane of the figure towards the edge.

The shaded cross on the figure illustrates the position of dark 'brushes' known as *isogyres* (Fig. 1.6.4.10*b*). These develop wherever vibration directions lie N–S or E–W, hence corresponding to the vibration directions of the analyser and polarizer. As the stage is rotated, as long as the optic axis is truly parallel to the microscope axis, the figure will not change. This is an example of a centred uniaxial optic axis figure, and such a figure identifies the crystal as belonging to the tetragonal, trigonal or hexagonal systems (see Fig. 1.6.4.11*a*).

From the point of crystal identification, one can also determine whether the figure coincides with the uniaxial positive ($n_e > n_o$) or uniaxial negative ($n_e < n_o$) cases. Inserting the sensitive-tint plate will move the coloured ring up or down the birefringence scale by a complete order. Fig. 1.6.4.11(*c*) shows the centred optic axis figure for calcite, which is optically negative. The insertion of a tint plate with its slow vibration direction lying NE–SW lowers the colours in the NE and SW quadrants of the figure, and raises

1.7. Nonlinear optical properties

By B. Boulanger and J. Zyss

1.7.1. Introduction

The first nonlinear optical phenomenon was observed by Franken *et al.* (1961): ultraviolet radiation at 0.3471 μm was detected at the exit of a quartz crystal illuminated with a ruby laser beam at 0.6942 μm. This was the first demonstration of second harmonic generation at optical wavelengths. A coherent light of a few W cm^{-2} is necessary for the observation of nonlinear optical interactions, which thus requires the use of laser beams.

The basis of nonlinear optics, including quantum-mechanical perturbation theory and Maxwell equations, is given in the paper published by Armstrong *et al.* (1962).

It would take too long here to give a complete historical account of nonlinear optics, because it involves an impressive range of different aspects, from theory to applications, from physics to chemistry, from microscopic to macroscopic aspects, from quantum mechanics of materials to classical and quantum electrodynamics, from gases to solids, from mineral to organic compounds, from bulk to surface, from waveguides to fibres and so on.

Among the main nonlinear optical effects are harmonic generation, parametric wave mixing, stimulated Raman scattering, self-focusing, multiphoton absorption, optical bistability, phase conjugation and optical solitons.

This chapter deals mainly with harmonic generation and parametric interactions in anisotropic crystals, which stand out as one of the most important fields in nonlinear optics and certainly one of its oldest and most rigorously treated topics. Indeed, there is a great deal of interest in the development of solid-state laser sources, be they tunable or not, in the ultraviolet, visible and infrared ranges. Spectroscopy, telecommunications, telemetry and optical storage are some of the numerous applications.

The electric field of light interacts with the electric field of matter by inducing a dipole due to the displacement of the electron density away from its equilibrium position. The induced dipole moment is termed polarization and is a vector: it is related to the applied electric field *via* the dielectric susceptibility tensor. For fields with small to moderate amplitude, the polarization remains linearly proportional to the field magnitude and defines the linear optical properties. For increasing field amplitudes, the polarization is a nonlinear function of the applied electric field and gives rise to nonlinear optical effects. The polarization is properly modelled by a Taylor power series of the applied electric field if its strength does not exceed the atomic electric field (10^8–10^9 V cm^{-1}) and if the frequency of the electric field is far away from the resonance frequencies of matter. Our purpose lies within this framework because it encompasses the most frequently encountered cases, in which laser intensities remain in the kW to MW per cm^2 range, that is to say with electric fields from 10^3 to 10^4 V cm^{-1}. The electric field products appearing in the Taylor series express the interactions of different optical waves. Indeed, a wave at the circular frequency ω can be radiated by the second-order polarization induced by two waves at ω_a and ω_b such as $\omega = \omega_a \pm \omega_b$: these interactions correspond to sum-frequency generation ($\omega = \omega_a + \omega_b$), with the particular cases of second harmonic generation ($2\omega_a = \omega_a + \omega_a$) and indirect third harmonic generation ($3\omega_a = \omega_a + 2\omega_a$); the other three-wave process is difference-frequency generation, including optical parametric amplification and optical parametric oscillation. In the same way, the third-order polarization governs four-wave mixing: direct third harmonic generation ($3\omega_a = \omega_a + \omega_a + \omega_a$) and more generally sum- and difference-frequency generations ($\omega = \omega_a \pm \omega_b \pm \omega_c$).

Here, we do not consider optical interactions at the microscopic level, and we ignore the way in which the atomic or molecular dielectric susceptibility determines the macroscopic optical properties. Microscopic solid-state considerations and the relations between microscopic and macroscopic optical properties, particularly successful in the realm of organic crystals, play a considerable role in materials engineering and optimization. This important topic, known as molecular and crystalline engineering, lies beyond the scope of this chapter. Therefore, all the phenomena studied here are connected to the macroscopic first-, second- and third-order dielectric susceptibility tensors $\chi^{(1)}$, $\chi^{(2)}$ and $\chi^{(3)}$, respectively; we give these tensors for all the crystal point groups.

We shall mainly emphasize propagation aspects, on the basis of Maxwell equations which are expressed for each Fourier component of the optical field in the nonlinear crystal. The reader will then follow how the linear optical properties come to play a pivotal role in the nonlinear optical interactions. Indeed, an efficient quadratic or cubic interaction requires not only a high magnitude of $\chi^{(2)}$ or $\chi^{(3)}$, respectively, but also specific conditions governed by $\chi^{(1)}$: existence of phase matching between the induced nonlinear polarization and the radiated wave; suitable symmetry of the field tensor, which is defined by the tensor product of the electric field vectors of the interacting waves; and small or nil double refraction angles. Quadratic and cubic processes cannot be considered as fully independent in the context of cascading. Significant phase shifts driven by a sequence of sum- and difference-frequency generation processes attached to a $\chi^{(2)} \cdot \chi^{(2)}$ contracted tensor expression have been reported (Bosshard, 2000). These results point out the relevance of polar structures to cubic phenomena in both inorganic and organic structures, thus somewhat blurring the borders between quadratic and cubic NLO.

We analyse in detail second harmonic generation, which is the prototypical interaction of frequency conversion. We also present indirect and direct third harmonic generations, sum-frequency generation and difference-frequency generation, with the specific cases of optical parametric amplification and optical parametric oscillation.

An overview of the methods of measurement of the nonlinear optical properties is provided, and the chapter concludes with a comparison of the main mineral and organic crystals showing nonlinear optical properties.

1.7.2. Origin and symmetry of optical nonlinearities

1.7.2.1. *Induced polarization and susceptibility*

The macroscopic electronic polarization of a unit volume of the material system is classically expanded in a Taylor power series of the applied electric field **E**, according to Bloembergen (1965):

$$\mathbf{P} = \mathbf{P}_0 + \varepsilon_o(\chi^{(1)} \cdot \mathbf{E} + \chi^{(2)} \cdot \mathbf{E}^2 + \ldots + \chi^{(n)} \cdot \mathbf{E}^n + \ldots), \tag{1.7.2.1}$$

where $\chi^{(n)}$ is a tensor of rank $n+1$, $\mathbf{E}^n$ is a shorthand abbreviation for the nth order tensor product $\mathbf{E} \otimes \mathbf{E} \otimes \ldots \otimes \mathbf{E} = \otimes^n \mathbf{E}$ and the dot stands for the contraction of the last n indices of the

Table 1.7.3.9. *Field-tensor components specifically nil in the principal planes of uniaxial and biaxial crystals for three-wave and four-wave interactions* $(i, j, k) = x, y$ or z.

Configurations of polarization	Nil field-tensor components		
	(xy) plane	(xz) plane	(yz) plane
eoo	$F_{xjk} = 0$; $F_{yjk} = 0$	$F_{ixk} = F_{ijx} = 0$ $F_{yjk} = 0$	$F_{iyk} = F_{ijy} = 0$ $F_{xjk} = 0$
oee	$F_{ixk} = F_{ijx} = 0$ $F_{iyk} = F_{ijy} = 0$	$F_{iyk} = F_{ijy} = 0$ $F_{xik} = 0$	$F_{ixk} = F_{ijx} = 0$ $F_{yjk} = 0$
eooo	$F_{xjkl} = 0$; $F_{yjkl} = 0$	$F_{ixkl} = F_{ijxl} = F_{ijkx} = 0$ $F_{yjkl} = 0$	$F_{iykl} = F_{ijyl} = F_{ijky} = 0$ $F_{xjkl} = 0$
oeee	$F_{ixkl} = F_{ijxl} = F_{ijkx} = 0$ $F_{iykl} = F_{ijyl} = F_{ijky} = 0$	$F_{iykl} = F_{ijyl} = F_{ijky} = 0$ $F_{xjkl} = 0$	$F_{ixkl} = F_{ijxl} = F_{ijkx} = 0$ $F_{yjkl} = 0$
ooee	$F_{ijxl} = F_{ijkx} = 0$ $F_{ijyl} = F_{ijky} = 0$	$F_{xjkl} = F_{ixkl} = 0$ $F_{ijyl} = F_{ijky} = 0$	$F_{yjkl} = F_{iykl} = 0$ $F_{ijxl} = F_{ijkx} = 0$

and configurations of polarization: D_4 and D_6 for 2*o.e*, C_{4v} and C_{6v} for 2*e.o*, D_6, D_{6h}, D_{3h} and C_{6v} for 3*o.e* and 3*e.o*. Thus, even if phase-matching directions exist, the effective coefficient in these situations is nil, which forbids the interactions considered (Boulanger & Marnier, 1991; Boulanger *et al.*, 1993). The number of forbidden crystal classes is greater under the Kleinman approximation. The forbidden crystal classes have been determined for the particular case of third harmonic generation assuming Kleinman conjecture and without consideration of the field tensor (Midwinter & Warner, 1965).

1.7.3.2.4.3. *Biaxial class*

The symmetry of the biaxial field tensors is the same as for the uniaxial class, though only for a propagation in the principal planes *xz* and *yz*; the associated matrix representations are given in Tables 1.7.3.7 and 1.7.3.8, and the nil components are listed in Table 1.7.3.9. Because of the change of optic sign from either side of the optic axis, the field tensors of the interactions for which the phase-matching cone joins areas *b* and *a* or *a* and *c*, given in Fig. 1.7.3.5, change from one area to another: for example, the field tensor (*eoee*) becomes an (*oeoo*) and so the solicited components of the electric susceptibility tensor are not the same.

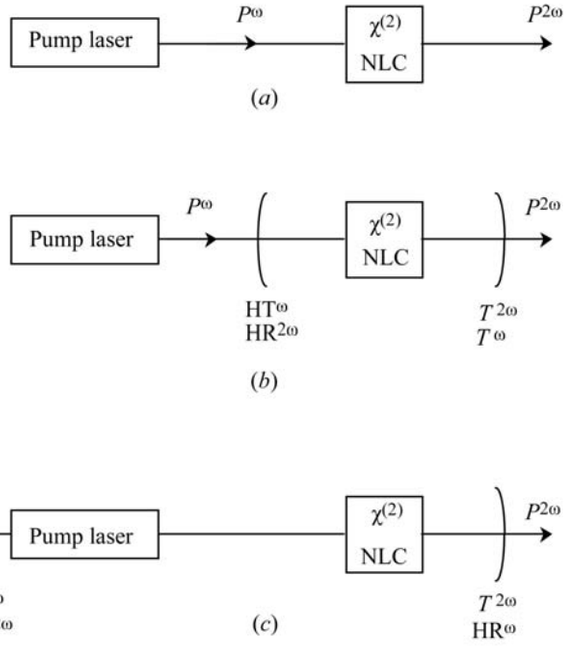

Fig. 1.7.3.6. Schematic configurations for second harmonic generation: (*a*) non-resonant SHG; (*b*) external resonant SHG: the resonant wave may either be the fundamental or the harmonic one; (*c*) internal resonant SHG. $P^{\omega,2\omega}$ are the fundamental and harmonic powers; HT^{ω} and $HR^{\omega,2\omega}$ are the high-transmission and high-reflection mirrors at ω or 2ω and $T^{\omega,2\omega}$ are the transmission coefficients of the output mirror at ω or 2ω. NLC is the nonlinear crystal with a nonzero $\chi^{(2)}$.

The nonzero field-tensor components for a propagation in the *xy* plane of a biaxial crystal are: F_{zxx}, F_{zyy}, $F_{zxy} \neq F_{zyx}$ for (*eoo*); F_{xzz}, F_{yzz} for (*oee*); F_{zxxx}, F_{zyyy}, $F_{zxyy} \neq F_{zyxy} \neq F_{zyyx}$, $F_{zxxy} \neq F_{zxyx} \neq F_{zyxx}$ for (*eooo*); F_{xzzz}, F_{yzzz} for (*oeee*); $F_{xyzz} \neq F_{yxzz}$, F_{xxzz}, F_{yyzz} for (*ooee*). The nonzero components for the other configurations of polarization are obtained by the associated permutations of the Cartesian indices and the corresponding polarizations.

The field tensors are not symmetric for a propagation out of the principal planes in the general case where all the frequencies are different: in this case there are 27 independent components for the three-wave interactions and 81 for the four-wave interactions, and so all the electric susceptibility tensor components are solicited.

As phase matching imposes the directions of the electric fields of the interacting waves, it also determines the field tensor and hence the effective coefficient. Thus there is no possibility of choice of the $\chi^{(2)}$ coefficients, since a given type of phase matching is considered. In general, the largest coefficients of polar crystals, *i.e.* χ_{zzz}, are implicated at a very low level when phase matching is achieved, because the corresponding field tensor, *i.e.* F_{zzz}, is often weak (Boulanger *et al.*, 1997). In contrast, QPM authorizes the coupling between three waves polarized along the z axis, which leads to an effective coefficient which is purely χ_{zzz}, *i.e.* $\chi_{\text{eff}} = (2/\pi)\chi_{zzz}$, where the numerical factor comes from the periodic character of the rectangular function of modulation (Fejer *et al.*, 1992).

1.7.3.3. *Integration of the propagation equations*

1.7.3.3.1. *Spatial and temporal profiles*

The resolution of the coupled equations (1.7.3.22) or (1.7.3.24) over the crystal length L leads to the electric field amplitude $E_i(X, Y, L)$ of each interacting wave. The general solutions are Jacobian elliptic functions (Armstrong *et al.*, 1962; Fève, Boulanger & Douady, 2002). The integration of the systems is simplified for cases where one or several beams are held constant, which is called the undepleted pump approximation. We consider mainly this kind of situation here. The power of each interacting wave is calculated by integrating the intensity over the cross section of each beam according to (1.7.3.8). For our main purpose, we consider the simple case of plane-wave beams with two kinds of transverse profile:

$$\begin{aligned} &\mathbf{E}(X, Y, Z) = \mathbf{e}E_o(Z) \quad \text{for } (X, Y) \in [-w_o, +w_o] \\ &\mathbf{E}(X, Y, Z) = 0 \qquad\quad \text{elsewhere} \end{aligned} \tag{1.7.3.36}$$

for a flat distribution over a radius w_o;

$$\mathbf{E}(X, Y, Z) = \mathbf{e}E_o(Z)\exp[-(X^2 + Y^2)/w_o^2] \tag{1.7.3.37}$$

for a Gaussian distribution, where w_o is the radius at $(1/e)$ of the electric field and so at $(1/e^2)$ of the intensity.

$$\rho(T) = \rho_i(1 + BT^2) + AT^2. \qquad (1.8.3.14)$$

The term ρ_i is the constant due to the impurity scattering. There is also a term proportional to BT^2, which is proportional to the impurity resistance. This factor is due to the Koshino–Taylor effect (Koshino, 1960; Taylor, 1964), which has been treated rigorously by Mahan & Wang (1989). It is the inelastic scattering of electrons by impurities. The impurity is part of the lattice and phonons can be excited when the impurity scatters the electrons. The term AT^2 is due to electron–electron interactions. The Coulomb interaction between electrons is highly screened and makes only a small contribution to A. The largest contribution to A is caused by phonons. MacDonald *et al.* (1981) showed that electrons can interact by exchanging phonons. There are also terms due to boundary scattering, which is important in thin films: see Bruls *et al.* (1985).

Note that (1.8.3.14) has no term from phonons of $O(T^5)$. Such a term is lacking in simple metals, contrary to the assertion in most textbooks. Its absence is due to *phonon drag*. For a review and explanation of this behaviour, see Wiser (1984). The T^5 term is found in the noble metals, where phonon drag is less important owing to the complexities of the Fermi surface.

1.8.3.2. *Metal alloys*

Alloys are solids composed of a mixture of two or more elements that do not form a stoichiometric compound. An example is Cu_xNi_{1-x}, in which x can have any value. For small values of x, or of $(1 - x)$, the atoms of one element just serve as impurities in the other element. This results in the type of behaviour described above. However, in the range $0.2 < x < 0.8$, a different type of resistivity is found. This was first summarized by Mooij (1973), who found a remarkable range of behaviours. He measured the resistivity of hundreds of alloys and also surveyed the published literature for additional results. He represented the resistivity at $T = 300$ K by two values: the resistivity itself, $\rho(T = 300)$, and its logarithmic derivative, $\alpha = \mathrm{d}\ln(\rho)/\mathrm{d}T$. He produced the graph shown in Fig. 1.8.3.2, where these two values are plotted against each other. Each point is one sample as represented by these two numbers. He found that all of the results fit within a band of numbers, in which larger values of $\rho(T = 300)$ are accompanied by negative values of α. Alloys with very high values of resistivity generally have a resistivity $\rho(T)$ that decreases with increasing temperature. The region where $\alpha = 0$ corresponds to a resistivity of $\rho^* = 150\ \mu\Omega$ cm, which appears to be a fixed point. As the temperature is increased, the resisitivities of alloys with $\rho > \rho^*$ decrease to this value, while the resisitivities of alloys with $\rho < \rho^*$ increase to this value.

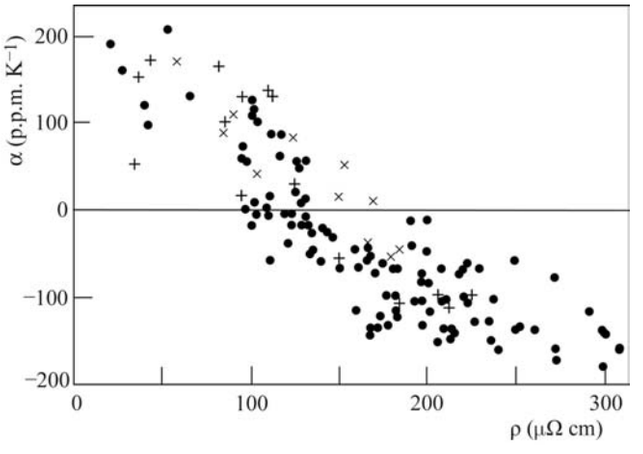

Fig. 1.8.3.2. The temperature coefficient of resistance *versus* resistivity for alloys according to Mooij (1973). Data are shown for bulk alloys (+), thin films (•) and amorphous alloys (×).

Mooij's observations are obviously important, but the reason for this behaviour is not certain. Several different explanations have been proposed and all are plausible: see Jonson & Girvin (1979), Allen & Chakraborty (1981) or Tsuei (1986).

Recently, another group of alloys have been found that are called *bad metals*. The ruthenates (see Allen *et al.*, 1996; Klein *et al.*, 1996) have a resistivity $\rho > \rho^*$ that increases at high temperatures. Their values are outliers on Mooij's plot.

1.8.3.3. *Semiconductors*

The resistivity of semiconductors varies from sample to sample, even of the same material. The conductivity can be written as $\sigma = n_0 e\mu$, where e is the charge on the electron, $\mu = e\tau/m^*$ is the mobility and n_0 is the density of conducting particles (electrons or holes). It is the density of particles n_0 that varies from sample to sample. It depends upon the impurity content of the semiconductor as well as upon temperature. Since no two samples have exactly the same number of impurities, they do not have the same values of n_0. In semiconductors and insulators, the conducting particles are extrinsic – they come from defects, impurities or thermal excitation – in contrast to metals, where the density of the conducting electrons is usually an intrinsic property.

In semiconductors, instead of talking about the conductivity, the more fundamental transport quantity (Rode, 1975) is the mobility μ. It is the same for each sample at high temperature if the density of impurities and defects is low. There is an intrinsic mobility, which can be calculated assuming there are no impurities and can be measured in samples with a very low density of impurities. We shall discuss the intrinsic mobility first.

Fig. 1.8.3.3 shows the intrinsic mobility of electrons in silicon, from Rode (1972), as a function of temperature. The mobility generally decreases with increasing temperature. This behaviour is found in all common semiconductors. The mobility also decreases with an increasing concentration of impurities: see Jacoboni *et al.* (1977).

The intrinsic mobility of semiconductors is due to the scattering of electrons and holes by phonons. The phonons come in various branches called TA, LA, TO and LO, where T is transverse, L is longitudinal, A is acoustic and O is optical. At long wavelengths, the acoustic modes are just the sound waves, which

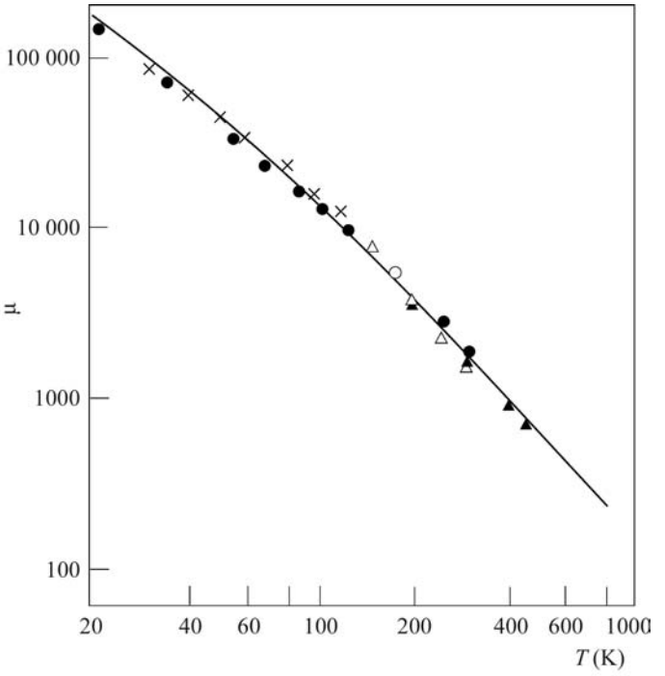

Fig. 1.8.3.3. The intrinsic mobility of electrons in silicon. Solid line: theory; points: experimental. After Rode (1972).

1.9. Atomic displacement parameters

By W. F. Kuhs

1.9.1. Introduction

Atomic thermal motion and positional disorder is at the origin of a systematic intensity reduction of Bragg reflections as a function of scattering vector **Q**. The intensity reduction is given as the well known *Debye–Waller factor* (DWF); the DWF may be of purely thermal origin (*thermal DWF* or *temperature factor*) or it may contain contributions of static atomic disorder (*static DWF*). As atoms of chemically or isotopically different elements behave differently, the individual atomic contributions to the global DWF (describing the weakening of Bragg intensities) vary. Formally, one may split the global DWF into the individual atomic contributions. Crystallographic experiments usually measure the global weakening of Bragg intensities and the individual contributions have to be assessed by adjusting individual atomic parameters in a least-squares refinement.

The theory of lattice dynamics (see *e.g.* Willis & Pryor, 1975) shows that the atomic thermal DWF T_α is given by an exponential of the form

$$T_\alpha(\mathbf{Q}) = \langle \exp(i\mathbf{Q}\mathbf{u}_\alpha)\rangle, \tag{1.9.1.1}$$

where $\mathbf{u}_\alpha$ are the individual atomic displacement vectors and the brackets symbolize the thermodynamic (time–space) average over all contributions $\mathbf{u}_\alpha$. In the harmonic (Gaussian) approximation, (1.9.1.1) reduces to

$$T_\alpha(\mathbf{Q}) = \exp[(-1/2)\langle(\mathbf{Q}\mathbf{u}_\alpha)^2\rangle]. \tag{1.9.1.2}$$

The thermodynamically averaged atomic mean-square displacements (of thermal origin) are given as $U^{ij} = \langle u^i u^j\rangle$, *i.e.* they are the thermodynamic average of the product of the displacements along the i and j coordinate directions. Thus (1.9.1.2) may be expressed with $\mathbf{Q} = 4\pi\mathbf{h}|\mathbf{a}|$ in a form more familiar to the crystallographer as

$$T_\alpha(\mathbf{h}) = \exp(-2\pi^2 h_i|\mathbf{a}^i|h_j|\mathbf{a}^j|U^{ij}_\alpha), \tag{1.9.1.3}$$

where h_i are the covariant Miller indices, $\mathbf{a}^i$ are the reciprocal-cell basis vectors and $1 \le \iota, \varphi \le 3$. Here and in the following, tensor notation is employed; implicit summation over repeated indices is assumed unless stated otherwise. For computational convenience one often writes

$$T_\alpha(\mathbf{h}) = \exp(-h_i h_j \beta^{ij}_\alpha) \tag{1.9.1.4}$$

with $\beta^{ij}_\alpha = 2\pi^2|\mathbf{a}^i||\mathbf{a}^j|U^{ij}_\alpha$ (no summation). Both **h** and $\boldsymbol{\beta}$ are dimensionless tensorial quantities; **h** transforms as a covariant tensor of rank 1, $\boldsymbol{\beta}$ as a contravariant tensor of rank 2 (for details of the mathematical notion of a tensor, see Chapter 1.1).

Similar formulations are found for the static atomic DWF S_α, where the average of the atomic static displacements $\Delta\mathbf{u}_\alpha$ may also be approximated [though with weaker theoretical justification, see Kuhs (1992)] by a Gaussian distribution:

$$S_\alpha(\mathbf{Q}) = \exp[(-1/2)\langle(\mathbf{Q}\Delta\mathbf{u}_\alpha)^2\rangle]. \tag{1.9.1.5}$$

As in equation (1.9.1.3), the static atomic DWF may be formulated with the mean-square disorder displacements $\Delta U^{ij} = \langle \Delta u^i \Delta u^j\rangle$ as

$$S_\alpha(\mathbf{h}) = \exp(-2\pi^2 h_i|\mathbf{a}^i|h_j|\mathbf{a}^j|\Delta U^{ij}_\alpha). \tag{1.9.1.6}$$

It is usually difficult to separate thermal and static contributions, and it is often wise to use the sum of both and call them simply (mean-square) atomic displacements. A separation may however be achieved by a temperature-dependent study of atomic displacements. A harmonic diagonal tensor component of purely thermal origin extrapolates linearly to zero at 0 K; zero-point motion causes a deviation from this linear behaviour at low temperatures, but an extrapolation from higher temperatures (where the contribution from zero-point motion becomes negligibly small) still yields a zero intercept. Any positive intercept in such extrapolations is then due to a (temperature-independent) static contribution to the total atomic displacements. Care has to be taken in such extrapolations, as pronounced anharmonicity (frequently encountered at temperatures higher than the Debye temperature) will change the slope, thus invalidating the linear extrapolation (see *e.g.* Willis & Pryor, 1975). Owing to the difficulty in separating thermal and static displacements in a standard crystallographic structure analysis, a subcommittee of the IUCr Commission on Crystallographic Nomenclature has recommended the use of the term *atomic displacement parameters* (ADPs) for U^{ij} and β^{ij} (Trueblood *et al.*, 1996).

1.9.2. The atomic displacement parameters (ADPs)

One notes that in the Gaussian approximation, the mean-square atomic displacements (composed of thermal and static contributions) are fully described by six coefficients β^{ij}, which transform on a change of the direct-lattice base (according to $\mathbf{a}_k = A_{ki}\mathbf{a}_i$) as

$$\beta^{kl} = A_{ki}A_{lj}\beta^{ij}. \tag{1.9.2.1}$$

This is the transformation law of a tensor (see Section 1.1.3.2); the mean-square atomic displacements are thus tensorial properties of an atom α. As the tensor is contravariant and in general is described in a (non-Cartesian) crystallographic basis system, its indices are written as superscripts. It is convenient for comparison purposes to quote the dimensionless coefficients β^{ij} as their dimensioned representations U^{ij}.

In the harmonic approximation, the atomic displacements are fully described by the fully symmetric second-order tensor given in (1.9.2.1). Anharmonicity and disorder, however, cause deviations from a Gaussian distribution of the atomic displacements around the atomic position. In fact, anharmonicity in the thermal motion also provokes a shift of the atomic position as a function of temperature. A generalized description of atomic displacements therefore also involves first-, third-, fourth- and even higher-order displacement terms. These terms are defined by a moment-generating function $M(\mathbf{Q})$ which expresses $\langle(\exp(i\mathbf{Q}\mathbf{u}_\alpha)\rangle$ in terms of an infinite number of moments; for a Gaussian distribution of displacement vectors, all moments of order > 2 are identically equal to zero. Thus

$$M(\mathbf{Q}) = \langle \exp(i\mathbf{Q}\mathbf{u}_\alpha)\rangle = \sum_{N=0}^{\infty}(i^N/N!)\langle(\mathbf{Q}\mathbf{u}_\alpha)^N\rangle. \tag{1.9.2.2}$$

The moments $\langle(\mathbf{Q}\mathbf{u}_\alpha)^N\rangle$ of order N may be expressed in terms of cumulants $\langle(\mathbf{Q}\mathbf{u}_\alpha)^N\rangle_{\rm cum}$ by the identity

$$\sum_{N=0}^{\infty}(1/N!)\langle(\mathbf{Q}\mathbf{u}_\alpha)^N\rangle \equiv \exp\sum_{N=1}^{\infty}(1/N!)\langle(\mathbf{Q}\mathbf{u}_\alpha)^N\rangle_{\rm cum}. \tag{1.9.2.3}$$

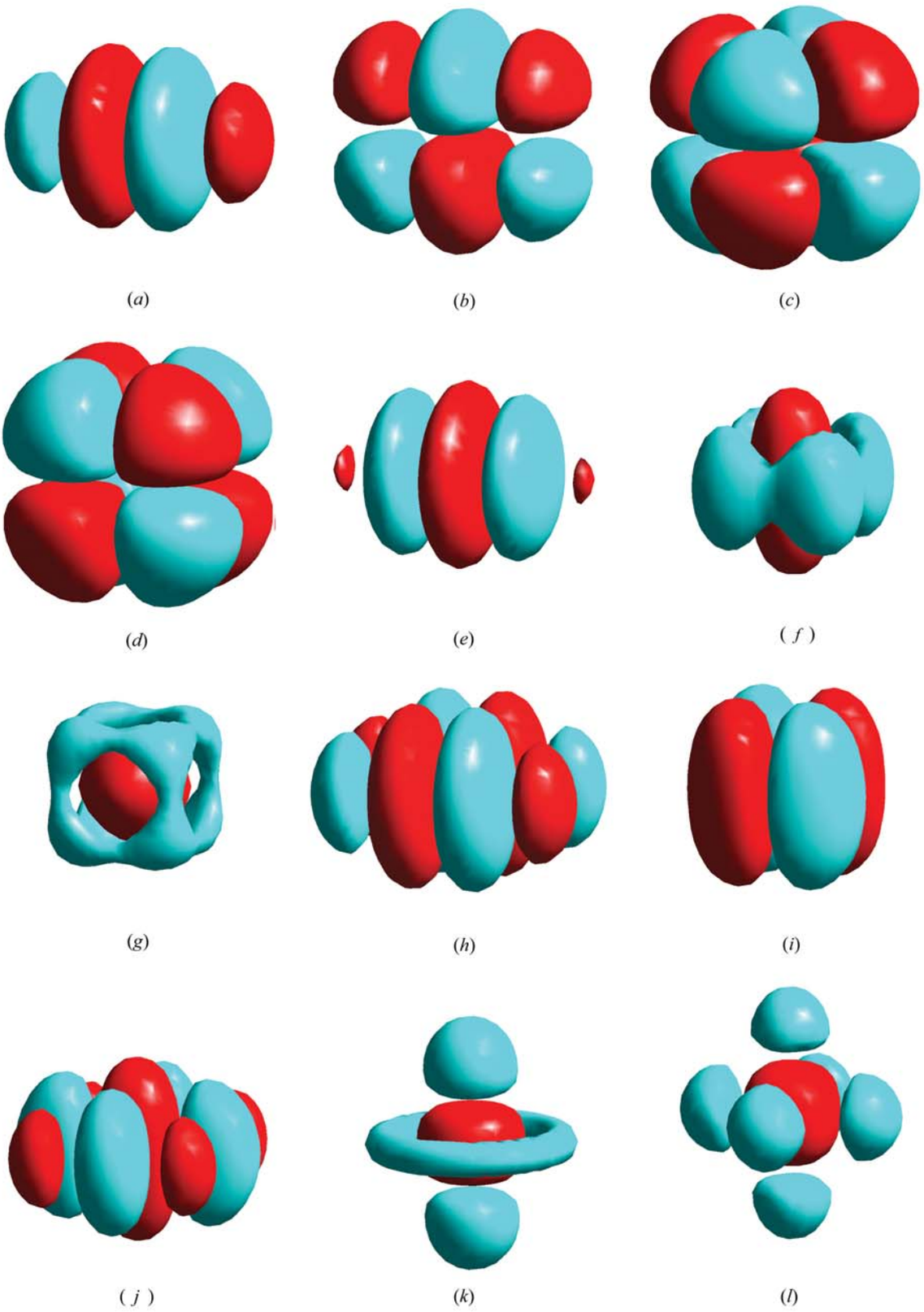

Fig. 1.9.4.1. A selection of graphical representations of density modulations due to higher-order terms in the Gram–Charlier series expansion of a Gaussian atomic probability density function. All figures are drawn on a common scale and have a common orientation. All terms within any given order of expansion are numerically identical and refer to the same underlying isotropic second-order term; the higher-order terms of different order of expansion differ by one order of magnitude, but refer again to the same underlying isotropic second-order term. The orthonormal crystallographic axes are oriented as follows: **x** oblique out of the plane of the paper towards the observer, **y** in the plane of the paper and to the right, and **z** in the plane of the paper and upwards. All surfaces are scaled to 1% of the absolute value of the maximum modulation within each density distribution. Positive modulations (*i.e.* an increase of density) are shown in red, negative modulations are shown in blue. The source of illumination is located approximately on the [111] axis. The following graphs are shown (with typical point groups for specific cases given in parentheses). Third-order terms: (*a*) b^{222}; (*b*) b^{223}; (*c*) $b^{113} = -b^{223}$ (point group $\bar{4}$); (*d*) b^{123} (point group $\bar{4}3m$). Fourth-order terms: (*e*) b^{2222}; (*f*) $b^{1111} = b^{2222}$; (*g*) $b^{1111} = b^{2222} = b^{3333}$ (point group $m\bar{3}m$); (*h*) b^{1222}; (*i*) $b^{1112} = b^{1222}$; (*j*) b^{1122}; (*k*) $b^{1133} = b^{2233}$; (*l*) $b^{1122} = b^{1133} = b^{2233}$ (point group $m\bar{3}m$).

1.10. Tensors in quasiperiodic structures

By T. Janssen

1.10.1. Quasiperiodic structures

1.10.1.1. *Introduction*

Many materials are known which show a well ordered state without lattice translation symmetry, often in a restricted temperature or composition range. This can be seen in the diffraction pattern from the appearance of sharp spots that cannot be labelled in the usual way with three integer indices. The widths of the peaks are comparable with those of perfect lattice periodic crystals, and this is a sign that the coherence length is comparable as well.

A typical example is K_2SeO_4, which has a normal lattice periodic structure above 128 K with space group *Pcmn*, but below this temperature shows satellites at positions $\gamma\mathbf{c}^*$, where γ is an irrational number, which in addition depends on temperature. These satellites cannot be labelled with integer indices with respect to the reciprocal basis $\mathbf{a}^*$, $\mathbf{b}^*$, $\mathbf{c}^*$ of the structure above the transition temperature. Therefore, the corresponding structure cannot be lattice periodic.

The diffraction pattern of K_2SeO_4 arises because the original lattice periodic *basic structure* is deformed below 128 K. The atoms are displaced from their positions in the basic structure such that the displacement itself is again periodic, but with a period that is *incommensurate* with respect to the lattice of the basic structure.

Such a *modulated structure* is just a special case of a more general type of structure. These structures are characterized by the fact that the diffraction pattern has sharp Bragg peaks at positions $\mathbf{H}$ that are linear combinations of a finite number of basic vectors:

$$\mathbf{H} = \sum_{i=1}^{n} h_i \mathbf{a}_i^* \quad (\text{integer } h_i). \tag{1.10.1.1}$$

Structures that have this property are called *quasiperiodic*. The minimal number n of basis vectors such that all h_i are integers is called the *rank* of the structure. If the rank is three and the vectors $\mathbf{a}_i$ do not all fall on a line or in a plane, the structure is just lattice periodic. Lattice periodic structures form special cases of quasiperiodic structures. The collection of vectors $\mathbf{H}$ forms the *Fourier module* of the structure. For rank three, this is just the *reciprocal lattice* of the lattice periodic structure.

The definition given above results in some important practical difficulties. In the first place, it is not possible to show experimentally that a wavevector has irrational components instead of rational ones, because an irrational number can be approximated by a rational number arbitrarily well. Very often the wavevector of the satellite changes with temperature. It has been reported that in some compounds the variation shows plateaux, but even when the change seems to be continuous and smooth one can not be sure about the irrationality. On the other hand, if the wavevector jumps from one rational position to another, the structure would always be lattice periodic, but the unit cell of this structure would vary wildly with temperature. This means that, if one wishes to describe the incommensurate phases in a unified fashion, it is more convenient to treat the wavevector as generically irrational. This experimental situation is by no means dramatic. It is similar to the way in which one can never be sure that the angles between the basis vectors of an orthorhombic lattice are really 90°, although this is a concept that no-one has problems understanding.

A second problem stems from the fact that the probt9-11(b27(theb743[(of)

$$\mathbf{e}(\mathbf{q},j)=\begin{pmatrix}\mathbf{e}_1(\mathbf{q},j)\\ \vdots\\ \mathbf{e}_N(\mathbf{q},j)\end{pmatrix}=\begin{pmatrix}e_1^x(\mathbf{q},j)\\ e_1^y(\mathbf{q},j)\\ e_1^z(\mathbf{q},j)\\ \vdots\\ e_N^x(\mathbf{q},j)\\ e_N^y(\mathbf{q},j)\\ e_N^z(\mathbf{q},j)\end{pmatrix} \tag{2.1.2.18}$$

and simultaneously the 3×3 matrices $\mathbf{F}_{\kappa\kappa'}(\mathbf{q})$ to a $3N\times 3N$ matrix $\mathbf{F}(\mathbf{q})$

$$\mathbf{F}(\mathbf{q})=\begin{pmatrix}F_{11}^{xx} & F_{11}^{xy} & F_{11}^{xz} & & & & F_{1N}^{xx} & F_{1N}^{xy} & F_{1N}^{xz}\\ F_{11}^{yx} & F_{11}^{yy} & F_{11}^{yz} & & s & & F_{1N}^{yx} & F_{1N}^{yy} & F_{1N}^{yz}\\ F_{11}^{zx} & F_{11}^{zy} & F_{11}^{zz} & & & & F_{1N}^{zx} & F_{1N}^{zy} & F_{1N}^{zz}\\ & & & F_{\kappa\kappa'}^{xx} & F_{\kappa\kappa'}^{xy} & F_{\kappa\kappa'}^{xz} & & & \\ & \vdots & & F_{\kappa\kappa'}^{yx} & F_{\kappa\kappa'}^{yy} & F_{\kappa\kappa'}^{yz} & & \vdots & \\ & & & F_{\kappa\kappa'}^{zx} & F_{\kappa\kappa'}^{zy} & F_{\kappa\kappa'}^{zz} & & & \\ F_{N1}^{xx} & F_{N1}^{xy} & F_{N1}^{xz} & & & & F_{NN}^{xx} & F_{NN}^{xy} & F_{NN}^{xz}\\ F_{N1}^{yx} & F_{N1}^{yy} & F_{N1}^{yz} & & s & & F_{NN}^{yx} & F_{NN}^{yy} & F_{NN}^{yz}\\ F_{N1}^{zx} & F_{N1}^{zy} & F_{N1}^{zz} & & & & F_{NN}^{zx} & F_{NN}^{zy} & F_{NN}^{zz}\end{pmatrix}, \tag{2.1.2.19}$$

equation (2.1.2.17) can be written in matrix notation and takes the simple form

$$\omega_{\mathbf{q},j}^2\,\mathbf{e}(\mathbf{q},j)=[\mathbf{M}\,\mathbf{F}(\mathbf{q})\,\mathbf{M}]\,\mathbf{e}(\mathbf{q},j)=\mathbf{D}(\mathbf{q})\,\mathbf{e}(\mathbf{q},j), \tag{2.1.2.20}$$

where the diagonal matrix

$$\mathbf{M}=\begin{pmatrix}\frac{1}{\sqrt{m_1}} & 0 & 0 & & & & & & \\ 0 & \frac{1}{\sqrt{m_1}} & 0 & s & & & & & \\ 0 & 0 & \frac{1}{\sqrt{m_1}} & & & & & & \\ & \vdots & & & & & \vdots & & \\ & & & & \frac{1}{\sqrt{m_N}} & 0 & 0 & & \\ & & & s & 0 & \frac{1}{\sqrt{m_N}} & 0 & & \\ & & & & 0 & 0 & \frac{1}{\sqrt{m_N}} & & \end{pmatrix} \tag{2.1.2.21}$$

contains the masses of all atoms. The $3N\times 3N$ matrix

$$\mathbf{D}(\mathbf{q})=\mathbf{M}\,\mathbf{F}(\mathbf{q})\,\mathbf{M} \tag{2.1.2.22}$$

is called the *dynamical matrix*. It contains all the information about the dynamical behaviour of the crystal and can be calculated on the basis of specific models for interatomic interactions. In analogy to the 3×3 matrices $\mathbf{F}_{\kappa\kappa'}(\mathbf{q})$, we introduce the submatrices of the dynamical matrix:

$$\mathbf{D}_{\kappa\kappa'}(\mathbf{q})=\frac{1}{\sqrt{m_\kappa m_{\kappa'}}}\,\mathbf{F}_{\kappa\kappa'}(\mathbf{q}). \tag{2.1.2.22a}$$

Owing to the symmetry of the force-constant matrix,

$$V_{\alpha\beta}(\kappa l,\kappa' l')=V_{\beta\alpha}(\kappa' l',\kappa l), \tag{2.1.2.23}$$

the dynamical matrix is Hermitian:[1]

$$\mathbf{D}^T(\mathbf{q})=\mathbf{D}^*(\mathbf{q})=\mathbf{D}(-\mathbf{q}) \tag{2.1.2.24}$$

or more specifically

$$D_{\kappa\kappa'}^{\alpha\beta}(\mathbf{q})=D_{\kappa'\kappa}^{\beta\alpha^*}(\mathbf{q})=D_{\kappa'\kappa}^{\beta\alpha}(-\mathbf{q}). \tag{2.1.2.24a}$$

Obviously, the squares of the vibrational frequency $\omega_{\mathbf{q},j}$ and the polarization vectors $\mathbf{e}(\mathbf{q},j)$ are eigenvalues and corresponding eigenvectors of the dynamical matrix. As a direct consequence of equation (2.1.2.20), the eigenvalues $\omega_{\mathbf{q},j}^2$ are real quantities and the following relations hold:

$$\omega_{\mathbf{q},j}^2=\omega_{-\mathbf{q},j}^2, \tag{2.1.2.25}$$

$$\mathbf{e}^*(\mathbf{q},j)=\mathbf{e}(-\mathbf{q},j). \tag{2.1.2.26}$$

Moreover, the eigenvectors are mutually orthogonal and can be chosen to be normalized.

[1] The superscripts ^{T} and * are used to denote the transposed and the complex conjugate matrix, respectively.

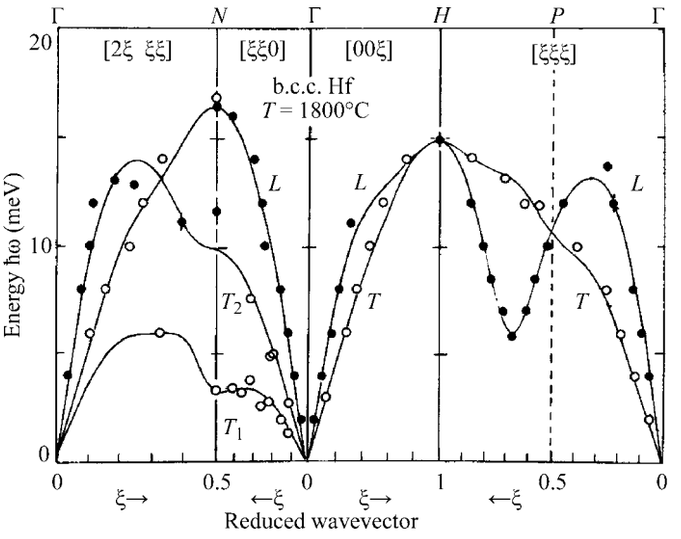

Fig. 2.1.2.3. Phonon dispersion of b.c.c. hafnium for wavevectors along the main symmetry directions of the cubic structure. The symbols represent experimental data obtained by inelastic neutron scattering and the full lines are the results of the model. From Trampenau *et al.* (1991). Copyright (1991) by the American Physical Society.

2.1.2.4. *Eigenvalues and phonon dispersion, acoustic modes*

The wavevector dependence of the vibrational frequencies is called *phonon dispersion*. For each wavevector $\mathbf{q}$ there are $3N$ fundamental frequencies yielding $3N$ phonon *branches* when $\omega_{\mathbf{q},j}$ is plotted *versus* $\mathbf{q}$. In most cases, the phonon dispersion is displayed for wavevectors along high-symmetry directions. These dispersion curves are, however, only special projections of the dispersion hypersurface in the four-dimensional $\mathbf{q}$–ω space. As a simple example, the phonon dispersion of b.c.c. hafnium is displayed in Fig. 2.1.2.3. The wavevectors are restricted to the first Brillouin zone (see Section 2.1.3.1) and the phonon dispersion for different directions of the wavevector are combined in one single diagram making use of the fact that different high-symmetry directions meet at the Brillouin-zone boundary. Note that in Fig. 2.1.2.3, the moduli of the wavevectors are scaled by the Brillouin-zone boundary values and represented by the reduced coordinates ξ. Owing to the simple b.c.c. structure of hafnium with one atom per primitive cell, there are only three phonon branches. Moreover, for all wavevectors along the directions [00ξ] and [$\xi\xi\xi$], two exhibit the same frequencies – they are said to be *degenerate*. Hence in the corresponding parts of Fig. 2.1.2.3 only two branches can be distinguished.

Whereas in this simple example the different branches can be separated quite easily, this is no longer true for more complicated crystal structures. For illustration, the phonon dispersion of the high-T_c superconductor Nd_2CuO_4 is shown in Fig. 2.1.2.4 for the main symmetry directions of the tetragonal structure (space group $I4/mmm$, seven atoms per primitive cell). Note that in many publications on lattice dynamics the frequency $\nu=\omega/2\pi$ is used rather than the angular frequency ω.

The 21 phonon branches of Nd_2CuO_4 with their more complicated dispersion reflect the details of the interatomic interactions between all atoms of the structure. The phonon frequencies ν cover a range from 0 to 18 THz. In crystals with

2.2.5. The free-electron (Sommerfeld) model

The free-electron model corresponds to the special case of taking a constant potential in the Schrödinger equation (2.2.4.1). The physical picture relies on the assumption that the (metallic) valence electrons can move freely in the field of the positively charged nuclei and the tightly bound core electrons. Each valence electron moves in a potential which is nearly constant due to the screening of the remaining valence electrons. This situation can be idealized by assuming the potential to be constant [$V(\mathbf{r}) = 0$]. This simple picture represents a crude model for simple metals but has its importance mainly because the corresponding equation can be solved analytically. By rewriting equation (2.2.4.1), we have

$$\nabla^2\psi_{\mathbf{k}}(\mathbf{r}) = -\frac{2mE}{\hbar^2}\psi_{\mathbf{k}}(\mathbf{r}) = -|\mathbf{k}|^2\psi_{\mathbf{k}}(\mathbf{r}), \tag{2.2.5.1}$$

where in the last step the constants are abbreviated (for later convenience) by $|\mathbf{k}|^2$. The solutions of this equation are plane waves (PWs)

$$\psi_{\mathbf{k}}(\mathbf{r}) = C\exp(i\mathbf{k}\cdot\mathbf{r}), \tag{2.2.5.2}$$

where C is a normalization constant which is defined from the integral over one unit cell with volume Ω. The PWs satisfy the Bloch condition and can be written (using the bra–ket notation) as

$$|\mathbf{k}\rangle = \psi_{\mathbf{k}}(\mathbf{r}) = \Omega^{1/2}\exp(i\mathbf{k}\cdot\mathbf{r}). \tag{2.2.5.3}$$

From (2.2.5.1) we see that the corresponding energy (labelled by $\mathbf{k}$) is given by

$$E_{\mathbf{k}} = \frac{\hbar^2}{2m}|\mathbf{k}|^2. \tag{2.2.5.4}$$

In this context it is useful to consider the momentum of the electron, which classically is the vector $\mathbf{p} = m\mathbf{v}$, where m and $\mathbf{v}$ are the mass and velocity, respectively. In quantum mechanics we must replace $\mathbf{p}$ by the corresponding operator $\mathbb{P}$.

$$\mathbb{P}|\mathbf{k}\rangle = \frac{\hbar}{i}\frac{\partial}{\partial\mathbf{r}}|\mathbf{k}\rangle = \frac{\hbar}{i}i\mathbf{k}|\mathbf{k}\rangle = \hbar\mathbf{k}|\mathbf{k}\rangle. \tag{2.2.5.5}$$

Thus a PW is an eigenfunction of the momentum operator with eigenvalue $\hbar\mathbf{k}$. Therefore the $\mathbf{k}$ vector is also called the *momentum* vector. Note that this is strictly true for a vanishing potential but is otherwise only approximately true (referred to as *pseudomomentum*).

Another feature of a PW is that its phase is constant in a plane perpendicular to the vector $\mathbf{k}$ (see Fig. 2.2.5.1). For this purpose, consider a periodic function in space and time,

$$\varphi_{\mathbf{k}}(\mathbf{r}, t) = \exp[i(\mathbf{k}\cdot\mathbf{r} - \omega t)], \tag{2.2.5.6}$$

which has a constant phase factor $\exp(i\omega t)$ within such a plane. We can characterize the spatial part by $\mathbf{r}$ within this plane. Taking the nearest parallel plane (with vector $\mathbf{r}'$) for which the same phase factors occur again but at a distance λ away (with the unit vector $\mathbf{e}$ normal to the plane),

$$\mathbf{r}' = \mathbf{r} + \lambda\mathbf{e} = \mathbf{r} + \lambda\frac{\mathbf{k}}{|\mathbf{k}|}, \tag{2.2.5.7}$$

then $\mathbf{k}\cdot\mathbf{r}'$ must differ from $\mathbf{k}\cdot\mathbf{r}$ by 2π. This is easily obtained from (2.2.5.7) by multiplication with $\mathbf{k}$ leading to

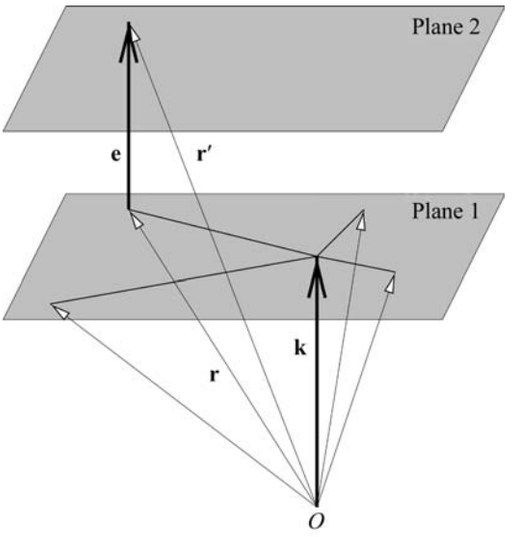

Fig. 2.2.5.1. Plane waves. The wavevector $\mathbf{k}$ and the unit vector $\mathbf{e}$ are normal to the two planes and the vectors $\mathbf{r}$ in plane 1 and $\mathbf{r}'$ in plane 2.

$$\mathbf{k}\cdot\mathbf{r}' = \mathbf{k}\cdot\mathbf{r} + \lambda\frac{|\mathbf{k}|^2}{|\mathbf{k}|} = \mathbf{k}\cdot\mathbf{r} + \lambda|\mathbf{k}| \tag{2.2.5.8}$$

$$\mathbf{k}\cdot\mathbf{r}' - \mathbf{k}\cdot\mathbf{r} = \lambda|\mathbf{k}| = 2\pi \tag{2.2.5.9}$$

$$\lambda = \frac{2\pi}{|\mathbf{k}|} \text{ or } |\mathbf{k}| = \frac{2\pi}{\lambda}. \tag{2.2.5.10}$$

Consequently λ is the wavelength and thus the $\mathbf{k}$ vector is called the *wavevector* or *propagation* vector.

2.2.6. Space-group symmetry

2.2.6.1. *Representations and bases of the space group*

The effect of a space-group operation $\{p|\mathbf{w}\}$ on a Bloch function, labelled by $\mathbf{k}$, is to transform it into a Bloch function that corresponds to a vector $p\mathbf{k}$,

$$\{p|\mathbf{w}\}\psi_{\mathbf{k}} = \psi_{p\mathbf{k}}, \tag{2.2.6.1}$$

which can be proven by using the multiplication rule of Seitz operators (2.2.3.12) and the definition of a Bloch state (2.2.4.17).

A special case is the inversion operator, which leads to

$$\{i|\mathbf{E}\}\psi_{\mathbf{k}} = \psi_{-\mathbf{k}}. \tag{2.2.6.2}$$

The Bloch functions $\psi_{\mathbf{k}}$ and $\psi_{p\mathbf{k}}$, where p is any operation of the point group P, belong to the same basis for a representation of the space group G.

$$\langle\psi_{\mathbf{k}}| = \langle\psi_{p\mathbf{k}}| \text{ for all } p \in P \text{ for all } p\mathbf{k} \in \text{BZ}. \tag{2.2.6.3}$$

The same $p\mathbf{k}$ cannot appear in two different bases, thus the two bases $\psi_{\mathbf{k}}$ and $\psi_{\mathbf{k}'}$ are either identical or have no $\mathbf{k}$ in common.

Irreducible representations of T are labelled by the N distinct $\mathbf{k}$ vectors in the BZ, which separate in disjoint bases of G (with no $\mathbf{k}$ vector in common). If a $\mathbf{k}$ vector falls on the BZ edge, application of the point-group operation p can lead to an equivalent $\mathbf{k}'$ vector that differs from the original by $\mathbf{K}$ (a vector *of* the reciprocal lattice). The set of all mutually inequivalent $\mathbf{k}$ vectors of $p\mathbf{k}$ ($p \in P$) define the *star of the* $\mathbf{k}$ *vector* ($S_{\mathbf{k}}$) (see also Section 1.2.3.3 of the present volume).

The set of all operations that leave a $\mathbf{k}$ vector invariant (or transform it into an equivalent $\mathbf{k} + \mathbf{K}$) forms the *group* $G_{\mathbf{k}}$ of the $\mathbf{k}$ vector. Application of q, an element of $G_{\mathbf{k}}$, to a Bloch function (Section 2.2.8) gives

$$q\psi^j_{\mathbf{k}}(\mathbf{r}) = \psi^{j'}_{\mathbf{k}}(\mathbf{r}) \text{ for } q \in G_{\mathbf{k}}, \tag{2.2.6.4}$$

Table 2.2.13.1. *Picking rules for the local coordinate axes and the corresponding LM combinations (ℓmp) of non-cubic groups taken from Kurki-Suonio (1977)*

Symmetry	Coordinate axes	ℓ, m, p of $y_{\ell mp}$	Crystal system
$\underline{1}$	Any	All $(\ell, m, \pm)$	Triclinic
$\overline{1}$	Any	$(2\ell, m, \pm)$	
2	$2 \parallel z$	$(\ell, 2m, \pm)$	Monoclinic
m	$m \perp z$	$(\ell, \ell - 2m, \pm)$	
$2/m$	$2 \parallel z, m \perp z$	$(2\ell, 2m, \pm)$	
222	$2 \parallel z, 2 \parallel y$ $(2 \parallel x)$	$(2\ell, 2m, +), (2\ell + 1, 2m, -)$	Orthorhombic
$mm2$	$2 \parallel z, m \perp y$ $(2 \perp x)$	$(\ell, 2m, +)$	
mmm	$2 \perp z, m \perp y, 2 \perp x$	$(2\ell, 2m, +)$	
4	$4 \parallel z$	$(\ell, 4m, \pm)$	Tetragonal
$\overline{4}$	$-4 \parallel z$	$(2\ell, 4m, \pm), (2\ell + 1, 4m + 2, \pm)$	
$4/m$	$4 \parallel z, m \perp z$	$(2\ell, 4m, \pm)$	
422	$4 \parallel z, 2 \parallel y$ $(2 \parallel x)$	$(2\ell, 4m, +), (2\ell + 1, 4m, -)$	
$4mm$	$4 \parallel z, m \perp y$ $(2 \perp x)$	$(\ell, 4m, +)$	
$\overline{4}2m$	$-4 \parallel z, 2 \parallel x$ $(m = xy \rightarrow yx)$	$(2\ell, 4m, +), (2\ell + 1, 4m + 2, -)$	
$4mmm$	$4 \parallel z, m \perp z, m \perp x$	$(2\ell, 4m, +)$	
3	$3 \parallel z$	$(\ell, 3m, \pm)$	Rhombohedral
$\overline{3}$	$-3 \parallel z$	$(2\ell, 3m, \pm)$	
32	$3 \parallel z, 2 \parallel y$	$(2\ell, 3m, +), (2\ell + 1, 3m, -)$	
$3m$	$3 \parallel z, m \perp y$	$(\ell, 3m, +)$	
$\overline{3}m$	$-3 \parallel z, m \perp y$	$(2\ell, 3m, +)$	
6	$6 \parallel z$	$(\ell, 6m, \pm)$	Hexagonal
$\overline{6}$	$-6 \parallel z$	$(2\ell, 6m, +), (2\ell + 1, 6m + 3, \pm)$	
$6/m$	$6 \parallel z, m \perp z$	$(2\ell, 6m, \pm)$	
622	$6 \parallel z, 2 \parallel y$ $(2 \parallel x)$	$(2\ell, 6m, +), (2\ell + 1, 6m, -)$	
$6mm$	$6 \parallel z, m \parallel y$ $(m \perp x)$	$(\ell, 6m, +)$	
$\overline{6}2m$	$-6 \parallel z, m \perp y$ $(2 \parallel x)$	$(2\ell, 6m, +), (2l + 1, 6m + 3, +)$	
$6mmm$	$6 \parallel z, m \perp z, m \perp y$ $(m \perp x)$	$(2\ell, 6m, +)$	

Therefore in the MTA one must make a compromise, whereas in full-potential calculations this problem practically disappears.

2.2.13. The local coordinate system

The partition of a crystal into atoms (or molecules) is ambiguous and thus the atomic contribution cannot be defined uniquely. However, whatever the definition, it must follow the relevant site symmetry for each atom. There are at least two reasons why one would want to use a *local coordinate system* at each atomic site: the concept of crystal harmonics and the interpretation of bonding features.

2.2.13.1. *Crystal harmonics*

All spatial observables of the bound atom (*e.g.* the potential or the charge density) must have the crystal symmetry, *i.e.* the point-group symmetry around an atom. Therefore they must be representable as an expansion in terms of site-symmetrized spherical harmonics. Any point-symmetry operation transforms a spherical harmonic into another of the same ℓ. We start with the usual complex spherical harmonics,

$$Y_{\ell m}(\vartheta, \varphi) = N_{\ell m} P_\ell^m(\cos\vartheta) \exp(im\varphi), \qquad (2.2.13.1)$$

which satisfy Laplacian's differential equation. The $P_\ell^m(\cos\vartheta)$ are the associated Legendre polynomials and the normalization $N_{\ell m}$ is according to the convention of Condon & Shortley (1953). For the φ-dependent part one can use the real and imaginary part and thus use $\cos(m\varphi)$ and $\sin(m\varphi)$ instead of the $\exp(im\varphi)$ functions,

Table 2.2.13.2. *LM combinations of cubic groups as linear cominations of $y_{\ell mp}$'s (given in parentheses)*

The linear-combination coefficients can be found in Kurki-Suonio (1977).

Symmetry	*LM* combinations
23	(0 0), (3 2−), (4 0, 4 4+), (6 0, 6 4+), (6 2+, 6 6+)
$m3$	(0 0), (4 0, 4 4+), (6 0, 6 4+) (6 2+, 6 6+)
432	(0 0), (4 0, 4 4+), (6 0, 6 4+)
$\overline{4}3m$	(0 0), (3 2−), (4 0, 4 4+), (6 0, 6 4+),
$m3m$	(0 0), (4 0, 4 4+), (6 0, 6 4+)

but we must introduce a parity p to distinguish the functions with the same $|m|$. For convenience we take real spherical harmonics, since physical observables are real. The even and odd polynomials are given by the combination of the complex spherical harmonics with the parity p either + or − by

$$y_{\ell mp} = \begin{cases} y_{\ell m+} = (1/\sqrt{2})(Y_{\ell m} + Y_{\ell \bar{m}}) & + \text{ parity} \\ y_{\ell m-} = -(i/\sqrt{2})(Y_{\ell m} - Y_{\bar{m}}) & - \text{parity} \end{cases}, \; m = 2n$$

$$y_{\ell mp} = \begin{cases} y_{\ell m+} = -(1/\sqrt{2})(Y_{\ell m} - Y_{\ell \bar{m}}) & + \text{ parity} \\ y_{\ell m-} = (i/\sqrt{2})(Y_{\ell m} + Y_{\ell \bar{m}}) & - \text{parity} \end{cases}, \; m = 2n + 1. \qquad (2.2.13.2)$$

The expansion of – for example – the charge density $\rho(\mathbf{r})$ around an atomic site can be written using the LAPW method [see the analogous equation (2.2.12.5) for the potential] in the form

$$\rho(\mathbf{r}) = \sum_{LM} \rho_{LM}(r) K_{LM}(\hat{\mathbf{r}}) \text{ inside an atomic sphere}, \qquad (2.2.13.3)$$

where we use capital letters LM for the indices (i) to distinguish this expansion from that of the wavefunctions in which complex spherical harmonics are used [see (2.2.12.1)] and (ii) to include the parity p in the index M (which represents the combined index mp). With these conventions, K_{LM} can be written as a linear combination of real spherical harmonics $y_{\ell mp}$ which are symmetry-adapted to the site symmetry,

$$K_{LM}(\hat{\mathbf{r}}) = \begin{cases} y_{\ell mp} & \text{non-cubic} \\ \sum_j c_{Lj} y_{\ell jp} & \text{cubic} \end{cases} \qquad (2.2.13.4)$$

i.e. they are either $y_{\ell mp}$ [(2.2.13.2)] in the non-cubic cases (Table 2.2.13.1) or are well defined combinations of $y_{\ell mp}$'s in the five cubic cases (Table 2.2.13.2), where the coefficients c_{Lj} depend on the normalization of the spherical harmonics and can be found in Kurki-Suonio (1977).

According to Kurki-Suonio, the number of (non-vanishing) LM terms [*e.g.* in (2.2.13.3)] is minimized by choosing for each atom a local Cartesian coordinate system adapted to its site

2.3. Raman scattering

By I. Gregora

2.3.1. Introduction

The term Raman scattering, traditionally used for light scattering by molecular vibrations or optical lattice vibrations in crystals, is often applied in a general sense to a vast variety of phenomena of inelastic scattering of photons by various excitations in molecules, solids or liquids. In crystals these excitations may be collective (phonons, plasmons, polaritons, magnons) or single-particle (electrons, electron–hole pairs, vibrational and electronic excitation of impurities). Raman scattering provides an important tool for the study of the properties of these excitations. In the present chapter, we shall briefly review the general features of Raman scattering in perfect crystals on a phenomenological basis, paying special attention to the consequences of the crystal symmetry. Our focus will be mainly on Raman scattering by vibrational excitations of the crystal lattice – *phonons*. Nevertheless, most of the conclusions have general validity and may be (with possible minor modifications) transferred also to inelastic scattering by other excitations.

2.3.2. Inelastic light scattering in crystals – basic notions

Although quantum concepts must be used in any complete theory of inelastic scattering, basic insight into the problem may be obtained from a semiclassical treatment. In classical terms, the origin of inelastically scattered light in solids should be seen in the modulation of the dielectric susceptibility of a solid by elementary excitations. The exciting light polarizes the solid and the polarization induced *via* the modulated part of the susceptibility is re-radiated at differently shifted frequencies. Thus inelastic scattering of light by the temporal and spatial fluctuations of the dielectric susceptibility that are induced by elementary excitations provides information about the symmetry and wavevector-dependent frequencies of the excitations themselves as well as about their interaction with electromagnetic waves.

2.3.2.1. *Kinematics*

Let us consider the incident electromagnetic radiation, the scattered electromagnetic radiation and the elementary excitation to be described by plane waves. The incident radiation is characterized by frequency ω_I, wavevector $\mathbf{k}_I$ and polarization vector $\mathbf{e}_I$. Likewise, the scattered radiation is characterized by ω_S, $\mathbf{k}_S$ and $\mathbf{e}_S$:

$$\mathbf{E}_{I,S}(\mathbf{r}, t) = E_{I,S}\mathbf{e}_{I,S}\exp(i\mathbf{k}_{I,S}\mathbf{r} - \omega t). \tag{2.3.2.1}$$

The scattering process involves the annihilation of the incident photon, the emission or annihilation of one or more quanta of elementary excitations and the emission of a scattered photon. The scattering is characterised by a *scattering frequency* ω (also termed the *Raman shift*) corresponding to the energy transfer $\hbar\omega$ from the radiation field to the crystal, and by a *scattering wavevector* $\mathbf{q}$ corresponding to the respective momentum transfer $\hbar\mathbf{q}$. Since the energy and momentum must be conserved in the scattering process, we have the conditions

$$\begin{aligned} \omega_I - \omega_S &= \omega, \\ \mathbf{k}_I - \mathbf{k}_S &= \mathbf{q}. \end{aligned} \tag{2.3.2.2}$$

Strictly speaking, the momentum conservation condition is valid only for sufficiently large, perfectly periodic crystals. It is further assumed that there is no significant absorption of the incident and scattered light beams, so that the wavevectors may be considered real quantities.

Since the photon wavevectors $(\mathbf{k}_I, \mathbf{k}_S)$ and frequencies (ω_I, ω_S) are related by the dispersion relation $\omega = ck/n$, where c is the speed of light in free space and n is the refractive index of the medium at the respective frequency, the energy and wavevector conservation conditions imply for the magnitude of the scattering wavevector q

$$c^2q^2 = n_I^2\omega_I^2 + n_S^2(\omega_I - \omega)^2 - 2n_In_S\omega_I(\omega_I - \omega)\cos\varphi, \tag{2.3.2.3}$$

where φ is the *scattering angle* (the angle between $\mathbf{k}_I$ and $\mathbf{k}_S$). This relation defines in the (ω, q) plane the region of wavevectors and frequencies accessible to the scattering. This relation is particularly important for scattering by excitations whose frequencies depend markedly on the scattering wavevector (*e.g.* acoustic phonons, polaritons *etc.*).

2.3.2.2. *Cross section*

In the absence of any excitations, the incident field $\mathbf{E}_I$ at frequency ω_I induces in the crystal the polarization $\mathbf{P}$, related to the field by the *linear* dielectric susceptibility tensor χ (ε_0 is the permittivity of free space):

$$\mathbf{P} = \varepsilon_0\chi(\omega_I)\mathbf{E}_I. \tag{2.3.2.4}$$

The linear susceptibility $\chi(\omega_I)$ is understood to be independent of position, depending on the crystal characteristics and on the frequency of the radiation field only. In the realm of nonlinear optics, additional terms of higher order in the fields may be considered; they are expressed through the respective *nonlinear* susceptibilities.

The effect of the excitations is to modulate the wavefunctions and the energy levels of the medium, and can be represented macroscopically as an additional contribution to the linear susceptibility. Treating this modulation as a perturbation, the resulting contribution to the susceptibility tensor, the so-called *transition susceptibility* $\delta\chi$ can be expressed as a Taylor expansion in terms of *normal coordinates* Q_j of the excitations:

$$\chi \to \chi + \delta\chi, \text{ where } \delta\chi = \sum_j \chi^{(j)}Q_j + \sum_{j,j'} \chi^{(j,j')}Q_jQ_{j'} + \ldots. \tag{2.3.2.5}$$

The tensorial coefficients $\chi^{(j)}$, $\chi^{(j,j')}$, ... in this expansion are, in a sense, *higher-order susceptibilities* and are often referred to as *Raman tensors* (of the first, second and higher orders). They are obviously related to *susceptibility derivatives* with respect to the normal coordinates of the excitations. The time-dependent polarization induced by $\delta\chi$ *via* time dependence of the normal coordinates can be regarded as the source of the inelastically scattered radiation.

The central quantity in the description of Raman scattering is the *spectral differential cross section*, defined as the relative rate of energy loss from the incident beam (frequency ω_I, polarization $\mathbf{e}_I$) as a result of its scattering (frequency ω_S, polarization $\mathbf{e}_S$) in volume V into a unit solid angle and unit frequency interval. The corresponding formula may be concisely written as (see *e.g.* Hayes & Loudon, 1978)

$$\frac{\mathrm{d}^2\sigma}{\mathrm{d}\Omega\ \mathrm{d}\omega_S} = \frac{\omega_S^3\omega_IV^2n_S}{(4\pi)^2c^4n_I}\left\langle\left|\mathbf{e}_I\delta\chi\mathbf{e}_S\right|^2\right\rangle_\omega. \tag{2.3.2.6}$$

Table 2.3.3.3. *Raman selection rules in crystals of the* 4*mm class*

Scattering configuration		Cross section for symmetry species	
		A_1	E
$\mathbf{q} \parallel \mathbf{z}$	$z(xx)z, z(yy)z$	$\sim \lvert a_{\rm LO}\rvert^2$	–
$\mathbf{q} \perp \mathbf{z}$	$x(zz)x, x(zz)y$	$\sim \lvert b_{\rm TO}\rvert^2$	–
	$\bar{y}(xz)y, \bar{x}(yz)x$	–	$\sim \lvert f_{\rm TO}\rvert^2$
	$x'(zx')y', x'(y'z)y'$	–	$\frac{1}{2}\lvert f_{\rm TO}\rvert^2 + \frac{1}{2}\lvert f_{\rm LO}\rvert^2$

Example: To illustrate the salient features of polar-mode scattering let us consider a crystal of the 4*mm* class, where of the Raman-active symmetry species the modes $A_1(z)$ and $E(x, y)$ are polar. According to Table 2.3.3.1, their ($\mathbf{q} = 0$) Raman tensors are identical to those of the A_{1g} and E_g modes in the preceding example of a 4/*mmm*-class crystal. Owing to the macroscopic electric field, however, here one has to expect directional dispersion of the frequencies of the long wavelength ($\mathbf{q} \approx 0$) A_1 and E optic phonon modes according to their longitudinal or transverse character. Consequently, in determining the polarization selection rules, account has to be taken of the direction of the phonon wavevector (*i.e.* the scattering wavevector) $\mathbf{q}$ with respect to the crystallographic axes. Since for a general direction of $\mathbf{q}$ the modes are coupled by the field, a suitable experimental arrangement permitting the efficient separation of their respective contributions should have the scattering wavevector $\mathbf{q}$ oriented along principal directions. At $\mathbf{q} \parallel \mathbf{z}$, the A_1 phonons are longitudinal ($LO_\parallel$) and both E modes ($2TO_\perp$) are transverse, remaining degenerate, whereas at $\mathbf{q} \parallel \mathbf{x}$ or $\mathbf{q} \parallel \mathbf{y}$, the A_1 phonons become transverse ($TO_\perp$) and the E phonons split into a pair of ($TO_\perp$, $LO_\perp$) modes of different frequencies. The subscripts $\parallel$ or $\perp$ explicitly indicate the orientation of the electric dipole moment carried by the mode with respect to the fourfold axis ($4 \parallel \mathbf{c} \equiv \mathbf{z}$).

Schematically, the situation (*i.e.* frequency shifts and splittings) at $\mathbf{q} \approx 0$ can be represented by

	$\mathbf{q} \parallel \mathbf{z}$	$\mathbf{q} \parallel \mathbf{x}$	
		–	$A_1(TO_\parallel)$
$A_1(LO_\parallel)$	–		
		–	$E_x(LO_\perp)$
$E(2TO_\perp)$	–	–	$E_y(TO_\perp)$

For a general direction of $\mathbf{q}$, the modes are of a mixed character and their frequencies show directional (angular) dispersion. The overall picture depends on the number of A_1 and E phonons present in the given crystal, as well as on their effective charges and on the ordering of their eigenfrequencies. In fact, only the $E(TO_\perp)$ modes remain unaffected by the directional dispersion.

Table 2.3.3.3 gives the corresponding contributions of these modes to the cross section for several representative scattering geometries, where subscripts TO and LO indicate that the components of the total Raman tensor may take on different values for TO and LO modes due to electro-optic contributions in the latter case.

2.3.3.6. $\mathbf{q}$-*dependent terms*

So far, we have not explicitly considered the dependence of the Raman tensor on the magnitude of the scattering wavevector, assuming $\mathbf{q} \to 0$ (the effects of directional dispersion in the case of scattering by polar modes were briefly mentioned in the preceding section). In some cases, however, the Raman tensors vanish in this limit, or $\mathbf{q}$-dependent corrections to the scattering may appear. Formally, we may expand the susceptibility in a Taylor series in $\mathbf{q}$. The coefficients in this expansion are higher-order susceptibility derivatives taken at $\mathbf{q} = 0$. The symmetry-restricted form of these tensorial coefficients may be determined in the same way as that of the zero-order term, *i.e.* by decomposing the reducible representation of the third-, fourth- and higher-order polar Cartesian tensors into irreducible components $\Gamma(j)$. General properties of the $\mathbf{q}$-dependent terms can be advantageously discussed in connection with the so-called *morphic* effects (see Sections 2.3.4 and 2.3.5).

2.3.4. Morphic effects in Raman scattering

By *morphic* effects we understand the effects that arise from a reduction of the symmetry of a system caused by the application of *external forces*. The relevant consequences of morphic effects for Raman scattering are changes in the selection rules. Applications of external forces may, for instance, render it possible to observe scattering by excitations that are otherwise inactive. Again, group-theoretical arguments may be applied to obtain the symmetry-restricted component form of the Raman tensors under applied forces.

It should be noted that under external forces in this sense various 'built-in' fields can be included, *e.g.* electric fields or elastic strains typically occurring near the crystal surfaces. Effects of 'intrinsic' macroscopic electric fields associated with long-wavelength LO polar phonons can be treated on the same footing. Spatial-dispersion effects connected with the finiteness of the wavevectors, $\mathbf{q}$ or $\mathbf{k}$, may also be included among morphic effects, since they may be regarded as being due to the gradients of the fields (displacement or electric) propagating in the crystal.

2.3.4.1. *General remarks*

Various types of applied forces – in a general sense – can be classified according to symmetry, *i.e.* according to their transformation properties. Thus a force is characterized as a *polar* force if it transforms under the symmetry operation of the crystal like a polar tensor of appropriate rank (rank 1: electric field $\mathbf{E}$; rank 2: electric field gradient $\nabla\mathbf{E}$, stress $\mathbf{T}$ or strain $\mathbf{S}$). It is an *axial* force if it transforms like an axial tensor (rank 1: magnetic field $\mathbf{H}$). Here we shall deal briefly with the most important cases within the macroscopic approach of the susceptibility derivatives. We shall treat explicitly the first-order scattering only and neglect, for the moment, $\mathbf{q}$-dependent terms.

In a perturbation approach, the first-order transition susceptibility $\delta\chi$ in the presence of an applied force $\mathbf{F}$ can be expressed in terms of Raman tensors $\mathbf{R}^j(\mathbf{F})$ expanded in powers of $\mathbf{F}$:

$$\delta\chi(\mathbf{F}) = \sum_j \mathbf{R}^j(\mathbf{F}) Q_j,$$
$$\text{where } \mathbf{R}^j(\mathbf{F}) = \mathbf{R}^{j0} + \mathbf{R}^{jF}\mathbf{F} + \tfrac{1}{2}\mathbf{R}^{jFF}\mathbf{F}\mathbf{F} + \ldots. \tag{2.3.4.1}$$

Here, $\mathbf{R}^{j0} = \chi^{(j)}(0) = (\partial\chi_{\alpha\beta}/\partial Q_j)$ is the zero-field *intrinsic* Raman tensor, whereas the tensors

$$\mathbf{R}^{jF}\mathbf{F} = \left(\frac{\partial^2\chi_{\alpha\beta}}{\partial Q_j \partial F_\mu}\right) F_\mu,$$
$$\mathbf{R}^{jFF}\mathbf{F}\mathbf{F} = \left(\frac{\partial^3\chi_{\alpha\beta}}{\partial Q_j \partial F_\mu \partial F_\nu}\right) F_\mu F_\nu \text{ etc.} \tag{2.3.4.2}$$

are the *force-induced* Raman tensors of the respective order in the field, associated with the jth normal mode. The scattering cross section for the jth mode becomes proportional to $\lvert\mathbf{e}_S(\mathbf{R}^{j0} + \mathbf{R}^{jF}\mathbf{F} + \frac{1}{2}\mathbf{R}^{jFF}\mathbf{F}\mathbf{F} + \ldots)\mathbf{e}_I\rvert^2$, which, in general, may modify the polarization selection rules. If, for example, the mode is *intrinsically* Raman inactive, *i.e.* $\mathbf{R}^{j0} = 0$ whereas $\mathbf{R}^{jF} \neq 0$, we deal with purely force-induced Raman scattering; its intensity is proportional to F^2 in the first order. Higher-order terms must be investigated if, for symmetry reasons, the first-order terms vanish.

For force-induced Raman activity, in accordance with general rules, invariance again requires that a particular symmetry species $\Gamma(j)$ can contribute to the first-order transition susceptibility by terms of order n in the force only if the identity

dissipation theorem in the classical limit for $h\delta\nu \ll k_B T$ (Hayes & Loudon, 1978). The coupling coefficient M is given by

$$M = |e_m e'_n \kappa_{mi} \kappa_{nj} p'_{ijk\ell} \hat{u}_k \hat{Q}_\ell|^2. \quad (2.4.4.8)$$

In practice, the incident intensity is defined outside the scattering volume, $I_{\rm out}$, and for normal incidence one can write

$$I_{\rm in} = \frac{4n}{(n+1)^2} I_{\rm out}. \quad (2.4.4.9a)$$

Similarly, the scattered power is observed outside as $P_{\rm out}$, and

$$P_{\rm out} = \frac{4n'}{(n'+1)^2} P_{\rm in}, \quad (2.4.4.9b)$$

again for normal incidence. Finally, the approximative relation between the scattering solid angle $\Omega_{\rm out}$, outside the sample, and the solid angle $\Omega_{\rm in}$, in the sample, is

$$\Omega_{\rm out} = (n')^2 \Omega_{\rm in}. \quad (2.4.4.9c)$$

Substituting (2.4.4.9*a*,*b*,*c*) in (2.4.4.7), one obtains (Vacher & Boyer, 1972)

$$\frac{{\rm d}P_{\rm out}}{{\rm d}\Omega_{\rm out}} = \frac{8\pi^2 k_B T}{\lambda_0^4} \frac{n^4}{(n+1)^2} \frac{(n')^4}{(n'+1)^2} \beta V I_{\rm out}, \quad (2.4.4.10)$$

where the coupling coefficient β is

$$\beta = \frac{1}{n^4 (n')^4} \frac{|e_m e'_n \kappa_{mi} \kappa_{nj} p'_{ijk\ell} \hat{u}_k \hat{Q}_\ell|^2}{C}. \quad (2.4.4.11)$$

In the cases of interest here, the tensor $\boldsymbol{\kappa}$ is diagonal, $\kappa_{ij} = n_i^2 \delta_{ij}$ without summation on i, and (2.4.4.11) can be written in the simpler form

$$\beta = \frac{1}{n^4 (n')^4} \frac{|e_i n_i^2 p'_{ijk\ell} \hat{u}_k \hat{Q}_\ell e'_j n_j^2|^2}{C}. \quad (2.4.4.12)$$

2.4.5. Use of the tables

The tables in this chapter give information on modes and scattering geometries that are in most common use in the study of hypersound in single crystals. Just as in the case of X-rays, Brillouin scattering is not sensitive to the presence or absence of a centre of symmetry (Friedel, 1913). Hence, the results are the same for all crystalline classes belonging to the same centric group, also called Laue class. The correspondence between the point groups and the Laue classes analysed here is shown in Table 2.4.5.1. The monoclinic and triclinic cases, being too cumbersome, will not be treated here.

For tensor components $c_{ijk\ell}$ and $p_{ijk\ell}$, the tables make use of the usual contracted notation for index pairs running from 1 to 6. However, as the tensor $p'_{ijk\ell}$ is not symmetric upon interchange of (k, ℓ), it is necessary to distinguish the order (k, ℓ) and (ℓ, k). This is accomplished with the following correspondence:

$$\begin{array}{lll} 1,1 \rightarrow 1 & 2,2 \rightarrow 2 & 3,3 \rightarrow 3 \\ 1,2 \rightarrow 6 & 2,3 \rightarrow 4 & 3,1 \rightarrow 5 \\ 2,1 \rightarrow \bar{6} & 3,2 \rightarrow \bar{4} & 1,3 \rightarrow \bar{5}. \end{array}$$

Geometries for longitudinal modes (LA) are listed in Tables 2.4.5.2 to 2.4.5.8. The first column gives the direction of the scattering vector $\hat{\mathbf{Q}}$ that is parallel to the displacement $\hat{\mathbf{u}}$. The second column gives the elastic coefficient according to (2.4.2.6). In piezoelectric materials, effective elastic coefficients defined in (2.4.2.11) must be used in this column. The third column gives the direction of the light polarizations $\hat{\mathbf{e}}$ and $\hat{\mathbf{e}}'$, and the last column gives the corresponding coupling coefficient β [equation (2.5.5.11)]. In general, the strongest scattering intensity is obtained for polarized scattering ($\hat{\mathbf{e}} = \hat{\mathbf{e}}'$), which is the only situation listed in the tables. In this case, the coupling to light (β) is independent of the scattering angle θ, and thus the tables apply to any θ value.

Tables 2.4.5.9 to 2.4.5.15 list the geometries usually used for the observation of TA modes in backscattering ($\theta = 180^\circ$). In this case, $\hat{\mathbf{u}}$ is always perpendicular to $\hat{\mathbf{Q}}$ (pure transverse modes), and $\hat{\mathbf{e}}'$ is not necessarily parallel to $\hat{\mathbf{e}}$. Cases where pure TA modes with $\hat{\mathbf{u}}$ in the plane perpendicular to $\hat{\mathbf{Q}}$ are degenerate are indicated by the symbol D in the column for $\hat{\mathbf{u}}$. For the Pockels tensor components, the notation is $p_{\alpha\beta}$ if the rotational term vanishes by symmetry, and it is $p'_{\alpha\beta}$ otherwise.

Tables 2.4.5.16 to 2.4.5.22 list the common geometries used for the observation of TA modes in 90° scattering. In these tables, the polarization vector $\hat{\mathbf{e}}$ is always perpendicular to the scattering plane and $\hat{\mathbf{e}}'$ is always parallel to the incident wavevector of light $\mathbf{q}$. Owing to birefringence, the scattering vector $\hat{\mathbf{Q}}$ does not exactly bisect $\mathbf{q}$ and $\mathbf{q}'$ [equation (2.4.4.4)]. The tables are written for strict 90° scattering, $\mathbf{q} \cdot \mathbf{q}' = 0$, and in the case of birefringence the values of $\mathbf{q}^{(m)}$ to be used are listed separately in Table 2.4.5.23. The latter assumes that the birefringences are not large, so that the values of $\mathbf{q}^{(m)}$ are given only to first order in the birefringence.

2.4.6. Techniques of Brillouin spectroscopy

Brillouin spectroscopy with visible laser light requires observing frequency shifts falling typically in the range ~1 to ~100 GHz, or ~0.03 to ~3 cm^{-1}. To achieve this with good resolution one mostly employs interferometry. For experiments at very small angles (near forward scattering), photocorrelation spectroscopy can also be used. If the observed frequency shifts are ≥ 1 cm^{-1}, rough measurements of spectra can sometimes be obtained with modern grating instruments. Recently, it has also become possible to perform Brillouin scattering using other excitations, in particular neutrons or X-rays. In these cases, the coupling does not occur *via* the Pockels effect, and the frequency shifts that are observed are much larger. The following discussion is restricted to optical interferometry.

The most common interferometer that has been used for this purpose is the single-pass planar Fabry–Perot (Born & Wolf, 1993). Upon illumination with monochromatic light, the frequency response of this instrument is given by the Airy function, which consists of a regular comb of maxima obtained as the optical path separating the mirrors is increased. Successive maxima are separated by $\lambda/2$. The ratio of the maxima separation to the width of a single peak is called the finesse F, which increases as the mirror reflectivity increases. The finesse is also limited by the planarity of the mirrors. A practical limit is $F \sim 100$. The resolving power of such an instrument is $R = 2\ell/\lambda$, where ℓ is the optical thickness. Values of R around 10^6 to 10^7 can be achieved. It is impractical to increase ℓ above ~5 cm because the luminosity of the instrument is proportional to $1/\ell$. If higher

Table 2.4.5.1. *Definition of Laue classes*

Crystal system	Laue class	Point groups
Cubic	C_1	432, $\bar{4}3m$, $m\bar{3}m$
	C_2	23, $\bar{3}m$
Hexagonal	H_1	622, $6mm$, $\bar{6}2m$, $6/mm$
	H_2	6, $\bar{6}$, $6/m$
Tetragonal	T_1	422, $4mm$, $\bar{4}2m$, $4/mm$
	T_2	4, $\bar{4}$, $4/m$
Trigonal	R_1	32, $3m$, $\bar{3}m$
	R_2	3, $\bar{3}$
Orthorhombic	O	mmm, $2mm$, 222

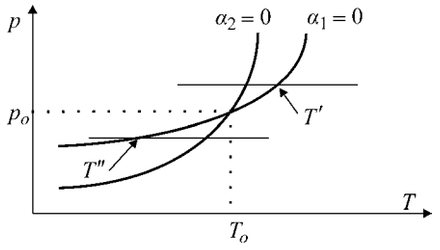

Fig. 3.1.2.3. Plots representative of the equations $\alpha_1(p, T) = 0$ and $\alpha_2(p, T) = 0$. The simultaneous vanishing of these coefficients occurs for a single couple of temperature and pressure (p_0,T_0).

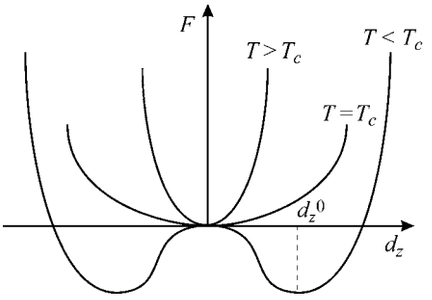

Fig. 3.1.2.4. Plots of the Landau free energy as a function of the order parameter, for values of the temperature above or below T_c or coincident with T_c. The shape of the plot changes qualitatively from a one-minimum plot to a two-minimum plot.

(T_0, p_0). Let us consider, for instance, the situation depicted in Fig. 3.1.2.3. For $p > p_0$, on lowering the temperature, α_1 vanishes at T' and α_2 remains positive in the neighbourhood of T'. Hence, the equilibrium value of the set (d_x, d_y) remains equal to zero on either side of T'. A transition at this temperature will only concern a possible change in d_z^0.

Likewise for p below p_0, a transition at T'' will only concern a possible change of the set of components (d_x^0, d_y^0), the third component d_z remaining equal to zero on either sides of T''. Hence an infinitesimal change of the pressure (for instance a small fluctuation of the atmospheric pressure) from above p_0 to below p_0 will *modify qualitatively the nature of the phase transformation* with the direction of the displacement changing abruptly from z to the (x, y) plane. As will be seen below, the crystalline symmetries of the phases stable below T' and T'' are different. This is a singular situation, of *instability*, of the type of phase transition, not encountered in real systems. Rather, the standard situation corresponds to pressures away from p_0, for which a slight change of the pressure does not modify significantly the direction of the displacement. In this case, one coefficient α_i only vanishes and changes sign at the transition temperature, as stated above.

3.1.2.2.5. *Stable state below T_c and physical anomalies induced by the transition*

We have seen that either d_z or the couple (d_x, d_y) of components of the displacement constitute the order parameter of the transition and that the free energy needs only to be expanded as a function of the components of the order parameter. Below the transition, the corresponding coefficient α_i is negative and, accordingly, the free energy, limited to its second-degree terms, has a maximum for $\mathbf{d} = 0$ and no minimum. Such a truncated expansion is not sufficient to determine the equilibrium state of the system. The stable state of the system must be determined by positive terms of higher degrees. Let us examine first the simplest case, for which the order parameter coincides with the d_z component.

The same symmetry argument used to establish the form (3.1.2.1) of the Landau free energy allows one straightforwardly to assert the absence of a third-degree term in the expansion of F as a function of the order parameter d_z, and to check the effective occurrence of a fourth-degree term. If we assume that this simplest form of expansion is sufficient to determine the equilibrium state of the system, the coefficient of the fourth-degree term must be positive in the neighbourhood of T_c. Up to the latter degree, the form of the relevant contributions to the free energy is therefore

$$F = F_o(T, p) + \frac{\alpha(T - T_c)}{2} d_z^2 + \frac{\beta}{4} d_z^4. \qquad (3.1.2.2)$$

In this expression, α_1, which is an odd function of $(T - T_c)$ since it vanishes and changes sign at T_c, has been expanded linearly. Likewise, the lowest-degree expansion of the function $\beta(T - T_c)$ is a *positive constant* in the vicinity of T_c. The function F_0, which is the zeroth-degree term in the expansion, represents the normal 'background' part of the free energy. It behaves smoothly since it does not depend on the order parameter. A plot of $[F(d_z) - F_0]$ for three characteristic temperatures is shown in Fig. 3.1.2.4.

The minima of F, determined by the set of conditions

$$\frac{\partial F}{\partial d_z} = 0; \quad \frac{\partial^2 F}{\partial^2 d_z} > 0, \qquad (3.1.2.3)$$

occur above T_c for $d_z = 0$, as expected. For $T < T_c$ they occur for

$$d_z^0 = \pm\sqrt{\alpha \frac{(T_c - T)}{\beta}}. \qquad (3.1.2.4)$$

This behaviour has a general validity: the order parameter of a transition is expected, in the framework of Landau's theory, to possess a square-root dependence as a function of the deviation of the temperature from T_c.

Note that one finds two minima corresponding to the same value of the free energy and opposite values of d_z^0. The corresponding upward and downward displacements of the M^+ ion (Fig. 3.1.2.1) are distinct states of the system possessing the same stability.

Other physical consequences of the form (3.1.2.2) of the free energy can be drawn: absence of latent heat associated with the crossing of the transition, anomalous behaviour of the specific heat, anomalous behaviour of the *dielectric susceptibility* related to the order parameter.

The *latent heat* is $L = T\Delta S$, where ΔS is the difference in entropy between the two phases at T_c. We can derive S in each phase from the equilibrium free energy $F(T, p, d_z^0(T, p))$ using the expression

$$S = -\frac{\mathrm{d}F}{\mathrm{d}T}\bigg|d_z^0 = -\left[\frac{\partial F}{\partial T}\bigg|d_z^0 + \frac{\partial F}{\partial d_z}\frac{\mathrm{d}(d_z)}{\mathrm{d}T}\bigg|d_z^0\right]. \qquad (3.1.2.5)$$

However, since F is a minimum for $d_z = d_z^0$, the second contribution vanishes. Hence

$$S = -\frac{\alpha}{2}\left(d_z^0\right)^2 - \frac{\partial F_0}{\partial T}. \qquad (3.1.2.6)$$

Since both d_z^0 and $(\partial F_0/\partial T)$ are continuous at T_c, there is no entropy jump $\Delta S = 0$, and *no latent heat at the transition*.

Several values of the specific heat can be considered for a system, depending on the quantity that is maintained constant. In the above example, the displacement $\mathbf{d}$ of a positive ion determines the occurrence of an electric dipole (or of a macroscopic polarization $\mathbf{P}$). The quantity ε, which is thermodynamically conjugated to d_z, is therefore proportional to an electric field (the conjugation between quantities η and ζ is expressed by the fact that infinitesimal work on the system has the form $\zeta\,\mathrm{d}\eta$ – *cf.*

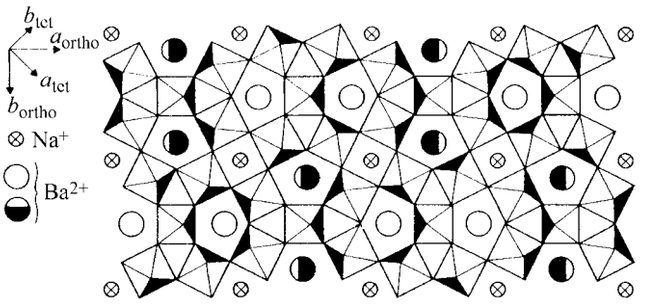

Fig. 3.1.5.12. Structure of the tungsten bronze barium sodium niobate $Ba_2NaNb_5O_{15}$ in its highest-temperature $P4/mbm$ phase above 853 K.

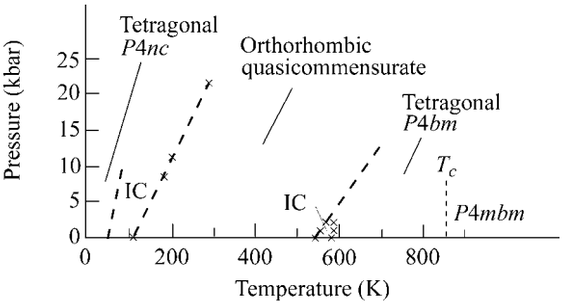

Fig. 3.1.5.13. Sequence of phases encountered with raising or lowering the temperature in barium sodium niobate.

with ribbons of such octahedra rather widely separated by the large ionic radius barium ions in the *b* direction. The resulting structure is, both magnetically and mechanically, rather two-dimensional, with easy cleavage perpendicular to the *b* axis and highly anisotropic electrical (ionic) conduction.

Most members of the BaMF$_4$ family (M = Mg, Zn, Mn, Co, Ni, Fe) have the same structure, which is that of orthorhombic C_{2v} (2*mm*) point-group symmetry. These materials are all ferroelectric (or at least pyroelectric; high conductivity of some makes switching difficult to demonstrate) at all temperatures, with an 'incipient' ferroelectric Curie temperature extrapolated from various physical parameters (dielectric constant, spontaneous polarization *etc.*) to lie 100 K or more above the melting point (*ca.* 1050 K). The Mn compound is unique in having a low-temperature phase transition. The reason is that Mn^{+2} represents (Shannon & Prewitt, 1969) an end point in ionic size (largest) for the divalent transition metal ions Mn, Zn, Mg, Fe, Ni, Co; hence, the Mn ion and the space for it in the lattice are not a good match. This size mismatch can be accommodated by the r.m.s. thermal motion above room temperature, but at lower temperatures a structural distortion must occur.

This phase transition was first detected (Spencer *et al.*, 1970) *via* ultrasonic attenuation as an anomaly near 255 K. This experimental technique is without question one of the most sensitive in discovering phase transitions, but unfortunately it gives no direct information about structure and often it signals something that is not in fact a true phase transition (in $BaMnF_4$ Spencer *et al.* emphasized that they could find no other evidence that a phase transition occurred).

Raman spectroscopy was clearer (Fig. 3.1.5.11*b*), showing unambiguously additional vibrational spectra that arise from a doubling of the primitive unit cell. This was afterwards confirmed directly by X-ray crystallography at the Clarendon Laboratory, Oxford, by Wondre (1977), who observed superlattice lines indicative of cell doubling in the *bc* plane.

The real structural distortion near 250 K in this material is even more complicated, however. Inelastic neutron scattering at Brookhaven by Shapiro *et al.* (1976) demonstrated convincingly that the 'soft' optical phonon lies not at $(0, 1/2, 1/2)$ in the Brillouin zone, as would have been expected for the *bc*-plane cell doubling suggested on the basis of Raman studies, but at $(0.39, 1/2, 1/2)$. This implies that the actual structural distortion from the high-temperature C_{2v}^{12} ($Cmc2_1$) symmetry does indeed double the primitive cell along the *bc* diagonal but in addition modulates the lattice along the *a* axis with a resulting repeat length that is incommensurate with the original (high-temperature) lattice constant *a*. The structural distortion microscopically approximates a rigid fluorine octahedra rotation, as might be expected. Hence, the chronological history of developments for this material is that X-ray crystallography gave the correct lattice structure at room temperature; ultrasonic attenuation revealed a possible phase transition near 250 K; Raman spectroscopy confirmed the transition and implied that it involved primitive cell doubling; X-ray crystallography confirmed directly the cell doubling; and finally neutron scattering revealed an unexpected incommensurate modulation as well. This interplay of experimental techniques provides a rather good model as exemplary for the field. For most materials, EPR would also play an important role in the likely scenarios; however, the short relaxation times for Mn ions made magnetic resonance of relatively little utility in this example.

3.1.5.2.8. *Barium sodium niobate*

The tungsten bronzes represented by $Ba_2NaNb_5O_{15}$ have complicated sequences of structural phase transitions. The structure is shown in Fig. 3.1.5.12 and, viewed along the polar axis, consists of triangular, square and pentagonal spaces that may or may not be filled with ions. In barium sodium niobate, the pentagonal channels are filled with Ba ions, the square channels are filled with sodium ions, and the triangular areas are empty.

The sequence of phases is shown in Fig. 3.1.5.13. At high temperatures (above $T_c = 853$ K) the crystal is tetragonal and paraelectric ($P4/mbm = D_{4h}^5$). When cooled below 853 K it becomes ferroelectric and of space group $P4bm = C_{4v}^2$ (still tetragonal). Between *ca.* 543 and 582 K it undergoes an incommensurate distortion. From 543 to *ca.* 560 K it is orthorhombic and has a '1q' modulation along a single orthorhombic axis. From 560 to 582 K it has a 'tweed' structure reminiscent of metallic lattices; it is still microscopically orthorhombic but has a short-range modulated order along a second orthorhombic direction and simultaneous short-range modulated order along an orthogonal axis, giving it an incompletely developed '2q' structure.

As the temperature is lowered still further, the lattice becomes orthorhombic but not incommensurate from 105–546 K; below 105 K it is incommensurate again, but with a microstructure quite different from that at 543–582 K. Finally, below *ca.* 40 K it becomes macroscopically tetragonal again, with probable space-group symmetry $P4nc$ (C_{4v}^6) and a primitive unit cell that is four times that of the high-temperature tetragonal phases above 582 K.

This sequence of phase transitions involves rather subtle distortions that are in most cases continuous or nearly continuous. Their elucidation has required a combination of experimental techniques, emphasizing optical birefringence (Schneck, 1982), Brillouin spectroscopy (Oliver, 1990; Schneck *et al.*, 1977; Tolédano *et al.*, 1986; Errandonea *et al.*, 1984), X-ray scattering, electron microscopy and Raman spectroscopy (Shawabkeh & Scott, 1991), among others. As with the other examples described in this chapter, it would have been difficult and perhaps impossible to establish the sequence of structures *via* X-ray techniques alone. In most cases, the distortions are very small and involve essentially only the oxygen ions.

3.1.5.2.9. *Tris-sarcosine calcium chloride (TSCC)*

Tris-sarcosine calcium chloride has the structure shown in Fig. 3.1.5.14. It consists of sarcosine molecules of formula

3.2. Twinning and domain structures

By V. Janovec, Th. Hahn and H. Klapper

3.2.1. Introduction and history

Twins have been known for as long as mankind has collected minerals, admired their beauty and displayed them in museums and mineral collections. In particular, large specimens of contact and penetration twins with their characteristic re-entrant angles and simulated higher symmetries have caught the attention of mineral collectors, miners and scientists. *Twinning* as a special feature of crystal morphology, therefore, is a 'child' of mineralogy, and the terms and symbols in use for twinned crystals have developed during several centuries together with the development of mineralogy.

The first scientific description of *twinning*, based on the observation of re-entrant angles, goes back to Romé de l'Isle (1783). Haüy (1801) introduced symmetry considerations into twinning. He described *hemitropes* (twofold rotation twins) and *penetration twins*, and stated that the *twin face* is parallel to a possible crystal face. Much pioneering work was done by Weiss (1809, 1814, 1817/1818) and Mohs (1822/1824, 1823), who extended the symmetry laws of twinning and analysed the symmetry relations of many twins occurring in minerals. Naumann (1830) was the first to distinguish between twins with parallel axes (*Zwillinge mit parallelen Achsensystemen*) and twins with inclined (*crossed*) axes (*Zwillinge mit gekreuzten Achsensystemen*), and developed the mathematical theory of twins (Naumann, 1856). A comprehensive survey of the development of the concept and understanding of twinning up to 1869 is presented by Klein (1869).

At the beginning of the 20th century, several important mineralogical schools developed new and far-reaching ideas on twinning. The French school of Mallard (1879) and Friedel (1904) applied the lattice concept of Bravais to twinning. This culminated in the lattice classification of twins by Friedel (1904, 1926) and his introduction of the terms *macles par mériédrie* (twinning by merohedry), *macles par pseudo-mériédrie* (twinning by pseudo-merohedry), *macles par mériédrie réticulaire* [twinning by reticular (lattice) merohedry] and *macles par pseudo-mériédrie réticulaire* (twinning by reticular pseudo-merohedry). This concept of twinning was very soon taken up and further developed by Niggli in Zürich, especially in his textbooks (1919, 1920, 1924, 1941). The lattice theory of Mallard and Friedel was subsequently extensively applied and further extended by J. D. H. Donnay (1940), and in many later papers by Donnay & Donnay, especially Donnay & Donnay (1974). The Viennese school of Tschermak (1904, 1906), Tschermak & Becke (1915), and Tertsch (1936) thoroughly analysed the morphology of twins, introduced the *Kantennormalengesetz* and established the minimal conditions for twinning. The structural and energy aspects of twins and their boundaries were first accentuated and developed by Buerger (1945). Presently, twinning plays an important (but negative) role in crystal structure determination. Several sophisticated computer programs have been developed that correct for the presence of twinning in a small single crystal.

A comprehensive review of twinning is given by Cahn (1954); an extensive treatment of mechanical twinning is presented in the monograph by Klassen-Neklyudova (1964). A tensor classification of twinning was recently presented by Wadhawan (1997, 2000). Brief modern surveys are contained in the textbooks by Bloss (1971), Giacovazzo (1992) and Indenbom (see Vainshtein *et al.*, 1995), the latter mainly devoted to theoretical aspects. In previous volumes of *International Tables*, two articles on twinning have appeared: formulae for the calculation of characteristic twin data, based on the work by Friedel (1926, pp. 245–252), are collected by Donnay & Donnay in Section 3 of Volume II of the previous series (Donnay & Donnay, 1972), and a more mathematical survey is presented by Koch in Chapter 1.3 of Volume C of the present series (Koch, 1999).

Independently from the development of the concept of twinning in mineralogy and crystallography, summarized above, the concept of *domain structures* was developed in physics at the beginning of the 20th century. This started with the study of *ferromagnetism* by Weiss (1907), who put forward the idea of a molecular field and formulated the hypothesis of differently magnetized regions, called *ferromagnetic domains*, that can be switched by an external magnetic field. Much later, von Hámos & Thiessen (1931) succeeded in visualizing magnetic domains by means of colloidal magnetic powder. For more details about magnetic domains see Section 1.6.4 of the present volume.

In 1921, Valasek (1921) observed unusual dielectric behaviour in Rochelle salt and pointed out its similarity with anomalous properties of ferromagnetic materials. This analogy led to a prediction of 'electric' domains, *i.e.* regions with different directions of spontaneous polarization that can be switched by an electric field. Materials with this property were called *Seignette electrics* (derived from the French, '*sel de Seignette*', denoting Rochelle salt). The term *seignettoelectrics* is still used in Russian, but in English has been replaced by the term *ferroelectrics* (Mueller, 1935). Although many experimental and theoretical results gave indirect evidence for *ferroelectric domain structure* [for an early history see Cady (1946)], it was not until 1944 that Zwicker & Scherrer (1944) reported the first direct optical observation of the domain structure in ferroelectric potassium dihydrogen phosphate (KDP). Four years later, Klassen-Neklyudova *et al.* (1948) observed the domain structure of Rochelle salt in a polarizing microscope (see Klassen-Neklyudova, 1964, p. 27). In the same year, Blattner *et al.* (1948), Kay (1948) and Matthias & von Hippel (1948) visualized domains and domain walls in barium titanate crystals using the same technique.

These early studies also gave direct evidence of the influence of mechanical stress and electric field on domain structure. Further, it was disclosed that a domain structure exists only below a certain temperature, called the *Curie point*, and that the crystal structures below and above the Curie point have different point-group symmetries. The Curie point thus marks a structural phase transition between a *paraelectric phase* without a domain structure and a *ferroelectric phase* with a ferroelectric domain structure. Later, the term 'Curie point' was replaced by the more suitable expression *Curie temperature* or *transition temperature*.

The fundamental achievement in understanding phase transitions in crystals is the *Landau theory* of continuous phase transitions (Landau, 1937). Besides a thermodynamic explanation of anomalies near phase transitions, it discloses that any continuous phase transition is accompanied by a discontinuous decrease of crystal symmetry. In consequence, a phase with lower symmetry can always form a domain structure.

The basic role of symmetry was demonstrated in the pioneering work of Zheludev & Shuvalov (1956), who derived by simple crystallographic considerations the point groups of paraelectric and ferroelectric phases of all possible ferroelectric phase transitions and gave a formula for the number of ferroelectric domain states.

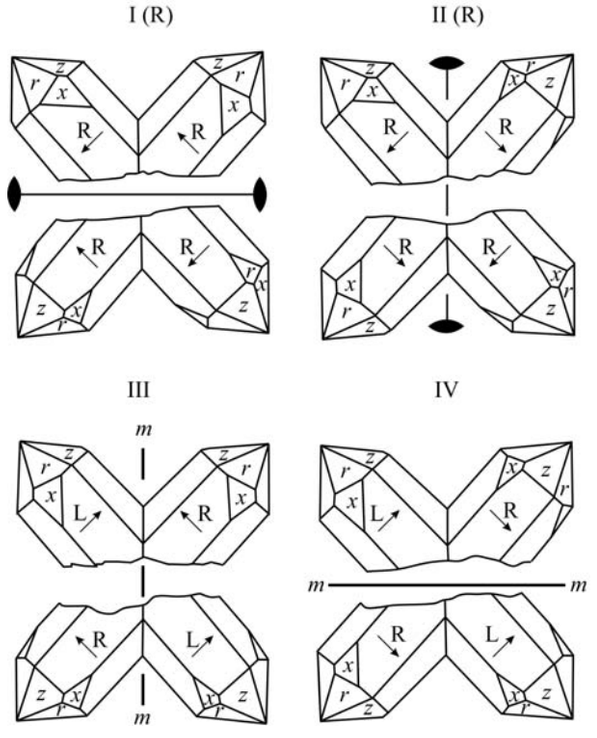

Fig. 3.3.6.3. The four variants of Japanese twins of quartz (after Frondel, 1962; *cf.* Heide, 1928). The twin elements 2 and *m* and their orientations are shown. In actual twins, only the upper part of each figure is realized. The lower part has been added for better understanding of the orientation relation. R, L: right-, left-handed quartz. The polarity of the twofold axis parallel to the plane of the drawing is indicated by an arrow. In addition to the cases I(R) and II(R) , I(L) and II(L) also exist, but are not included in the figure. Note that a vertical line in the plane of the figure is the zone axis $[11\bar{1}]$ for the two rhombohedral faces *r* and *z*, and is parallel to the twin and composition plane $(11\bar{2}2)$ and the twin axis in variant II.

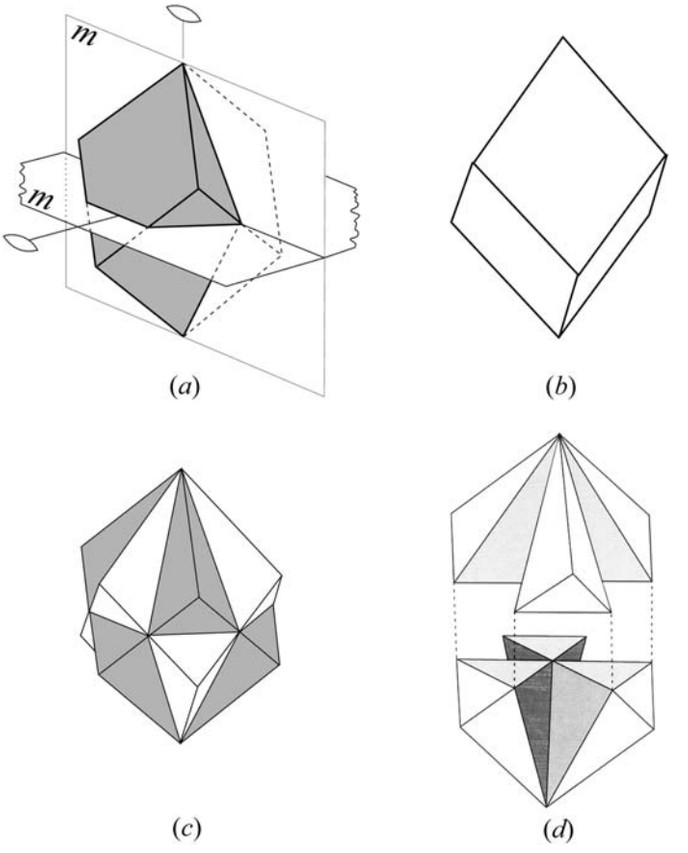

Fig. 3.3.6.4. Twin intergrowth of 'obverse' and 'reverse' rhombohedra of rhombohedral $FeBO_3$. (*a*) 'Obverse' rhombohedron with four of the 12 alternative twin elements. (*b*) 'Reverse' rhombohedron (twin orientation). (*c*) Interpenetration of both rhombohedra, as observed in penetration twins of $FeBO_3$. (*d*) Idealized skeleton of the six components (exploded along [001] for better recognition) of the 'obverse' orientation state shown in (*a*). The components are connected at the edges along the threefold and the twofold eigensymmetry axes. The shaded faces are $\{10\bar{1}0\}$ and (0001) coinciding twin reflection and contact planes with the twin components of the 'reverse' orientation state. Parts (*a*) to (*c*) courtesy of R. Diehl, Freiburg.

The *eigensymmetry* of high-temperature quartz is 622 (order 12). Hence, the coset of the Brazil twin law contains 12 twin operations, as follows:

(i) the six twin operations of a Brazil twin in low-temperature quartz, as listed above in Example 3.3.6.3.2;

(ii) three further reflections across planes $\{10\bar{1}0\}$, which bisect the three Brazil twin planes $\{11\bar{2}0\}$ of low-temperature quartz;

(iii) three further rotoinversions around [001]: $\bar{6}^1$, $\bar{6}^3 = m_z$, $\bar{6}^5 = \bar{6}^{-1}$.

The composite symmetry is

$$\mathcal{K} = \frac{6}{m'}\frac{2}{m'}\frac{2}{m'}(\bar{1}'),$$

a supergroup of index [2] of the *eigensymmetry* 622.

In high-temperature quartz, the combined Dauphiné–Brazil twins (Leydolt twins) are identical with Brazil twins, because the Dauphiné twin operation has become part of the *eigensymmetry* 622. Accordingly, both kinds of twins of low-temperature quartz merge into one upon heating above 846 K. We recommend that these twins are called 'Brazil twins', independent of their type of twinning in the low-temperature phase. Upon cooling below 846 K, transformation Dauphiné twin domains may appear in both Brazil growth domains, leading to four orientation states as shown in Fig. 3.3.6.2. Among these four orientation states, two Leydolt pairs occur. Such Leydolt domains, however, are not necessarily in contact (*cf.* Example 3.3.6.3.3 above).

In addition to these twins with 'parallel axes' (merohedral twins), several kinds of growth twins with 'inclined axes' occur in high-temperature quartz. They are not treated here, but additional information is provided by Frondel (1962).

3.3.6.5. *Twinning of rhombohedral crystals*

In some rhombohedral crystals such as corundum Al_2O_3 (Wallace & White, 1967), calcite $CaCO_3$ or $FeBO_3$ (calcite structure) (Kotrbova *et al.*, 1985; Klapper, 1987), growth twinning with a 'twofold twin rotation around the threefold symmetry axis [001]' (similar to the Dauphiné twins in low-temperature quartz described above) is common. Owing to the *eigensymmetry* $\bar{3}2/m$ (order 12), the following 12 twin operations form the coset (twin law). They are described here in hexagonal axes:

(i) three rotations around the threefold axis [001]: 6^1, $6^3 = 2_z$, $6^5 = 6^{-1}$;

(ii) three twofold rotations around the axes [120], [210], $[1\bar{1}0]$;

(iii) three reflections across the planes $(10\bar{1}0)$, $(1\bar{1}00)$, $(01\bar{1}0)$;

(iv) three rotoinversions around the threefold axis [001]: $\bar{6}^1$, $\bar{6}^3 = m_z$ and $\bar{6}^5 = \bar{6}^{-1}$.

Some of these twin elements are shown in Fig. 3.3.6.4. They include the particularly conspicuous twin reflection plane m_z perpendicular to the threefold axis [001]. The composite symmetry is

$$\mathcal{K} = \frac{6'}{m'}(\bar{3})\frac{2}{m}\frac{2'}{m'} \quad \text{(order 24)}.$$

It is of interest that for $FeBO_3$ crystals this twin law always, without exception, forms penetration twins (Fig. 3.3.6.4), whereas for the isotypic calcite $CaCO_3$ only (0001) contact twins are found (Fig. 3.3.6.5). This aspect is discussed further in Section 3.3.8.6.

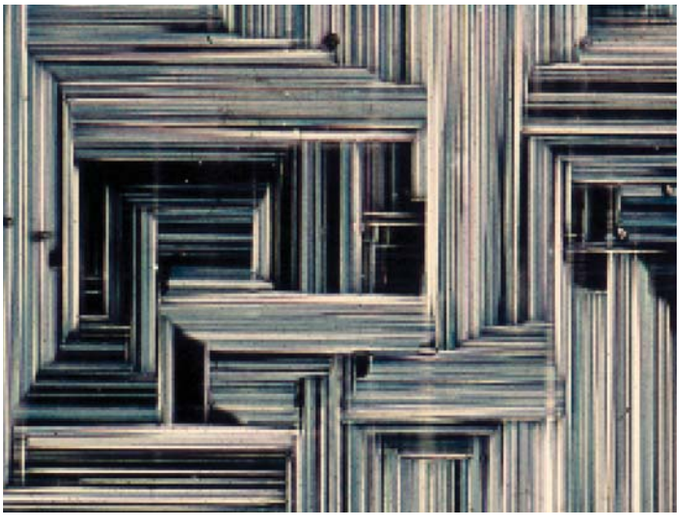

Fig. 3.3.10.13. Thin section of tetragonal leucite, $K(AlSi_2O_6)$, between crossed polarizers. The two nearly perpendicular systems of (101) twin lamellae result from the cubic-to-tetragonal phase transition at about 878 K. Width of twin lamellae 20–40 μm. Courtesy of M. Raith, Bonn.

(*cf.* Example 3.3.6.7). Three (cyclic) sets of orthorhombic twin lamellae with interfaces parallel to $\{10\bar{1}0\}_{hex}$ or $\{110\}_{orth}$ are generated by the transformation. More detailed observations on hexagonal–orthorhombic twins are available for the III⟶II (heating) and I⟶II (cooling) transformations of $KLiSO_4$ at about 712 and 938 K (Jennissen, 1990; Scherf *et al.*, 1997). The development of the three systems of twin lamellae of the orthorhombic phase II is shown by two polarization micrographs in Fig. 3.3.10.14. A further example, the cubic⟶rhombohedral phase transition of the perovskite $LaAlO_3$, was studied by Bueble *et al.* (1998).

Another surprising feature is the penetration of two or more differently oriented nano-sized twin lamellae, which is often encountered in electron micrographs (*cf.* Müller *et al.*, 1989, Fig. 2*b*). In several cases, the penetration region is interpreted as a metastable area of the higher-symmetrical para-elastic parent phase.

In addition to the fitting problems discussed above, the resulting final twin texture is determined by several further effects, such as:

(*a*) the nucleation of the (twinned) daughter phase in one or several places in the crystal;

(*b*) the propagation of the phase boundary (transformation front, *cf.* Fig. 3.3.10.14);

(*c*) the tendency of the twinned crystal to minimize the overall elastic strain energy induced by the fitting problems of different twin lamellae systems.

Systematic treatments of ferroelastic twin textures were first published by Boulesteix (1984, especially Section 3.3 and references cited therein) and by Shuvalov *et al.* (1985). This topic is extensively treated in Section 3.4.4 of the present volume. A detailed theoretical explanation and computational simulation of these twin textures, with numerous examples, was recently presented by Salje & Ishibashi (1996) and Salje *et al.* (1998). Textbook versions of these problems are available by Zheludev (1971) and Putnis (1992).

3.3.10.7.4. *Tweed microstructures*

The textures of ferroelastic twins and their fitting problems, discussed above, are 'time-independent' for both growth and deformation twins, *i.e.* after twin nucleation and growth or after the mechanical deformation there occurs in general no 'ripening process' with time before the final twin structure is produced.

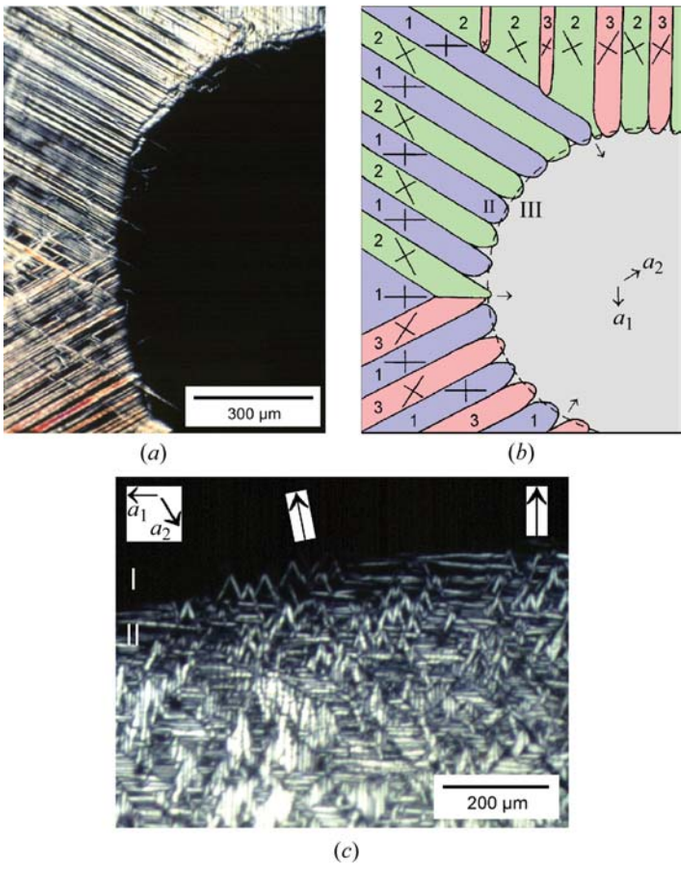

Fig. 3.3.10.14. Twin textures generated by the two different hexagonal-to-orthorhombic phase transitions of $KLiSO_4$. The figures show parts of $(0001)_{hex}$ plates (viewed along [001]) between crossed polarizers. (*a*) Phase boundary III⟶II with circular 712 K transition isotherm during heating. Transition from the inner (cooler) room-temperature phase III (hexagonal, dark) to the (warmer) high-temperature phase II (orthorhombic, birefringent). Owing to the loss of the threefold axis, lamellar $\{10\bar{1}0\}_{hex} = \{110\}_{orth}$ cyclic twin domains of three orientation states appear. (*b*) Sketch of the orientations states 1, 2, 3 and the optical extinction directions of the twin lamellae. Note the tendency of the lamellae to orient their interfaces normal to the circular phase boundary. Arrows indicate the direction of motion of the transition isotherm during heating. (*c*) Phase boundary I⟶II with 938 K transition isotherm during cooling. The dark upper region is still in the hexagonal phase I, the lower region has already transformed into the orthorhombic phase II (below 938 K). Note the much finer and more irregular domain structure compared with the III⟶II transition in (*a*). Courtesy of Ch. Scherf, PhD thesis, RWTH Aachen, 1999; *cf.* Scherf *et al.* (1997).

This is characteristically different for some transformation twins, both of the (slow) order–disorder and of the (fast) displacive type and for both metals and non-metals. Here, with time and/or with decreasing temperature, a characteristic microstructure is formed in between the high- and the low-temperature polymorph. This 'precursor texture' was first recognized and illustrated by Putnis in the investigation of cordierite transformation twinning and called '*tweed microstructure*' (Putnis *et al.*, 1987; Putnis, 1992). In addition to the hexagonal–orthorhombic cordierite transformation, tweed structures have been investigated in particular in the K-feldspar orthoclase (monoclinic–triclinic transformation), in both cases involving (slow) Si–Al ordering processes. Examples of tweed structures occurring in (fast) displacive transformations are provided by tetragonal–orthorhombic Co-doped $YBaCu_3O_{7-d}$ (Schmahl *et al.*, 1989) and rhombohedral–monoclinic $(Pb,Sr)_3(PO_4)_2$ and $(Pb,Ba)_3(PO_4)_2$ (Bismayer *et al.*, 1995).

Tweed microstructures are precursor twin textures, intermediate between those of the high- and the low-temperature modifications, with the following characteristic features:

3.4. Domain structures

By V. Janovec and J. Přívratská

3.4.1. Introduction

3.4.1.1. *Basic concepts*

It was demonstrated in Section 3.1.2 that a characteristic feature of structural phase transitions connected with a lowering of crystal symmetry is an anomalous behaviour near the transition, namely unusually large values of certain physical properties that vary strongly with temperature. In this chapter, we shall deal with another fundamental feature of structural phase transitions: the formation of a non-homogeneous, textured low-symmetry phase called a *domain structure*.

When a crystal homogeneous in the parent (prototypic) phase undergoes a phase transition into a ferroic phase with lower point-group symmetry, then this ferroic phase is almost always formed as a non-homogeneous structure consisting of homogeneous regions called *domains* and contact regions between domains called *domain walls*. All domains have the same or the enantiomorphous crystal structure of the ferroic phase, but this structure has in different domains a different orientation, and sometimes also a different position in space. When a domain structure is observed by a measuring instrument, different domains can exhibit different tensor properties, different diffraction patterns and can differ in other physical properties. The domain structure can be visualized optically (see Fig. 3.4.1.1) or by other experimental techniques. Powerful high-resolution electron microscopy (HREM) techniques have made it possible to visualize atomic arrangements in domain structures (see Fig. 3.4.1.2). The appearance of a domain structure, detected by any reliable technique, provides the simplest unambiguous experimental proof of a structural phase transition.

Under the influence of external fields (mechanical stress, electric or magnetic fields, or combinations thereof), the domain structure can change; usually some domains grow while others decrease in size or eventually vanish. This process is called *domain switching*. After removing or decreasing the field a domain structure might not change considerably, *i.e.* the form of a domain pattern depends upon the field history: the domain structure exhibits *hysteresis* (see Fig. 3.4.1.3). In large enough fields, switching results in a reduction of the number of domains. Such a procedure is called *detwinning*. In rare cases, the crystal may consist of one domain only. Then we speak of a *single-domain crystal*.

There are two basic types of domain structures:

(i) Domain structures with one or several systems of parallel plane domain walls that can be observed in an optical or electron microscope. Two systems of perpendicular domain walls are often visible (see Fig. 3.4.1.4). In polarized light domains exhibit different colours (see Fig. 3.4.1.1) and in diffraction experiments splitting of reflections can be observed (see Fig. 3.4.3.9). Domains can be switched by external mechanical stress. These features are typical for a *ferroelastic domain structure* in which neighbouring domains differ in mechanical strain (deformation). Ferroelastic domain structures can appear only in ferroelastic phases, *i.e.* as a result of a phase transition characterized by a spontaneous shear distortion of the crystal.

(ii) Domain structures that are not visible using a polarized-light microscope and in whose diffraction patterns no splitting of reflections is observed. Special methods [*e.g.* etching, deposition of liquid crystals (see Fig. 3.4.1.5), electron or atomic force microscopy, or higher-rank optical effects (see Fig. 3.4.3.3)] are needed to visualize domains. Domains have the same strain and cannot usually be switched by an external mechanical stress. Such domain structures are called *non-ferroelastic domain structures*. They appear in all non-ferroelastic phases resulting from symmetry lowering that preserves the crystal family, and in partially ferroelastic phases.

Another important kind of domain structure is a *ferroelectric domain structure*, in which domains differ in the direction of the spontaneous polarization. Such a domain structure is formed at ferroelectric phase transitions that are characterized by the appearance of a new polar direction in the ferroic phase. Ferro-

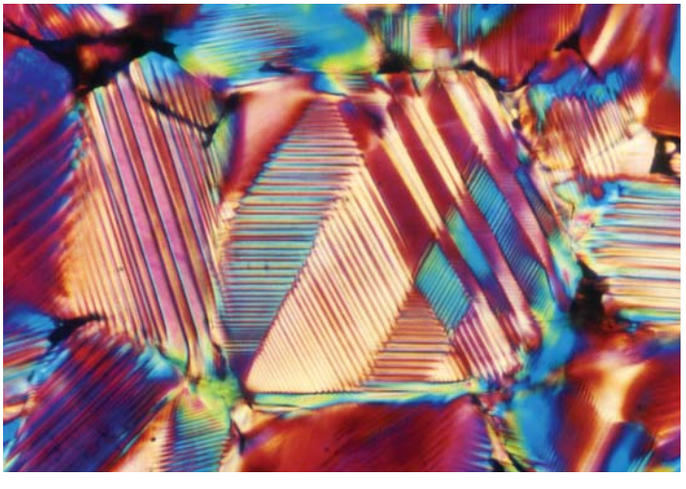

Fig. 3.4.1.1. Domain structure of tetragonal barium titanate ($BaTiO_3$). A thin section of barium titanate ceramic observed at room temperature in a polarized-light microscope (transmitted light, crossed polarizers). Courtesy of U. Täffner, Max-Planck-Institut für Metallforschung, Stuttgart. Different colours correspond to different ferroelastic domain states, connected areas of the same colour are ferroelastic domains and sharp boundaries between these areas are domain walls. Areas of continuously changing colour correspond to gradually changing thickness of wedge-shaped domains. An average distance between parallel ferroelastic domain walls is of the order of 1–10 μm.

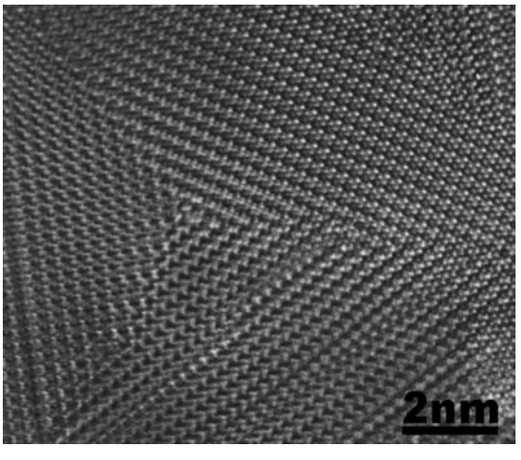

Fig. 3.4.1.2. Domain structure of a $BaGa_2O_4$ crystal seen by high-resolution transmission electron microscopy. Parallel rows are atomic layers. Different directions correspond to different ferroelastic domain states of domains, connected areas with parallel layers are different ferroelastic domains and boundaries between these areas are ferroelastic domain walls. Courtesy of H. Lemmens, EMAT, University of Antwerp.

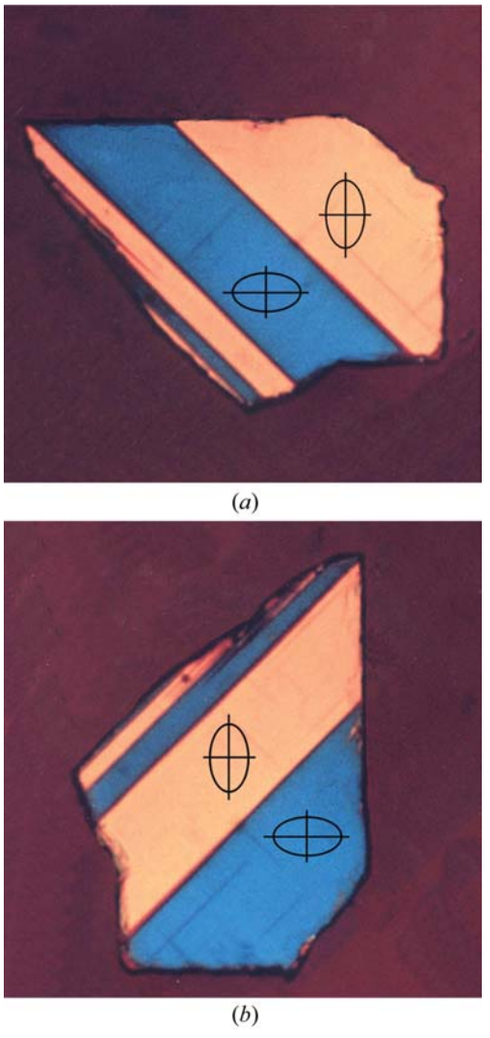

Fig. 3.4.3.7. Ferroelastic twins in a very thin $YBa_2Cu_3O_{7-\delta}$ crystal observed in a polarized-light microscope. Courtesy of H. Schmid, Université de Geneve.

$YBa_2Cu_3O_{7-\delta}$ in Fig. 3.4.3.7. The symmetry descent $G = 4_z/m_z m_x m_{xy} \supset m_x m_y m_z = F_1 = F_2$ gives rise to two ferroelastic domain states $\mathbf{R}_1$ and $\mathbf{R}_2$. The twinning group K_{12} of the non-trivial domain pair $(\mathbf{R}_1, \mathbf{R}_2)$ is

$$K_{12}[m_x m_y m_z] = J_{12}^{\star} = m_x m_y m_z \cup 4_z^{\star}\{2_x m_y m_z\} = 4_z^{\star}/m_z m_x m_{xy}^{\star}. \tag{3.4.3.61}$$

The colour of a domain state observed in a polarized-light microscope depends on the orientation of the index ellipsoid (indicatrix) with respect to a fixed polarizer and analyser. This index ellipsoid transforms in the same way as the tensor of spontaneous strain, *i.e.* it has different orientations in ferroelastic domain states. Therefore, different ferroelastic domain states exhibit different colours: in Fig. 3.4.3.7, the blue and pink areas (with different orientations of the ellipse representing the spontaneous strain in the plane of of figure) correspond to two different ferroelastic domain states. A rotation of the crystal that does not change the orientation of ellipses (*e.g.* a 180° rotation about an axis parallel to the fourfold rotation axis) does not change the colours (ferroelastic domain states). If one neglects disorientations of ferroelastic domain states (see Section 3.4.3.6) – which are too small to be detected by polarized-light microscopy – then none of the operations of the group $F_1 = F_2 = m_x m_y m_z$ change the single-domain ferroelastic domain states $\mathbf{R}_1$, $\mathbf{R}_2$, hence there is no change in the colours of domain regions of the crystal. On the other hand, all operations with a star symbol (operations lost at the transition) exchange domain states $\mathbf{R}_1$ and $\mathbf{R}_2$, *i.e.* also exchange the two colours in the domain regions. The corresponding permutation is a transposition of two colours and this attribute is represented by a star attached to the symbol of the operation. This exchange of colours is nicely demonstrated in Fig. 3.4.3.7 where a −90° rotation is accompanied by an exchange of the pink and blue colours in the domain regions (Schmid, 1991, 1993).

It can be shown (Shuvalov *et al.*, 1985; Dudnik & Shuvalov, 1989) that for small spontaneous strains the amount of shear s and the angle φ can be calculated from the second invariant Λ_2 of the differential tensor Δu_{ik}:

$$s = 2\sqrt{-\Lambda_2}, \tag{3.4.3.62}$$

$$\varphi = \sqrt{-\Lambda_2}, \tag{3.4.3.63}$$

where

$$\Lambda_2 = \begin{vmatrix} \Delta u_{11} & \Delta u_{12} \\ \Delta u_{21} & \Delta u_{22} \end{vmatrix} + \begin{vmatrix} \Delta u_{22} & \Delta u_{23} \\ \Delta u_{32} & \Delta u_{33} \end{vmatrix} + \begin{vmatrix} \Delta u_{11} & \Delta u_{13} \\ \Delta u_{31} & \Delta u_{33} \end{vmatrix}. \tag{3.4.3.64}$$

In our example, where there are only two nonzero components of the differential spontaneous strain tensor [see equation (3.4.3.58)], the second invariant $\Lambda_2 = -(\Delta u_{11}\Delta u_{22}) = -(u_{22} - u_{11})^2$ and the angle φ is

$$\varphi = \pm|u_{22} - u_{11}|. \tag{3.4.3.65}$$

In this case, the angle φ can also be expressed as $\varphi = \pi/2 - 2\arctan a/b$, where a and b are lattice parameters of the orthorhombic phase (Schmid *et al.*, 1988).

The shear angle φ ranges in ferroelastic crystals from minutes to degrees (see *e.g.* Schmid *et al.*, 1988; Dudnik & Shuvalov, 1989).

Each equally deformed plane gives rise to two compatible domain walls of the same orientation but with opposite sequence of domain states on each side of the plane. We shall use for a *simple domain twin* with a planar wall a symbol $(\mathbf{R}_1^+|\mathbf{n}|\mathbf{R}_2^-)$ in which $\mathbf{n}$ denotes the normal to the wall. The bra–ket symbol (| and |) represents the half-space domain regions on the negative and positive sides of $\mathbf{n}$, respectively, for which we have used letters $\mathcal{B}_1$ and $\mathcal{B}_2$, respectively. Then $(\mathbf{R}_1^+|$ and $|\mathbf{R}_2^-)$ represent domains $\mathbf{D}_1(\mathbf{R}_1^+, \mathcal{B}_1)$ and $\mathbf{D}_2(\mathbf{R}_2^-, \mathcal{B}_2)$, respectively. The symbol $(\mathbf{R}_1^+|\mathbf{R}_2^-)$ properly specifies a domain twin with a zero-thickness domain wall.

A domain wall can be considered as a domain twin with domain regions restricted to non-homogeneous parts near the plane p. For a domain wall in domain twin $(\mathbf{R}_1^+|\mathbf{R}_2^-)$ we shall use the symbol $[\mathbf{R}_1^+|\mathbf{R}_2^-]$, which expresses the fact that a domain wall of zero thickness needs the same specification as the domain twin.

If we exchange domain states in the twin $(\mathbf{R}_1^+|\mathbf{n}|\mathbf{R}_2^-)$, we get a *reversed twin (wall)* with the symbol $(\mathbf{R}_2^-|\mathbf{n}|\mathbf{R}_1^+)$. These two ferroelastic twins are depicted in the lower right and upper left parts of Fig. 3.4.3.8, where – for ferroelastic–non-ferroelectric twins – we neglect spontaneous polarization of ferroelastic domain states. The reversed twin $\mathbf{R}_2^-|\mathbf{n}'|\mathbf{R}_1^+$ has the opposite shear direction.

Twin and reversed twin can be, but may not be, crystallographically equivalent. Thus *e.g.* ferroelastic–non-ferroelectric twins $(\mathbf{R}_1^+|\mathbf{n}|\mathbf{R}_2^-)$ and $(\mathbf{R}_2^-|\mathbf{n}|\mathbf{R}_1^+)$ in Fig. 3.4.3.8 are equivalent, *e.g. via* 2_z, whereas ferroelastic–ferroelectric twins $(\mathbf{S}_1^+|\mathbf{n}|\mathbf{S}_3^-)$ and $(\mathbf{S}_3^-|\mathbf{n}|\mathbf{S}_1^+)$ are not equivalent, since there is no operation in the group K_{12} that would transform $(\mathbf{S}_1^+|\mathbf{n}|\mathbf{S}_3^-)$ into $(\mathbf{S}_3^-|\mathbf{n}|\mathbf{S}_1^+)$.

As we shall show in the next section, the symmetry group $\mathsf{T}_{12}(\mathbf{n})$ of a twin and the symmetry group $\mathsf{T}_{21}(\mathbf{n})$ of a reverse twin are equal,

$$\mathsf{T}_{12}(\mathbf{n}) = \mathsf{T}_{21}(\mathbf{n}). \tag{3.4.3.66}$$